DEVELOPMENT OF A MICROFLUIDIC OXYGENATOR AS AN OXYGENATING UNIT OF A LUNG ASSIST DEVICE FOR TERM AND PRE-TERM NEONATES WITH RESPIRATORY DISTRESS SYNDROME

Development of a Microfluidic Oxygenator as the Oxygenating Unit of a Lung Assist Device for Term and Pre-Term Neonates with Respiratory Distress Syndrome

By

Harpreet Matharoo

A Thesis

Submitted to the School of Graduate Studies

in Partial Fulfillment of the Requirement

for the Degree

Master of Applied Science

McMaster University

Hamilton, Ontario, Canada

MASTER OF APPLIED SCIENCE (2015) McMaster University
MECHANICAL ENGINEERING Hamilton, Ontario Canada

TITLE	Development of a Microfluidic Oxygenator as an Oxygenating Unit of a Lung Assist Device for Term and Pre-Term Neonates with Respiratory Distress Syndrome
AUTHOR	Harpreet Matharoo, B.Tech
SUPERVISOR	Dr. P. R. Selvaganapathy, Canada Research Chair of Biomicrofluidics, Associate Professor Department of Mechanical Engineering
NUMBER OF PAGES	xvii, 171

Abstract

Respiratory distress syndrome is a major cause of mortality among infants. Current therapies are limited in terms of invasiveness, cost, infrastructure, and leads to long term morbidities such as bronchopulmonary dysplasia. As a result a form of respiratory support termed as “artificial placenta” has been developed that allows natural development of lungs and avoids long term morbidities. The artificial placenta is connected via the umbilical vessels and provide pumpless respiratory support and is characterized by non-invasiveness, low cost and low infrastructure. Our group previously reported on a development of porous PDMS membrane artificial placenta. To build upon its development, one of the objectives of this thesis was to reduce the variation in the oxygen saturation of the input blood for testing the oxygenator. Another objective was to setup a mathematical model to predict the oxygen uptake in an oxygenating unit and use the model to optimize the geometric parameters of a design. The final objective was to improve the oxygen uptake of the oxygenating unit of the artificial placenta by redesigning the blood flow path and the membrane material.

The experimental setup was improved to employ an active controller that actively maintained the oxygen saturation of the input blood for testing the oxygenator within a variation of ±3% of the set point for at least an hour. As compared to previous experimental setup the blood deviated from the set point by 9%.

Later, the blood flow path in the oxygenator was redesigned from a flat height profile to a sloping height profile; and the PDMS membrane was reinforced with a thin steel mesh. Such changes improved the oxygen uptake at the operating pressure of 30 mmHg from 16

μL/min in case of an oxygenator with flat height profile and PDMS membrane to 26 μL/min in case of an oxygenator with flat profile and composite membrane.

Finally, a mathematical model was developed that coupled oxygen uptake, pressure drop and membrane expansion. The model was validated against experimental results and was later used to optimize the configuration of the oxygenator with sloping profile and composite membrane. The predicted oxygen uptake of the optimized configuration at the operating pressure of 30 mmHg was 78.8 μL/min.

Acknowledgements

I would first like to thank my supervisor Dr. Ravi for giving me the opportunity to work on this unique project. Dr. Ravi has been immense help throughout my masters. His guidance and advice has been useful and extends beyond academics, to life in general. Secondly, I give my gratitude to Dr. Christoph Fusch for his valuable advice. Also, I would like to thank Niels Rochow and Dr. Gerhard Fusch for the initial training and guiding me through the health sciences aspect of the project.

My master would have been devoid of any meaning if it was not for my lab mates. I was fortunate to have the support of two different groups of students, who made it enjoyable to work around them. A special thanks to my family for always encouraging me to be the best version of myself. Lastly, I want to thank my friends for celebrating my achievements and just making Canada an overall fun experience.

Table of Contents

List of Figures

List of Tables

Glossary

Arteriovenous	Relating to artery and vein. For example arteriovenous pressure drop means pressure drop between an artery and a vein.
Cardiopulmonary Bypass	A part of the blood returning to the heart is diverted to a machine before it is returned to arterial circulation.
Extracorporeal	Occurring outside of the body. For example cardiopulmonary bypass employs extracorporeal circulation.
Hemorrhage	Excessive bleeding characterized by patient's inability to stop the flow.
Hypercarbia	Abnormally elevated carbon dioxide in blood
Intracranial Hemorrhage	Build of blood in the skull leading to increase in intracranial pressure.
Oxygen Saturation	Percentage of hemoglobin in blood bound to oxygen

Chapter 1 – Motivation & Organization

Respiratory distress syndrome (RDS) is recognized by any signs of difficulty in breathing in an infant. The severity of the disease vary from low to lethal. In the US alone, around 40,000 infants get affected by RDS every year. Over the past 60 years, neonatal care has taken huge technological strides in reducing mortality related to RDS in neonates. Neonatal mortality rate related to RDS has also significantly reduced in high-resource countries from 2.89 per 1000 live births between 1969 and 1973 to 0.4 per 1000 live births in 1995 [2]. However, in developing countries, RDS occurrence and its related mortality remain very high. For example in India, RDS occur at a greater frequency with 200,000 infants getting affected every year. RDS related mortality ranged from 57% to 89% in 1990s [3], [4]. Regardless, availability of technologically advanced equipment in developing countries has shown improvement in neonatal mortality rates [5].

Current modalities of respiratory support for RDS include surfactant replacement therapy (SRT), assisted ventilation, and extracorporeal membrane oxygenation (ECMO). During SRT, exogenous surfactants are administered to an infant's lungs to assist in breathing. SRT has shown improvement on neonatal mortality rate [6]. SRT improves the ability of the lungs to accept oxygen; however additional respiratory support is required to fully compensate for the lack of lung maturity, which can be done through various means. One of such means is assisted ventilation, the goal of which is to provide adequate oxygenation to the lungs and ventilate them. The disadvantage of assisted ventilation is that it leads to long term morbidities such as bronchopulmonary dysplasia (BPD). BPD is characterized by arrested lung development causing long term pulmonary complications

which lead to re-hospitalization of the patient in the subsequent years. BPD affects almost all infants with RDS treated with assisted ventilation [7].

To eliminate BPD, extracorporeal membrane oxygenation (ECMO) techniques were developed. In ECMO support, the blood is withdrawn from the infant and is oxygenated externally in a device. Once oxygenated, the blood is returned to the body. ECMO has shown to significantly improve mortality rate over assisted ventilation [8]. However, the main disadvantage of this method is that it requires surgery to connect the device to the circulatory system. There is a potential for blood loss that could lead to complications such as hemorrhage, intracranial hemorrhage, and neurological complications [9].

To eliminate potential blood loss, a non-invasive technique that mimics placental environment to provide respiratory support has been under development. The technique is similar to ECMO, but the blood is withdrawn from the umbilical vessels. The technique has been used on various animals with up to 3 weeks of support [10]. In the experiments, commercial hollow fiber oxygenator and spiral coil oxygenators have been used. However, such devices have high priming volume and cannot be used for neonatal respiratory support.

In an attempt to reduce the priming volume, artificial placentas that use microfluidic oxygenating units have been developed [11]. Such units have low priming volume, high surface area to provide adequate oxygen, and can be designed to have low pressure drop. The work presented in this thesis contributes to the development of such an artificial placenta that uses microfluidic oxygenating unit.

1.1 Objectives

The main goal of the thesis are to contribute to the development of an artificial placenta that uses microfluidic oxygenators as the oxygenating unit. The work is specifically focused on developing such oxygenating units. The objectives of the work are as follows:

1) Build an experimental set up that keeps the oxygen saturation of the blood constant with time so that it could be used to measure the performance of an oxygenator to uptake oxygen.
2) Improve the performance of the oxygenating unit by increasing its oxygen saturation capability at improving its ability to handle high flow rates under the operating pressure provided by the neonate's vascular pressure.

The following are the unique contributions of this thesis to the specific body of knowledge in this field:

1) Blood is to be used to measure the oxygen uptake performance of devices; however precisely controlling oxygen saturation of blood proved to be difficult. A closed loop system was built that controls the oxygen saturation of the blood. The blood from the loop can be withdrawn and used to test an oxygenator device.
2) The oxygenator is a two-part device consisting of blood channels and a gas permeable membrane. The performance of the oxygenator depends on the geometry of the blood channels and the material of the membrane. In the work, the performance of the oxygenator was improved by 44%.
3) A thorough understanding of the mechanism of oxygen uptake is necessary for the development of the device. A mathematical model was developed to be able to

predict the performance of a conceived design prior to experimental testing. This contribution will help the future students in fine tuning the design to meet performance requirements.

1.2 Thesis Organization

In total, there are 8 chapters in this thesis.

Chapter 2 delves into the functioning of lungs and the cause of respiratory distress syndrome. Subsequently, various modalities of treatment in a clinical setting are discussed. Finally, development of microfluidic oxygenators in research is reviewed.

Chapter 3 presents literature review on various types of membrane oxygenators and mathematical modeling used to predict the performance of a microfluidic oxygenator.

Chapter 4 details the design constraints and various designs of oxygenator tested in our study. Subsequently, the fabrication process to manufacture these designs is described. Later, experimental methods to measure burst pressure, membrane expansion, hydraulic resistance of the oxygenator with water, and performance of the oxygenator with the blood is presented. Finally, redesign of the experimental setup to measure oxygen uptake of a device is presented. In the new experimental setup, the oxygen saturation of the input blood remains within a range of $\pm 5\%$ of the set value. This feature allows reliable measurement of the performance of an oxygenator device by passing the input blood through the device and measuring the increase in oxygen saturation.

Chapter 5 presents the mathematical model developed to predict the performance of an oxygenator. It is a multiphysics model that takes in geometrical parameter of the device

and measure the oxygen uptake and pressure drop as a function of flow rate. Subsequently, the model is validated against the results of the oxygenators in research.

Chapter 6 presents experimental results of in-vitro testing of the designs detailed in chapter 4. The results are also compared against the mathematical predictions using the model explained in chapter 5.

Chapter 7 presents parametric analysis of the designs explained in the chapter 4. Only geometric parameters are analyzed. The analysis will be useful for the future researchers in fine tuning the performance of the device.

Chapter 8 concludes the thesis and sets up the stage for future work.

Chapter 2 – Introduction

Lungs are organs responsible for exchanging gases between the blood and the atmosphere through breathing. Spontaneous breathing happens through a two staged process: inspiration and expiration. During inspiration, the pressure inside the lungs is lower than the atmosphere pressure due to the forces generated by the respiratory muscles and vice-versa during expiration as shown in figure 2.1 [11].

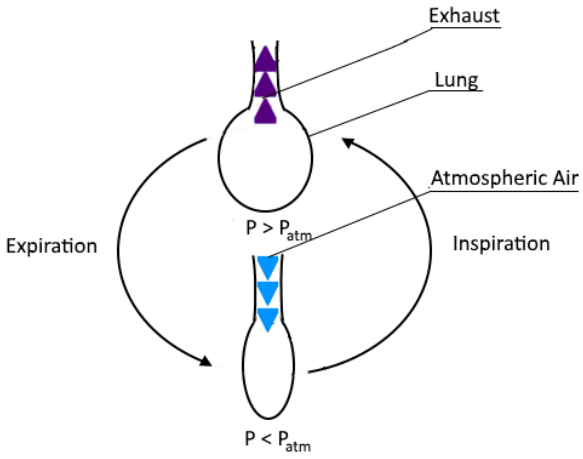

Figure 2.1 Schematic representation of the process of spontaneous breathing

Lungs have two functional areas: conducting system and gas exchange system [12]. The conducting system is responsible for delivering and withdrawing gases to and from the gas exchange system. The gas exchange system is responsible for exchanging gases between the blood stream and the atmosphere. As shown in figure 2.2, the conducting system consists of nasal passages, pharynx, larynx, trachea, bronchi, and bronchioles until terminal bronchioles. These bronchioles are supported by cartilage to prevent it from collapsing on expiration. Gas exchange system contains respiratory bronchioles, alveolar sacs, alveolar ducts, and alveoli. The gas exchange system is a non-cartilage system that interfaces with

a gas permeable membrane that consists of connective tissues, epithelial cells, endothelial cells, pericytes etc. Also, the surface of alveoli that is exposed to atmosphere is covered with plasma and surfactant. The alveolar surfactant changes the surface tension of the plasma to stabilize the lungs. Without the surfactants, the lungs would collapse upon expiration [13]. Avery and Mead [13] showed the surface tension of plasma depends on the surface area of the lung, which changes upon expiration and inspiration. The surface tension was found to vary from 5 dynes/cm^2 to 60 dynes/cm^2.

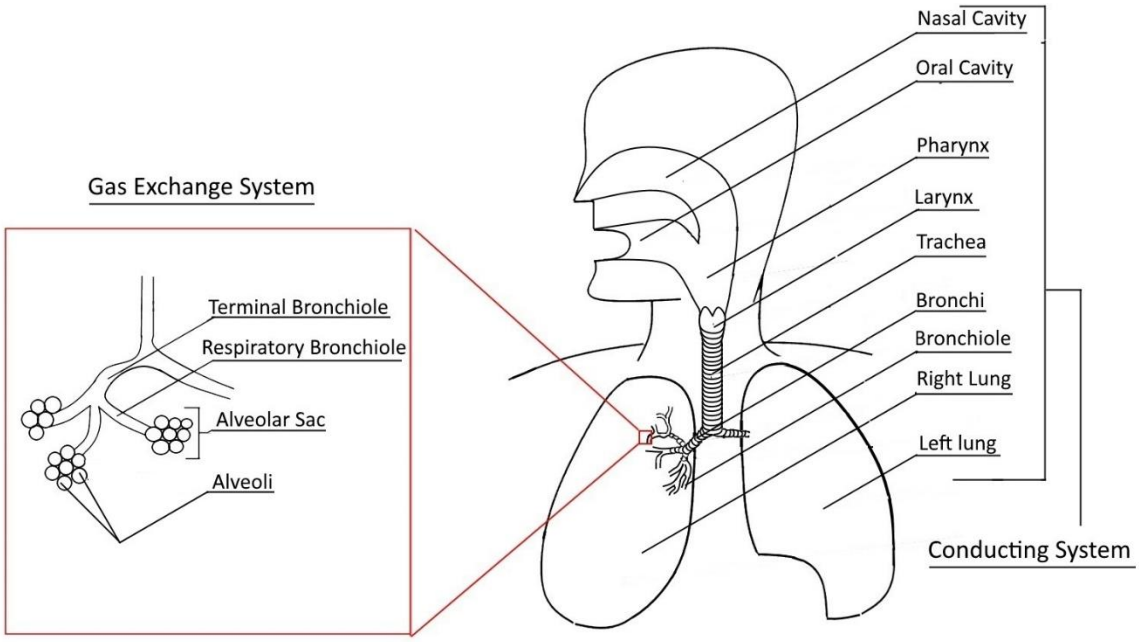

Figure 2.2 Illustration of the conducting zone and the gas exchange zone of a lung. Terminal bronchiole shown in the gas exchange system, belongs to the conducting zone and is used as a reference in the diagram.

Lungs are one of the last organs to develop in fetal development. Therefore, preterm infants often suffer from pulmonary complications. There are about 4.1 million infants born every year in the US, out of which 12% are affected by preterm birth [14]. The lungs of a prematurely born infant may lack lung maturity causing difficulty in breathing. The

complication is also called Respiratory distress syndrome (RDS). It is caused by lack of surfactants in lungs. Lack of surfactant causes difficulty in expansion and contraction during breathing, which in turn causes poor gas exchange between the air and the blood. This causes complications such as hypoxia, hypercarbia, respiratory acidosis, and metabolic acidosis [7]. Around 10% of babies born prematurely in the US are affected by RDS [14]. The risk increases with prematurity. For babies born before 29 weeks, the risk of developing RDS is 60% [14]. Birth weight also affects the risk of developing RDS. It has been reported to affect 56% of infants weighing between 501 g and 1500 g in the US [7].

Management of infants with RDS is complex and is done through various modalities such as surfactant replacement therapy, mechanical ventilation, continuous positive airway pressure, and extracorporeal membrane oxygenation. Introduction of antenatal steroid has also proven beneficial in accelerating lung maturation.

2.2 Assisted Ventilation

Surfactant replacement therapy improves oxygen uptake by the lung; however lack of structural maturity of lungs still causes oxygen deficiency and requires additional respiratory support. Assisted ventilation is used in addition with SRT to compensate for the oxygen deficiency. Goal of assisted ventilation is to provide adequate oxygenation to the blood and ventilation to the lung by manipulating the air pressure and the air flow rate inside the lungs. The air flow rate can be administered by various means such as through endotracheal intubation, nasal prongs, or by creating an artificial airway in the trachea by making an incision [11].

The first mechanical ventilator was developed in 20th century. The ventilator applied intermittent positive airway pressure (IPPV) using time cycled, pressure limited devices [15]. The ventilator is relatively easy to use, leaving all the parameters such as frequency at the discretion of the operator. However, frequency set by the operator may not synchronize with infants breathing pattern causing asynchronous breathing causing discomfort for the infant and risk of lung damage [16].

IPPV remained major mode of ventilation for three decades, before concerns of asynchronous breathing led to the development of more advanced modes of ventilation [16]. Newer modes of ventilation introduced non-invasive methods to deliver airflow such as through nasal prongs [17]. Such methods have been used along with IPPV and continuous positive airway pressure [17] & [18]. Concerns of asynchronous breathing were also addressed by introducing synchronous intermittent positive pressure ventilation [16].

Ventilatory management has taken huge strides since its inception to provide adequate oxygenation and decrease lung injury. Nevertheless, ventilatory management still induced associated pulmonary complications [19]. Riyas *et al* [20] showed 51% of 102 babies on mechanical ventilation survived. 58.8% of 102 babies developed complications. Such pulmonary complications include barotrauma, bronchopulmonary dysplasia, and chronic lung disease. Furthermore, ventilation is likely to fail in the cases of pulmonary hypertension of the newborn and congenital diaphragmatic hernia. These limitations of assisted ventilation calls for an alternative treatment, which is discussed in the next section.

2.1 Surfactant Replacement Therapy (SRT)

In 1950s, Avery and Mead reported the role of surfactant deficiency in pathophysiology of RDS [13]. Soon after that, surfactant replacement therapy (SRT) was conceived. It is the administration of exogenous surfactants to a neonate's lungs through endotracheal tube.

SRT has been shown to significantly decrease mortality among infants born at less than 30 weeks gestation with birth weight less than 1250 g [21]. Fujiwara *et al* successfully treated 10 mechanically ventilated infants with diagnoses of RDS with modified bovine surfactant extract [6]. Soll [22] identified six randomized controlled trials of SRT to neonates with established RDS, and found synthetic surfactants to significantly improve pulmonary gas exchange and decrease requirement for ventilator support in premature infants.

However, the incidences of other medical morbidities remain unchanged. Such morbidities include bronchopulmonary dysplasia [23]. Also, it has been hypothesized that administration of synthetic surfactants to infants born at 27 weeks' gestation may have increased incidences of pulmonary hemorrhage [23].

2.3 Extracorporeal Membrane Oxygenation

In extracorporeal membrane oxygenation (ECMO), the blood is taken out of the body and passed through the respiratory support device, which compensates for the underperformance of the lungs by exchanging the gases between the blood and the atmosphere. Figure 2.3 demonstrates a simplified version of the circuit used to provide respiratory support through ECMO in a clinical setting. A bypass is made by making an incision where the blood is withdrawn from using a pump. The pump pushes the blood through an ECMO device that exchanges gases between the blood and the atmosphere. The

oxygenated blood is subsequently returned back to the body. ECMO works as an alternative to assisted ventilation and must be administered with SRT. SRT is essential for natural development of the lung.

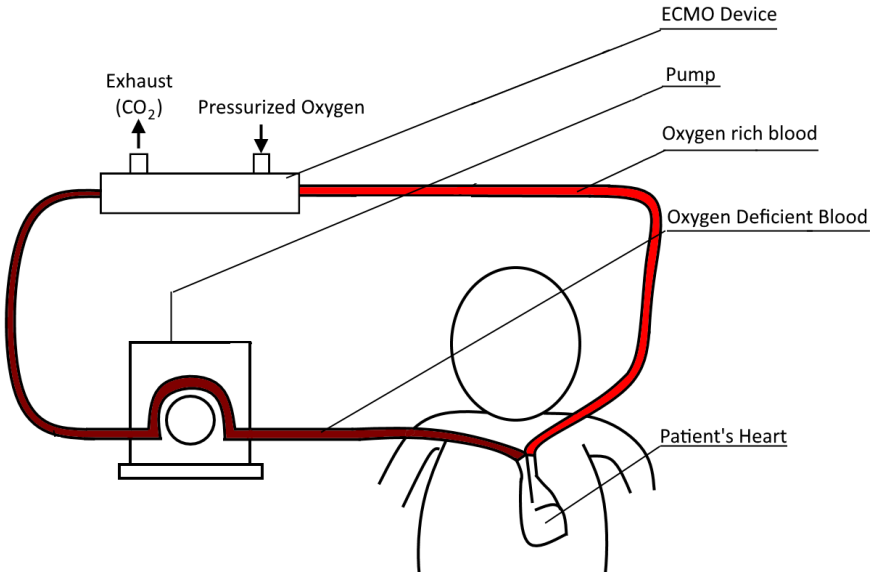

Figure 2.3 Schematic representation of the use of ECMO in a clinical setting.

In 1976, Barlett *et al* [24] demonstrated efficacy of ECMO by saving 4 out of 13 critically-ill infants. O'Rourke *et al* [25] recruited 39 neonates with 85% likelihood of dying and randomly assigned them with assisted ventilation or ECMO as the respiratory support. The mortality rate for ventilation and ECMO were 40% and 3% respectively. Kanto *et al* [26] reported 83% survival rate for neonates with RDS and 80% likelihood of dying, when treated with ECMO. Mugford *et al* [8] analyzed four trials comparing ECMO with assisted ventilation and reported that use of ECMO had a significant effect on mortality. They found that ECMO provided a risk ratio of 0.44 indicating that if ECMO rather than ventilation is used for every three babies with respiratory failure, one additional infant will survive.

Despite lower mortality for ECMO as compared to assisted ventilation, it still causes some morbidities. Neonates treated with ECMO are at a higher risk of intracranial hemorrhage. Brain development is affected, and may be accompanied by neurological complications [9]. Potential blood loss due to the invasiveness of the technique and its high dead volume make it impossible to use to treat preterm neonates with this technique [11]. Downard [27] reported 4.9% of 23,556 ECMO patients from Extracorporeal Life Support Organization Registry, suffered from intracranial hemorrhage, out of which over 2000 patients had significant cannula site and surgical site bleeding. Also, surgical site bleeding was prominent after cardiac procedures, with more than 30% incidence of significant hemorrhage.

2.4 Artificial Placenta

Artificial placenta uses ECMO devices to oxygenate the blood, but the devices are administered through umbilical cords instead. This feature avoids the complexities related to cardiopulmonary bypass techniques and some morbidities such as hemorrhage. One of the earliest reported cases of artificial placenta is by Zapol *et al* [10], who provided two days of total extra-uterine support to an isolated premature lamb fetus using a spiral coil ECMO device with 70 ml priming volume and 0.4 m^2 gas exchange area. The rate of blood flow in the device was 70 – 100 ml/min/kg using a pump. The device was found to be capable of providing sufficient oxygenation when the input venous oxygen saturation varied between 55 % and 75 %. However, there was no information reported on the oxygen uptake and the output oxygenation level achieved. In a later reported case, the survival time was extended to 3 weeks.

The first pump-less circuit where the flow through the device was powered by the arterio-venous pressure difference was reported by Awad *et al* [28]. The animal was kept alive for up to 6 hours using a microporous hollow-fiber membrane oxygenator with 90 ml priming volume. The partial pressure of oxygen in blood increased by estimated average of 490 mmHg from the inlet to the outlet of the oxygenator. Information on increase in oxygen saturation was not reported.

Reoma *et al* [29] used neonatal lamb model and provided support for the fetuses for up to 4 hours. High cannula resistance and declining device flow hampered prolonged support. The device flow rate reduced from 382±90 to 176±24 ml/min over 4 hours. As a result, the oxygen uptake reduced from 13.55±4.91 ml/min/kg to 5.01±0.87 ml/min/kg. The baseline oxygen saturation was set at 61.23% $\pm$ 16.76%. The oxygen saturation at the outlet ranged from 92.5% to 99.7%. Also, in the study, the fetuses were submerged into artificial amniotic fluid to simulate placental environment.

Gray *et al* [30] provided support for neonatal lamb for 24 hours through extracorporeal life support as artificial placenta. In this study, polypropylene hollow fiber oxygenator with surface area of 0.5 m^2 were used. Information on the oxygen uptake was not reported. The mean circuit flow for five survivors was 94±20 ml/kg/min.

Miura *et al* [31] supported premature lamb on a pumpless arteriovenous extracorporeal life support for 18±3.2 hours. The oxygenator used was able to deliver oxygen transfer in the range of 10.5 – 12.2 mL/min for circuit blood flow rate in the range of 25 – 125 mL/min/kg. However, the circuit volume was 60 mL, which is high for clinical application for neonates. Hence, additional development is needed.

Manan [11] conceptualized an artificial placenta with focus on microfabricated oxygenating units. In this study, microfluidic devices made out of Polydimethylsiloxane (PDMS) with PDMS, polycarbonate (PC), and porous PDMS membranes were tested. Each unit had a gas exchange area of 13.6 cm^2 and a dead volume of 0.11 ml. Later, the units made with PDMS membrane were stacked in a parallel flow configuration and tested on a piglet. The device demonstrated an average O_2 transfer of 3.5 $\mu L/min/cm^2$ at a flow of 14 ml/min. Current study builds up on the works of Manan [11] in developing a microfluidic oxygenator.

Bryner *et al* [32] treated extremely premature lambs with an artificial placenta using an ECMO device and compared the results with the control of similar lambs treated with high-frequency oscillatory ventilation. The artificial placenta model involves a pump-driven veno-venous system with a targeted circuit flow of 75-100 mL/min/kg and a pO_2 of 35-50 mmHg. The lambs treated with ventilation survived for 2-8 hours, while the ones treated with artificial placenta survived for 1 week with hemodynamic stability and adequate gas exchange. The artificial placenta proved promising however, the priming volume for the whole circuit was 200 ml, which twice the blood volume of a neonate. Hence, additional development is needed.

Schoberer *et al* [33] treated premature lamb with an extracorporeal membrane oxygenator for 6 hours. The oxygenator device increased partial pressure of oxygen in the blood from 20±16.6 mmHg to 446.2±104.6 mmHg at device flow rates of 109.3±11.8 mL/h (1.82±0.1967 mL/min). Also, the total circuit volume was 21 ml out of which 14 ml was contributed by the oxygenator device. As the device operating flow rates are significantly lower than the desired flow rate (30 mL/min), it requires additional development.

The artificial placenta type membrane oxygenators are suitable for neonatal respiratory support. Such device would reduce complications, long term morbidities, and mortality. However for the devices so far been used had high priming volume for neonates. Manan's [11] device is the one with low priming volume, but the oxygen uptake capacity is low. So the challenge is to improve the oxygen uptake while maintaining the low dead volume, which is the focus of this thesis.

Chapter 3 – Literature Review

This chapter provides a broad overview of the historical development of oxygenator technology which began in the early 20th century. Earliest oxygenator applied direct contact between the blood and the atmosphere to oxygenate the blood which tended to contaminate the blood and led to alternate approaches. Later, the designs were modified to separate the blood and the atmosphere by means of a gas permeable membrane. Since then many membrane oxygenator designs have been developed. Such designs include spiral membrane oxygenator in which blood flows in a thin film in a spiral form, hollow fiber oxygenator in which the blood either flows into or over hollow fibers, and microfluidic oxygenator in which dimension of the blood channel is less than 100 μm. All these designs have been explained in greater detail in the rest of the chapter.

3.1 Historical Development

Initial prototypes of oxygenator applied direct contact between the blood and the gases. The gas exchange was achieved by either forming a thin film of blood exposed to atmosphere or introducing gas bubbles in the blood. The former design is called film oxygenator, while the latter is called bubble oxygenator [11]. Both these designs exchanged adequate amount of gases. In 1956, DeWall *et al* [34] introduced a bubble oxygenator capable of fully oxygenating venous blood up to 3 L/min. Later on, a modified version of the oxygenator was used on 50 adult patients in the same study. The oxygenator was able to maintain the mean oxygen saturation of the arterial blood at 96.2%. However, prolonged exposure of the blood to the gases caused significant damage to the blood through trauma

or/and air embolism [35]. This led to the development of membrane oxygenators, in which a permeable interface was introduced between the blood and the gases.

3.2 Membrane Oxygenator

Membrane oxygenator is the state-of-the-art technology for respiratory care. The oxygenator types differ from each other in terms of fluid path as well as the gas flow. Some of the key types of such oxygenators have been discussed in detail in the following sub sections.

3.2.1 Spiral Oxygenator

Spiral oxygenators were some of the first oxygenator that were developed as far back as in 1956 [36]. The design is shown in figure 3.1. Kolobow and Bowman [37] introduced a spiral membrane oxygenator with a dip-coated silicone membrane in 1963. Several different configurations of the device were tested. The oxygenators had surface area of 1.2 m^2 with priming volume from 80 ml and 110 ml, with maximum O_2 uptake of 120 ml/min/m^2 and 82 ml/min/m^2 respectively. In a later study, a number of spiral oxygenators were used to give respiratory support to unanesthetized lambs for up to 16 days. The oxygenators had a surface area ranging from 0.88 to 1.62 m^2. The flow rate ranged from 400-700 ml/min. Later, Barlett *et al* [38] reported treating 45 newborns with 23 survivors. Also, the device proved reliable in a study of 50 infants, however prolonged usage led to a decrease in platelet count and fibrinogen by 50% and 31% respectively [39]. This effect is likely observed as a result of high shear rates in the device.

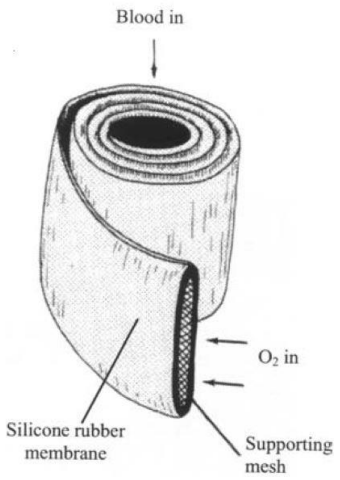

Figure 3.1 Illustration of a spiral membrane oxygenator as shown in [2]*. The blood flows parallel to the core and the gas flows inside the membrane envelope.*

3.2.2 Hollow Fiber Oxygenator

First introduced in 1972, development of hollow fiber oxygenator marks a big step in the history of oxygenators. Hollow fiber is the structural unit of the oxygenator to separate blood from the atmosphere. In the beginning, the fibers were micro porous to allow gas exchange [36]. In a later developmental stride, the fibers were coated with silicone to avoid leakage.

There are two designs of hollow fiber oxygenator available: shell/tube and cross flow [40]. These designs are illustrated in figure 3.2. In a shell/tube type oxygenator, the blood flows inside the hollow fiber while the gas flows outside of it. In a cross flow oxygenator, the blood flows outside of the hollow fiber and the gases flow inside of it. For similar gas exchange rates, cross flow oxygenator has lower hydraulic resistance and requires 2-2.5 times less amount of surface area of gas exchange [40].

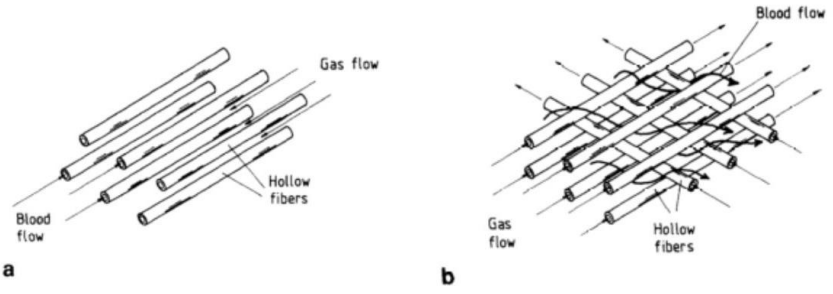

Figure 3.2 Diagram contrasting structural difference in (a) shell/tube type oxygenator and (b) cross flow oxygenator as shown in [40].

Table 3.1 lists the range of performance and the geometric parameters of commercially available oxygenators at different points in time. The range for gas exchange area has changed from 1.8 – 5.4 m^2 in 1988 to 0.5 – 2.5 m^2 in 2016. This can be attributed to the improved oxygen uptake in the devices, which required less amount of gas exchange area to oxygenate similar blood flow rates. Also, the range for priming volume has also reduced from 320 – 730 ml in 1988 to 43 – 260 ml in 2016. This can be attributed to need for lower gas exchange area and the development of advanced manufacturing techniques which allowed fabrication of fibers with high surface to volume ratio. The pressure drop has also reduced. Limited data on oxygen flux also shows significant improvement in gas exchange from 1988 to 1994.

Review	Area (m^2)	Priming Volume (ml)	Oxygen Flux (ml/min/m^2)	Max Flow Rate (ml/min)	Pressure (mmHg)
Gaylor 1988 [40]	1.8 – 5.4	320 – 730	55.5 – 181.5	6.5 – 7	50.9 – 266
Gaylor 1994 [41]	1.7 – 3.7	220 – 560	119 – 221	-	60 – 260
Voorhees 1997 [42]	1.7 – 2.5 m^2	299 – 479	-	-	70 – 148
Current 2016	0.5 – 2.5 m^2	43 – 260	-	4 – 7	-

Table 3.1 List of range of the performance and the geometric parameters of hollow fiber oxygenators at different points in time.

Hollow fiber oxygenator is the state-of-the-art oxygenator technology. However, the problem of plasma leakage through micropores still exists [36]. Also, it requires large volumes and mechanical pumps, which implies that it can only be used for infants greater than 24 weeks and weight more than 2000 grams, thereby excluding preterm population [43].

3.2.3 Microfluidic Oxygenator

Advent of electronic computers spurred development of advanced manufacturing technology that allowed fabrication of parts at a micro-scale. The adaptation of this technology to fluid mechanics led to the development of microfluidics that deals with small fluid volumes – of the order of μL to pL – flowing in channels with small characteristic dimension (1-1000 um) [44]. One of the applications of microfluidics is in cell culture, which required development of custom oxygenators to maintain dissolved oxygen concentration in culture media [45].

These oxygenators have been adapted in research to provide respiratory support. Lee *et al* [46] developed theoretical models of microfluidic artificial lungs with eight different geometries and assessed their suitability for oxygenation. Four types of designs, as shown in Figure 3.3 were assessed in the study: circular channels embedded in a flat sheet, rectangular channels with gas permeable walls, broad open rectangular channels with support posts, and screen filled channels. Flow rate of 4 L/min, pressure drop of 10 mmHg, and the blood saturation of 66% at the inlet and 98% at the outlet were imposed as the boundary conditions.

Figure 3.3 (a) shows the design of circular channels embedded in a gas permeable membrane. The blood flows into the circular channels and the gas permeates from the sides. Figure 3.3 (b) shows the design of rectangular channels with gas permeable membrane. The blood flows into a series of parallel rectangular channels and one of the walls is gas permeable where gas exchange happens. Figure 3.3 (c) shows the design of wide rectangular channels with support posts. In this design, the channels are wider than the previous case, hence support posts are introduced to stabilize the membrane. Figure 3.3 (d) shows the design of screen filled rectangular channel. The presence of screen introduces transverse mixing, improving overall gas exchange area. The study found circular channels of diameter 12 µm to be the most attractive at a priming volume of 13 ml and the oxygen flux of 6.6 µl/min/cm^2.

Table 3.2 lists the geometric and the performance parameters of the other designs conceived by Lee *et al* [46]. The table also compares various types of microfluidic oxygenator designs in their ability to oxygenate the testing fluid at different flow rates. The table lists geometrical parameters, membrane material, testing fluid, and performance parameters.

In the second paper of the series by Lee *et al* [46], Kung *et al* [47] manufactured a scaled down version of the oxygenator with screen-filled wide rectangular channels. The device integrated a stainless steel screen of 40 µm and 80 µm thickness into blood channels of the same height. A combination of devices with a capillary length of 3 mm or 6 mm were tested. For devices with 40 µm channel height, the gas exchange surface area was 1.27 cm^2. For the devices with 80 µm channel height, the surface area ranged from 1.16 to 2.38 cm^2. The estimated oxygen uptake was in the range of 14.79 – 22.15 µL/min/cm^2 for 40 µm

high devices and 9.85 – 18.46 µL/min/cm^2 for 80 µm high devices. The maximum pressure drop reported for 40 µm high devices was 5.8 mmHg; pressure drop for 80 µm high devices was not reported. Also, the estimated blood flow rates was in the range of 0.8 – 2.4 ml/min for 40 µm high devices and 0.5 – 2 ml/min for 80 µm high devices. The devices used pressurized 100% oxygen.

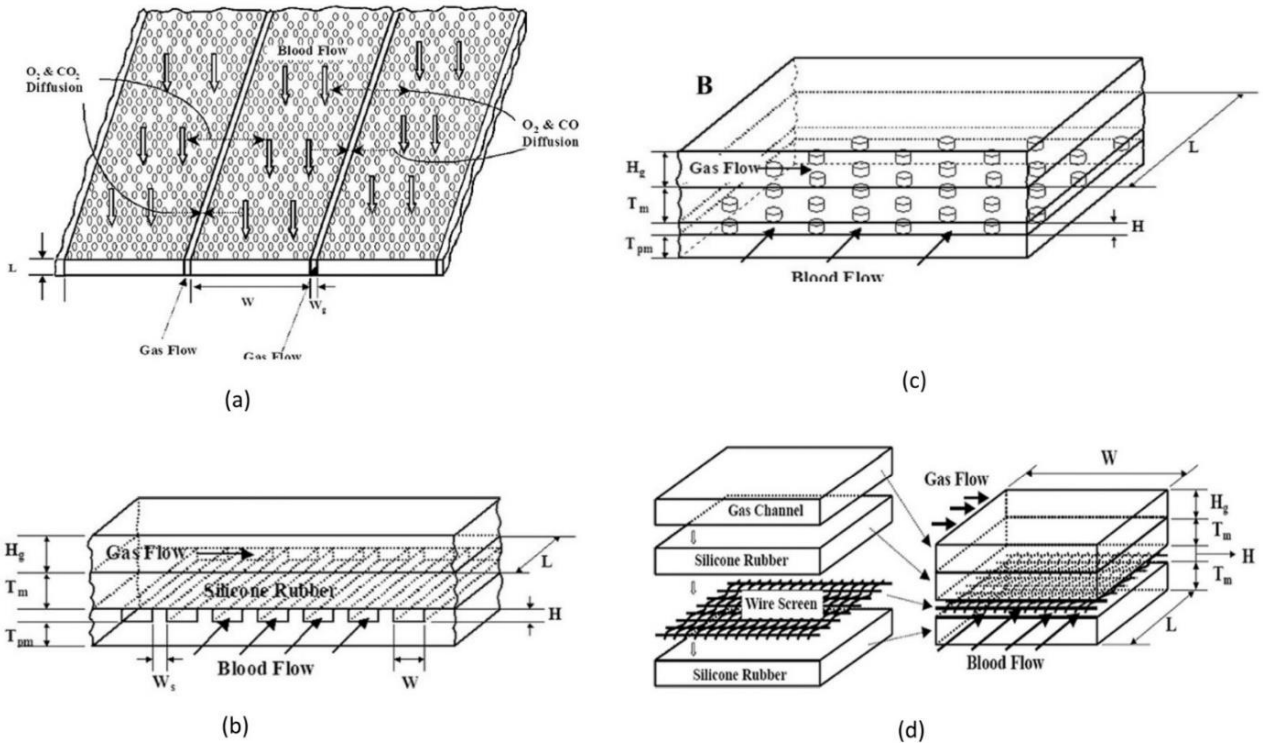

Figure 3.3 Illustration of various types of designs by Lee et al [46] *(a) Circular channels embedded in a gas permeable membrane, (b) Rectangular channel with gas permeable membrane, (c) Wide rectangular channels with support posts, (d) Screen filled rectangular channels*

In the second paper of the series by Lee *et al* [46], devices with rectangular channels were manufactured and tested [48]. In particular, two designs containing rectangular channels were tested. One of the designs exhibited wide rectangular channels with support posts as shown in figure 3.3(b) while the other had straight parallel rectangular channels (figure 3.3(c)). The gas exchange area for the devices were 0.83 cm^2 ml at 0.00124 ml of dead

volume and 1.16 cm^2 at 0.00174 ml of dead volume for straight rectangular channels (SC) and wide rectangular channels with support posts (SP) respectively. Also, the design with support post more efficiently uses the area as it exhibited higher ratio of surface area to nominal area (0.84). The dead volumes reported here are for the blood volume exposed to oxygenation. The dead volume for inlet and outlet were not incorporated. The blood flow rates varied within 1.6 – 1.9 ml/min and 0.5 – 2.0 ml/min for SC and SP respectively at pressure drop lying in between 2 – 4 mmHg. Also, the maximum oxygen uptake for SC and SP was 26.2 and 24.7 µL/min/cm^2 respectively. The maximum oxygen uptake by the devices presented in this series will translate to a maximum increase in oxygen saturation by 10% at a flow rate of 2 ml/min. The devices use pressurized oxygen as the ventilating gas, hence they cannot be used as a lung assist device

Table 3.2 List of parameters of oxygenator designs. Geometrical parameters, membrane material, testing fluid, and performance parameters are listed. The estimated values are marked with an asterisk(*).

Group	Lee 2008 [46] (theory)
Height (µm)	12 25
Channel Type	Circular
Surface Area (cm^2)	42241* 84087*
Surface Area/ Nominal Area	-
Dead Volume (ml)	13 50
Membrane Material	PDMS
Testing Fluid	Human Blood
Gas	O_2
Pressure drop (mmHg)	
Flow Rate (ml/min)	4000
Oxygen (µl/min/cm^2)	6.6* 3.32*

					Kung [47]		Lee 2008 [48]	
12	25	12	25	40	40	80	15	15
Rectangular		Rectangular with Support Posts		Screen-Filled Rectangular	Screen-Filled Rectangular		Rectangular With Support Posts	Rectangular
10875*	20100*	10844.5*	20067*	8362*	1.27	1.16 – 2.38	1.16	0.83
-		-		-	<0.5*		0.84	0.5
13	50	13	50	27	0.004	0.008 – 0.015	0.00174	0.00124
PDMS		PDMS		PDMS	PDMS		PDMS	PDMS
Human Blood		Human Blood		Human Blood	Bovine Blood		Bovine Blood	Bovine Blood
O_2		O_2		O_2	O_2		O_2	O_2
10		10		10	5.8(max)	N/A	2 – 4	
4000		4000		4000	0.8 – 2.4*	0.5 – 2*	0.5 – 2*	1.6 – 1.9*
25.64*	13.87*	25.7*	13.89*	33.3*	14.8 – 22.1*	9.85 – 18.5*	16 – 24.7*	26.3*

Potkay 2009 [49]	Hoganson 2010 [50]	Kniazeva 2010 [51]	Potkay 2011 [52]	Wu 2013 [53]	Kovach 2015 [54]
30	Variable	100	10 20	80	200-10
Rectangular	Rectangular Variable Height	Rectangular	Rectangular	Rectangular with Support Posts	Rectangular Variable Height
2.4	23.1	-	1.67 2.34	13.6*	15.1*
0.5	0.3	-	0.5* 0.5*	0.76	0.45*
0.011	-	0.173*	0.002 0.006	0.109*	0.196*
PDMS	PDMS	PDMS	PDMS	µp-PDMS PDMS PC	PDMS
DI Water	Sheep Blood	PBS	Pig Blood	Human (Expired Blood)	Bovine Blood
O_2	O_2	O_2	Air	Air	O_2
7-19	7-19	N/A	150-300 50-500	7-32 15-36 17-55 16 - >60	2-10
-	.5-6.3	.12-.33*	.5-1.4 .25-1.5	0.5-4	0.2-1
-	.3-3.4	.3-.53*	11.8-20.8 6.3-12.6	1-1.9 .8-1.1 .5-1.1 .9-1.3	0.78-1.33*

In 2009, Potkay [49] introduced a micro-machined artificial lung with dimensions comparable to natural lung. The device featured 30 µm high channels. The device was

tested by oxygenating deionized water. However, the experimental study was limited that the setup only measured the diffusional resistance of the membrane. The membrane resistance to oxygen diffusion was found to be 27 X 10^3 $ml^{-1}s.cm^2.cmHg$.

In 2010, Hoganson *et al* [50] developed a micro-machined artificial lung featuring a microvascular network of blood channels with variable depth. Figure 3.4 illustrates the geometry of the device. The depth of the channels varies in the streamline direction. This design feature was introduced to mimic similar flow distribution as in lungs. The design also featured alveolar chambers on the other side of the membrane to introduce high pressure gas. This was done to enhance gas exchange. The operating flow rate varied from 0.5 – 6.3 ml/min at which pressure of 7-19 mmHg were reached. Resulting oxygen uptake was 3.4 $\mu L/min/cm^2$.

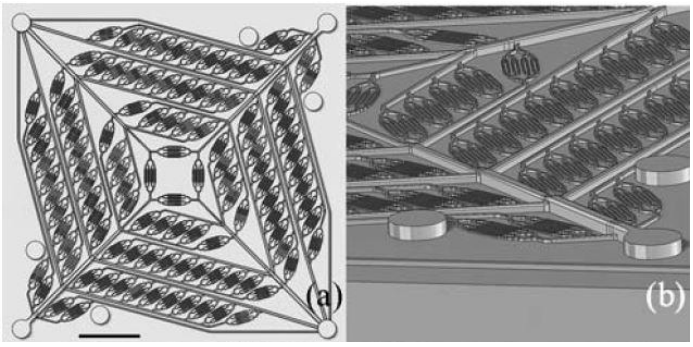

Figure 3.4 Illustration of oxygenator device by Hoganson et al [50] *(a) Shows the top view of the fluid path and (b) Computer aided drawing of the mold. Notice the variable depth of the channels in the computer drawing.*

The device has low pressure drop, and high operating flow rate, but low oxygen flux as compared to Lee's [48] device. However, the device uses pressurized 100% oxygen as input, which makes the device resource intensive and bulky. Also, the design inefficiently uses the nominal area, as it uses just 30% of the nominal area. Hence, the device is not suitable to be used for a lung assist device

In 2011, Potkay *et al* [52] addressed issues of portability by doing a theoretical analysis of branched network with varying channel heights. Later, devices with optimal performance were fabricated for experimental study. The result showed high oxygen flow rate in the range of 6.3 – 20.8 µL/min/cm^2. The device has high gas exchange area and uses atmospheric air to oxygenate the blood. However, the device has extremely high pressure drops (>100 mmHg) at such dimensions and operating flow rates, which makes it unsuitable for use in a lung assist device.

Later, Kniazeva *et al* [51] introduced a parallel plate multilayered oxygenator. Each layer featured a branched microvascular network sitting on top a thin gas permeable membrane with alveolar chambers for gas on the other side to enhance gas exchange. The device was tested using phosphate buffered saline. The resulting oxygen uptake was in the range of 0.3 – 0.53 µL/min/cm^2 at flow rates of 0.12 – 0.33 ml/min. Since the devices were not tested using blood, the study lacks enough evidence to prove the applicability of the device in a lung assist device for neonates.

In 2013, Wu *et al* [53] reported a microvascular network with square pillars. The defining feature of the device was that it was exposed to atmospheric air instead of pressurized gas. Various types of membranes were tested in the study. The oxygenator achieved a maximum gas exchange rate of 1.46 µL/min/cm^2 and 5.27 µL/min/cm^2 for O_2 and CO_2 respectively at 4 ml/min of blood flow rate for porous PDMS membrane. The devices demonstrate low pressure drop (32 - 60 mmHg) at the operating flow rate. Also, the devices use atmospheric ambient air to oxygenate the blood. Hence, such devices may be suitable to be used in a lung assist device.

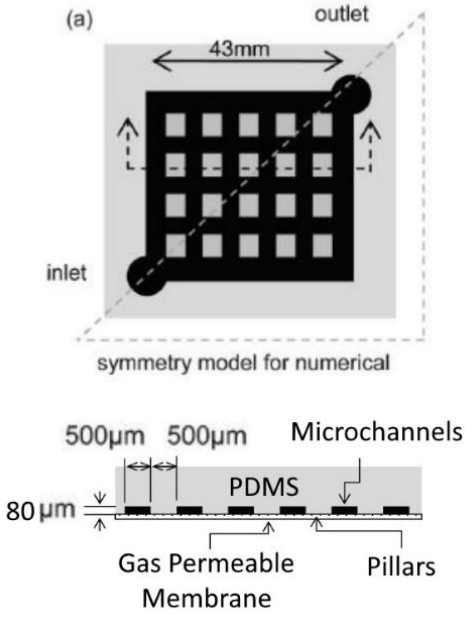

Figure 3.5 Illustration of the oxygenator design by Wu et al [53].

The device with porous membrane has an oxygen transfer of 1.46 µL/min/cm^2 at the flow rate of 4 ml/min, which translates to an estimated increase in oxygen saturation by 2.5%. This does not meet the requirement as a lung assist device for preterm neonates as the device needs to produce an increase in oxygen saturation by 30% at the operating flow rate. Hence, additional development is needed on the device.

In 2015, Kovach *et al* [54] introduced an oxygenator with biomimetic flow. Biomimetic flow promotes uniform wall shear rate and minimizes blood trauma. The oxygenator used pressurized oxygen to oxygenate the blood. The oxygenator achieved oxygen uptake of 0.78-1.33 µL/min/cm^2 at blood flow rates of 0.2 - 1 ml/min. The pressure drops at such flow rates was in the range of 2 – 10 mmHg. The device is unsuitable to be used as a lung assist device as it uses pressurized 100% oxygen to oxygenate the blood.

3.3 Mathematical Modeling

It is essential to understand the effect of various geometric features on the performance of the device. Hence, a mathematical model was developed to simulate the oxygenator. This section provides the historical development of mathematical modeling of an oxygenator.

One of the earliest attempt to model the oxygen uptake by blood in a membrane oxygenator was that by Weisman *et al* [55]. In the study, blood flowing in a round tube was modeled. First, oxygen uptake by blood flowing in a straight round tube was studied. Later, various modifications were made to the tube to introduce mixing to enhance the oxygen uptake. In particular, effect of a manifold that divides into smaller streams and recombines the flow downstream was modeled and studied. Later, effect of turbulent mixing was also modeled. Finally, the axis of the tube was bent into a helical coil and its effect on the oxygen uptake was studied. In all cases, sedimentation was assumed to have no effect on the velocity profile. For oxygen uptake, the blood was assumed homogenous with red blood cells uniformly distributed. Red cells were also assumed to uptake the oxygen instantaneously. The oxygen uptake was numerically solved using mass balance equation for oxygen. The information on the type of solver and mesh was not available. The solver solves for the distribution of oxygen saturation at any cross-section of the tubing. Experiments were performed to measure the oxygen saturation of the blood at the outlet of circular tubes of various lengths. The results closely agreed with numerical prediction. The model proves useful for predicting oxygen saturation of blood flowing in a round tube. However, it can only be applied to simple geometries.

In 1971, Weissman and Hung [56] modified the model of round tube to simulate diffusion of oxygen in blood flowing in a rectangular channel. Mass balance equation was used to simulate the diffusion. The model would solve for three-dimensional distribution of oxygen saturation in the domain. Later, Hung [57] applied the same model to numerically predict the oxygen uptake by the blood flowing in rectangular channels. The predicted performance agreed with the experimental results. The model is useful in predicting oxygen uptake and oxygen saturation distribution. However, the model can be computationally intensive when applied to complex geometries. Hence, simpler models were sought.

In 1998, Hewitt *et al* [58] set up a mathematical model to predict oxygen uptake by blood flowing in a cross-flow type hollow fiber oxygenator. Unlike previous models, computationally less intensive equations were used. Instead of resolving distribution of oxygen saturation in the device, overall oxygen uptake was solved. This was done using transport equations such as Fick's law that uses equivalent permeability of the blood film as well as the membrane. In 2008, Lee *et al* [46] used a similar model to predict oxygen uptake of blood flowing in various types of microfluidic devices. In 2013, Potkay [59] used similar strategy to find oxygen uptake by blood flowing in straight channels. The mathematical model formed an analytical solution to find the overall oxygen uptake.

None of these models can fully simulate an oxygenating unit of a lung assist device in the case when the gas permeable membrane expands under operation. This effect was observed in designs where one side of the membrane is exposed to ambient atmosphere and does not have a dedicated gas flow channels with pressurized air or oxygen flow. Since the vascular channels on the other side of the membrane is pressurized, it leads to membrane expansion which changes the geometry of the channels. As a result pressure generated by the blood

and membrane deflection need to be calculated prior to the oxygen uptake is solved. Such a model is developed and presented in chapter 5.

The chapter reports historical development of microfluidic oxygenator. The chapter begins with initial prototypes of direct oxygenators such as bubble oxygenator and film oxygenator. Such devices could provide enough oxygenation, but high dead volume and observed cases of blood trauma discouraged usage of such devices and required additional development. Subsequently, various types of membrane oxygenators were introduced. Hollow Fiber Oxygenator is currently state of the art technology used in clinical setting for respiratory support. Such devices could provide enough oxygenation to the blood, but they exhibit high pressure drop and high dead volume. As a result, further development was needed. Later, research in microfluidics introduced a new form of oxygenators with dimensions closer to the ones in a natural lung. Such devices feature small priming volume, high surface area, and high gas exchange. For this reason, microfluidic approach has been pursued in the development of artificial placenta. However, currently available devices fail to provide enough oxygenation with a maximum change in oxygen saturation of 2.5% at the operating pressure and also the devices studied so far often exhibited have high pressure drop.

Chapter 4 – Design, Fabrication, and Experimental Setup

This chapter introduces various designs investigated in this thesis along with the device fabrication process and experimental setup to test the devices. The designs were categorized based on the type of vascular network and the type of membrane used. Subsequently, the fabrication process for each of these designs have been described. Finally, the setup for various experiments have been presented. In particular, these setups were used to measure the burst pressure of a device, membrane expansion, hydraulic resistance of a device for water, and oxygen uptake and hydraulic resistance of a device for blood.

4.1 Design Constraints

The development of an oxygenator for neonates with RDS is a constrained optimization problem. The constraints for the problem are derived from the operating conditions in a clinical setting such as blood pressure, blood flow rate and initial oxygen saturation. Another important parameter is the dead volume of the device although it is not as critical as the pressure, flow rate and the oxygen saturation level that needs to be obtained.

The perfusion pressure used for extracorporeal membrane oxygenation in a cardiopulmonary bypass surgery varies between 20 – 50 mmHg [60] and is similar to arterio-venous pressure drop required for a pumpless artificial placenta. The mean pressure was taken as 30 mmHg.

Systemic blood flow rate in a neonate is 200 ml/min/kg [61]. The flow rate for the artificial placenta will be a fraction of the systemic flow rate. Rochow *et al* [62] proposed maximum flow rate for the artificial placenta to be 30 mL/min/kg, which is the maximum a neonate can sustain in the case of ductus arteriosus.

The design of this artificial placenta is modular and is made up of multiple oxygenating units that could be added or removed to accommodate neonates of various weights. Each oxygenation unit is required to oxygenate blood at the flow rates more than 1 ml/min so that the total number of oxygenation units that are combined together to form the artificial placenta device can be kept manageable at less than 30 units.

Also, the constraint for the oxygenating capacity of the device comes from the guidance for cardiopulmonary bypass oxygenators by FDA [63]. The device should be able to increase the oxygen saturation of the blood from 65% to 100%. Though it should be noted the in-utero arterial oxygen saturation is 62% in healthy fetuses [64]. Since the baby inside the womb is hypoxic a smaller increase in oxygen saturation provided by the oxygenator would be sufficient although a higher increase in desirable.

4.2 Designs

In this section, various designs have been discussed. All the designs studied in this thesis featured a microvascular network of fluid channels that sits on top of a gas permeable membrane. The task of the network is to facilitate distribution of the blood and formation of a thin layer of blood adjacent to a gas permeable membrane to enable oxygenation. The designs are categorized based on the type of vascular network and the type of membrane used. In this study, two types of vascular network and two types of membrane were used.

The two types of vascular network that were tested in the study are termed as flat and sloping profile. Flat and sloping profile devices differed in terms of their cross-sectional height profile. The height of the flow distribution network remains constant between the inlet and the outlet in the flat device while it varies in the stream-wise direction (decreases till the mid-point and then increases back to the original height) in case of sloping design.

The design for flat device is similar to a previous design published from our group and is used for comparison purposes [53]. Figure 4.1 illustrates anatomy of the device. The blood enters the device through a circular tubing (4.1 mm I.D) as inlet and takes a 90 degrees sharp turn and enters the vascular network. The vascular network featured an array of square support pillars that separates microfluidic channels. The purpose of the pillars is to provide support to the large area thin membrane made of Polydimethylsiloxane (PDMS) that is highly oxygen permeable and which enables oxygenation of blood in the microfluidic channels. Without the support from the pillars, the PDMS membrane which is thin and elastic and could collapse to the bottom during fabrication or balloon out significantly when a positive pressure is applied to the oxygenator during operation. Furthermore, presence of uniformly spaced pillars promotes uniform distribution of the flow as the fluid path length from inlet to outlet is independent of the path. A gas permeable membrane sits at the bottom of the channels which facilitates gas exchange between the blood and the atmosphere.

The dimensions of the device are shown in the figure 4.1. Initially, devices with 500 µm pillar size and 500 µm pillar spacing were fabricated and tested. However, the membrane would delaminate under operation conditions described above, in such devices. Hence, the pillar size was increased to 1x1 mm which prevented delamination. The height of the

device was chosen at 100 µm as it was in the range of heights that could be fabricated using photolithography. Furthermore it matched with the previous design and could be used to compare the various design modifications made in this thesis [53]. The photolithography equipment available at McMaster could accommodate Silicon wafers up to 3 inches (76.2 mm). These wafers were used as a substrate of the molds in the fabrication of the oxygenator and therefore restricted the maximum width of the oxygenator to $1.5\sqrt{2}$(53.8 mm). Also, an additional clearance of 5 mm is needed to allow cutting of the device. Hence, the total width was taken as 43 mm to cover the maximum area on the mold.

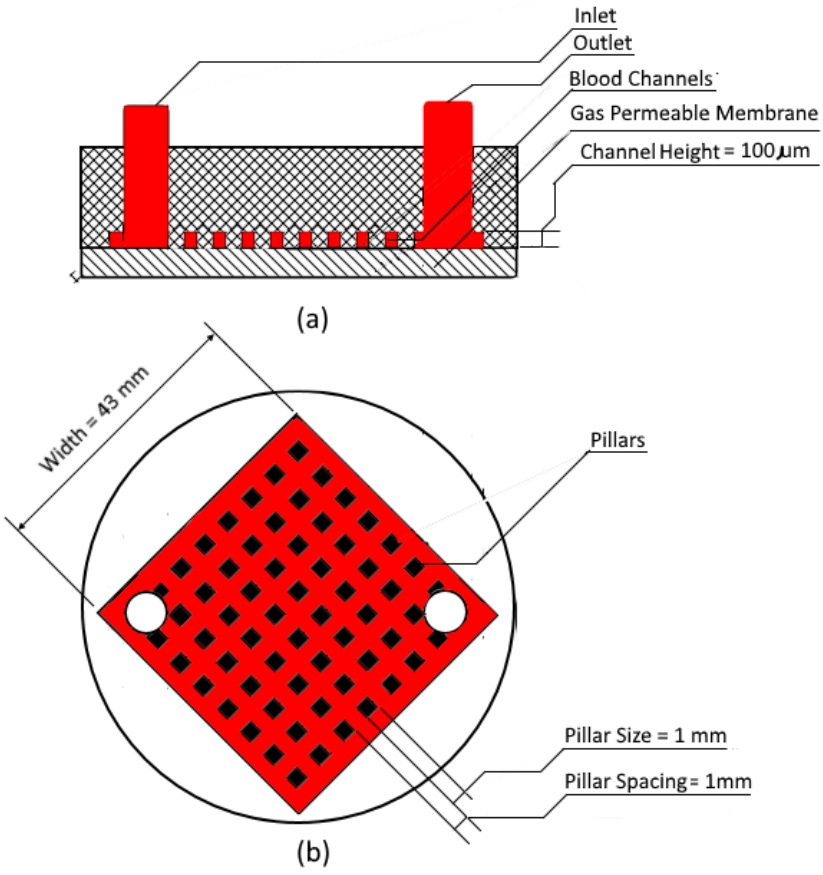

Figure 4.1 Illustration of a flat device. (a) Shows the front view of the device and it shows membrane connected to blood channels (b) Shows the top view of the device showing the array of uniformly spaced square pillars.

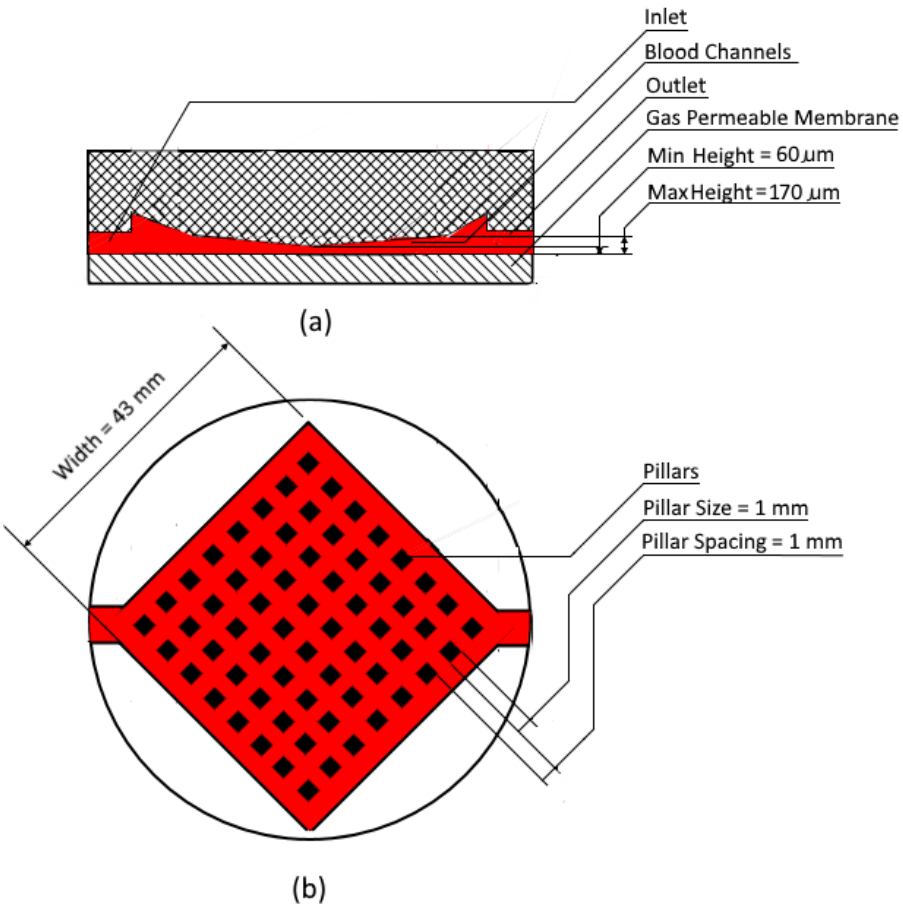

Figure 4.2 Illustration of a sloping profile (a) Shows the front view of the device and it shows membrane connected to blood channels. It also illustrates sloping profile of the blood channels and side inlets. (b) Shows the top view of the device showing the array of uniformly spaced square pillars.

The sloping design, as shown in figure 4.2, was derived from the flat design. In this design, the height of the channels decreases linearly at a rate of 5.12 µm/mm in the stream-wise direction from 170 µm at the inlet to 60 µm at the center of the device after which the height starts to increase linearly at a rate of 5.12 µm/mm back to 170 µm at the outlet. The support pillars were 1 mm square. For comparative analysis, the total width was 43 mm to keep the gas exchange area for the device equal to that of a flat design. Also, the device features horizontal inlet and outlet. Such geometry eliminates sharp bends in flow which causes pressure drop to reduce.

The performance of two types of membranes on both these oxygenator designs was also investigated. The first type consisted of a double layered sandwich of PDMS membrane, which was 50 µm in total thickness. The second type was a 50 µm thick composite membrane with a 39±2 µm thick fine steel mesh (MS-400/19, Asada Mesh Co. Ltd.), made out of 19±1 µm steel wire embedded into a thin PDMS membrane.

The membrane plays an important role in oxygenator by separating the blood from external environment. Gases can easily permeate through the membrane while other contaminants including bacteria or dust particles from ambient are kept away. The choice of material for membrane depends on various criteria such as permeability to gases, mechanical strength, and ease of fabrication. PDMS is a material of choice due to its high gas permeability (6.0×10^{-9} ml $O_2\cdot cm\cdot s^{-1}\cdot cm^{-2}\cdot mmHg^{-1}$).

However, PDMS is also elastic and thin membranes formed of it exhibit significant deformation under pressure which contributed to poor oxygenation in earlier designs. Therefore, alternate membranes that demonstrate high stability, low deformation under pressure, and high gas exchange was desired. One way to fabricate such a membrane was to embed a fine steel mesh as a reinforcement into a thin PDMS membrane. But such a mesh will reduce the gas exchange area for the membrane, which may adversely affect oxygen uptake.

Figure 4.3 shows the orthographic views of the mesh. The mesh has 45 µm square open units and has an overall open area of 51%. The mesh is woven from a thin steel wire of diameter 19±1 µm. Mesh with a thickness of 39±2 µm was chosen.

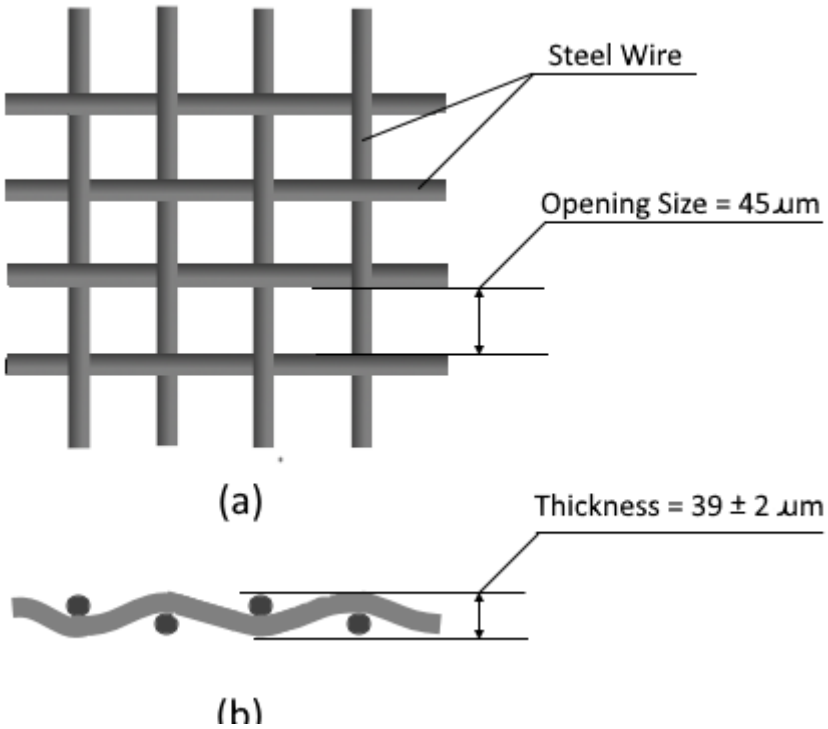

Figure 4.3 Illustration of the steel mesh. (a) Shows the top view of the mesh illustrating its opening area. (b) Shows the side view of the mesh illustrating the thickness of woven steel mesh.

In total, there are 4 types of designs tested in this study: sloping with PDMS only membrane, flat with PDMS only membrane, sloping with composite membrane, and flat with composite membrane. In the next section the fabrication of such devices is covered. Later, performance characterization strategy, and experimental set up to test them is discussed.

4.3 Fabrication & Quality Testing

The fabrication of an oxygenator device is a multi-staged process. The two parts of the oxygenator, namely, the vascular network and the membrane are fabricated separately. After this step, the two parts are activated using oxygen plasma and brought in contact to

make a strong bond. Subsequently, the devices undergo integrity testing, in which they are tested to determine if they can withstand pressure up to 50 mmHg for 30 minutes.

Process of fabrication of the vascular network of flat design is laid out in figure 4.4. First, a mold which is a negative template of the desired microfluidic network, is fabricated as shown in figure 4.4(Ia). For the case of the flat design, the mold was made by exposing a negative photoresist (SU8-100, Microchem) spun on a Silicon wafer (Universal Wafers - 3 inches) through a mask which defines the pattern of the microfluidic network, by photolithography. After exposure the wafer is developed in the photoresist developer and dried. Next, Polydimethylsiloxane (PDMS) pre-polymer was cast on the mold as shown in figure 4.4 (Ib). The PDMS pre-polymer (2 part kit Sylgard TM 184 from Dow Corning) was prepared by mixing the base and the curing agent in 10:1 ratio by weight. The mixture was degassed in a vacuum chamber for 10 minutes to eliminate hydrogen released during the mixing process. Silicone tubing (MasterFlex Platinum Cured Silicon L/S 16, Cole-Palmer) was cut into 4 mm long tubes and placed on top of the diagonally opposite corner of the square pattern as inlet and outlet. Subsequently, 10 grams of the mixture was poured onto the mold. The mold was placed in an oven at 80^{o} C for 2 hours. The liquid pre-polymer cross links forming an elastomer via hydrosylilation reaction between the base and the curing agent [65]. Once solidified, the PDMS was cut out, peeled and the inlet/outlet were cleaned of any residual PDMS (figure 4.4 (Ic)). The detailed process flow is provided in the appendix A.

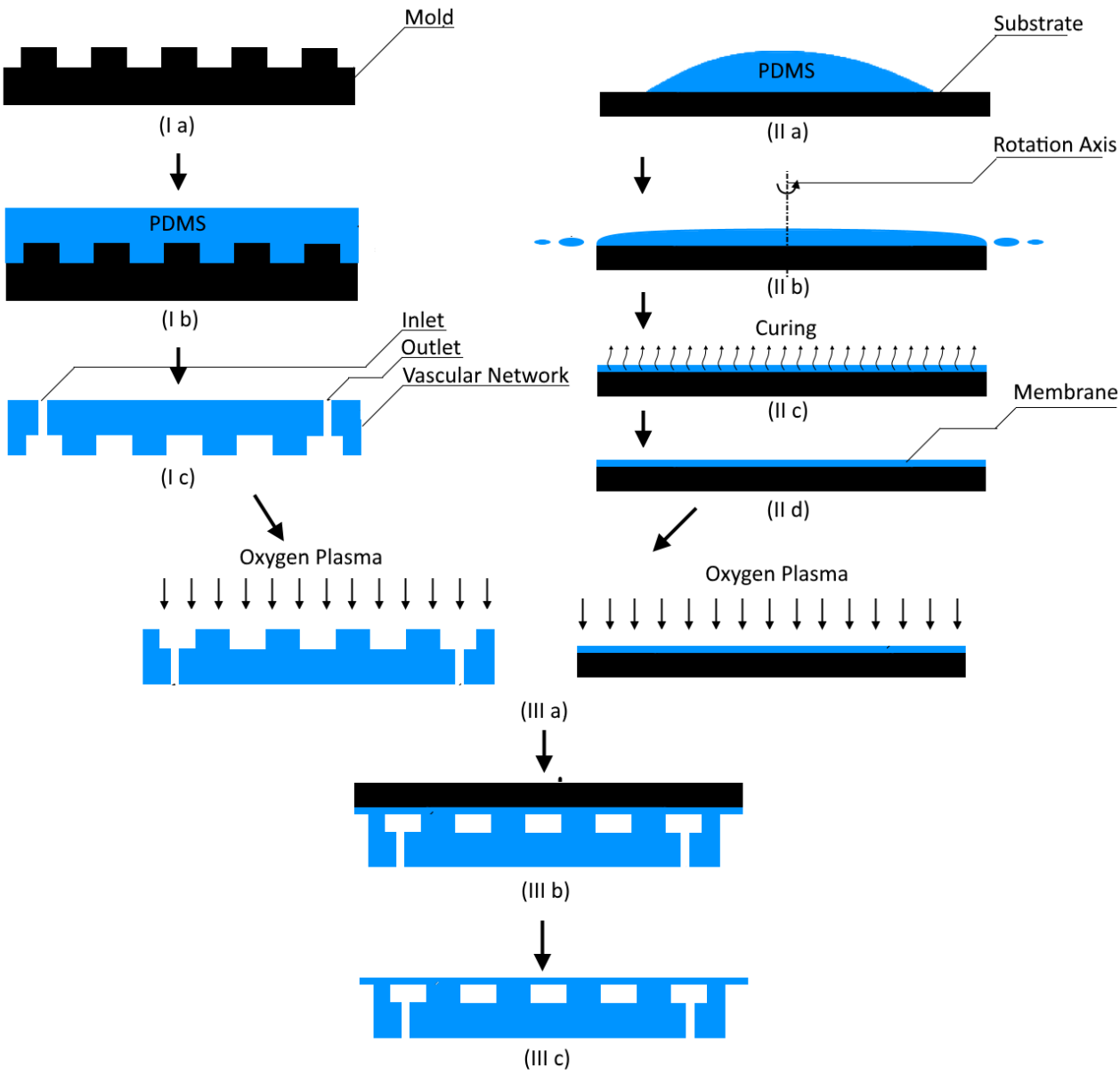

Figure 4.4 Fabrication process of a device (Ia) Mold is prepared. (Ib) PDMS is poured on the mold, (Ic) Once cured, the PDMS is peeled off and holes are punched for inlet and outlet, (IIa) PDMS is poured on to substrate, (IIb) the substrate is spun, (IIc) PDMS is cured, (IIIa) The vascular network and the membrane are exposed oxygen plasma, (IIIb) Vascular network and the membrane are brought in contact, (IIIc) The device is peeled off the substrate.

The process of fabricating the vascular network for sloping design is similar to flat device. PDMS is prepared by mixing the base and the curing agent in 10:1 ratio and is used to cast the device on the mold. The mold for sloping design is machined on an aluminum block

using a tool of diameter 500 µm on a 5-axis micro-milling machine (Matsuura LX-1, Matsuura) available at the McMaster Manufacturing Research Institute.

PDMS membrane is fabricated by spin-coating a thin layer of PDMS pre-polymer on a substrate (figure 4.4 IIa – IIc). The substrate was made of a teflon sheet (Z278793, Bytac surface protection laminate, Sigma Aldrich) adhered on top of a silicon wafer for an easy release of the membrane. First, 1 ml of PDMS is measured and poured on the substrate as shown in figure 4.4(IIa). Second, the substrate is spun at 4000 RPM for 30 seconds. PDMS is forced to move radially outwards because of centrifugal forces as shown in figure 4.4(IIb). As a result, a thin layer of PDMS pre-polymer is formed on to the substrate. The substrate is then placed in an oven at 60^{o} C for 5 hours to cure PDMS into an elastomer (figure 4.4(IIc)). The thickness of the resulting membrane is 25 µm.

Composite membrane is prepared by spin coating a thin layer of PDMS on a substrate at 4000 RPM for 30 seconds. A piece of 39 ± 2 µm thick steel mesh cut into 50 cm X 50 cm dimension is gently laid on the uncured PDMS layer. The resulting product is cured in an oven at 60^{o} C for 5 hours. Later, another layer of PDMS is spin-coated on top of it at 4000 RPM for 30 seconds and cured at 60^{o} C in an oven for 5 hours. The thickness of the membrane is 50 µm.

Once the vascular network and the membrane are fabricated, they are bonded to each other by exposing their surfaces to oxygen plasma at a 500-550 mTorr of pressure and 50 W power for 2-2.5 minutes, as shown in figure 4.4(III a). The exposure activates the surfaces and when brought in contact form a strong bond with each other as shown in figure 4.4(III b). The device is placed in an oven at 60^{o} C for 4-6 hour to strengthen the bond before it is released off the Teflon substrate (figure 4.4(III c)). Two PDMS membrane are bonded in

the case of device with PDMS membrane while a single membrane is bonded in the case of devices with composite membrane.

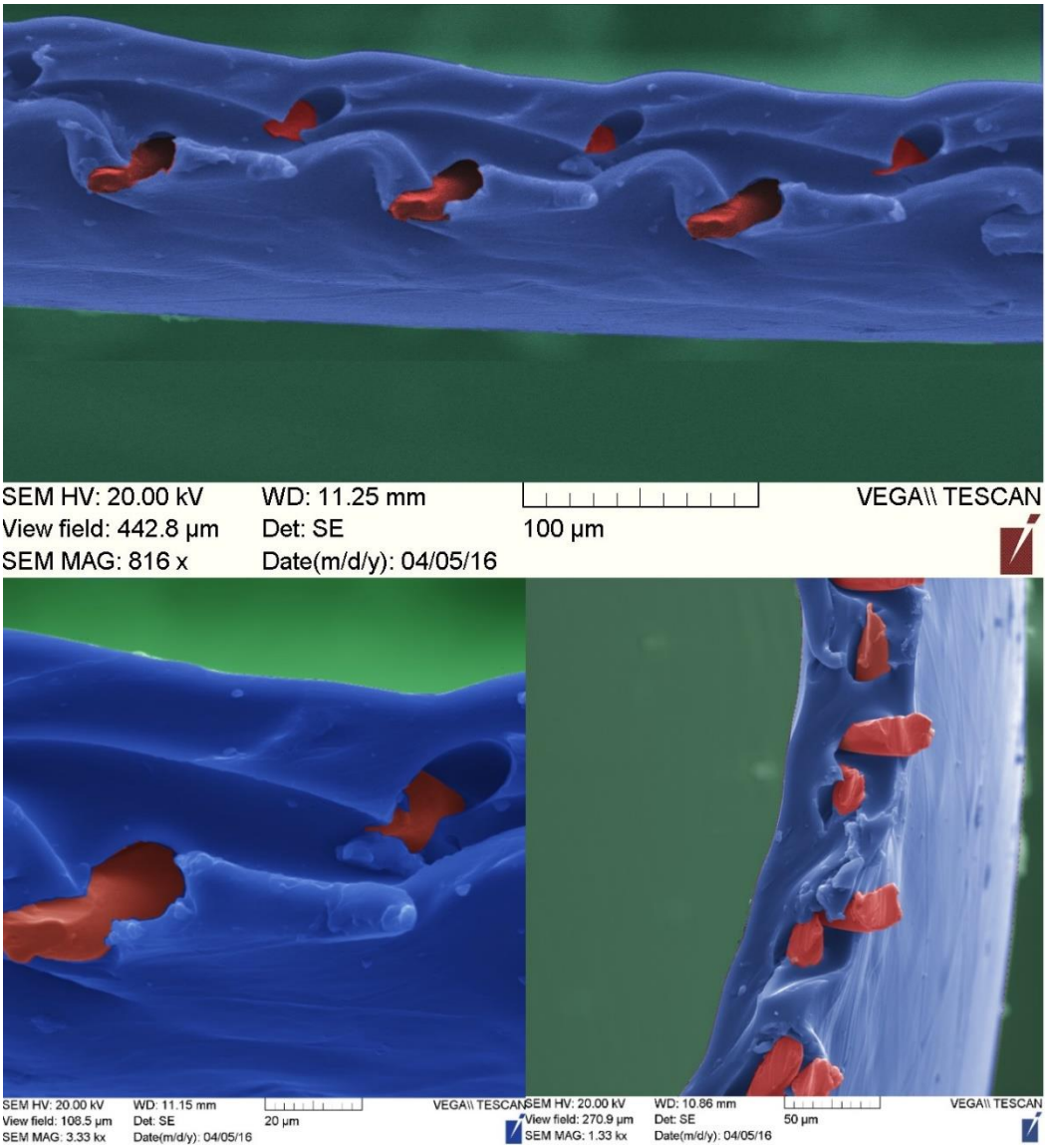

Figure 4.5 SEM picture of the cross-section of a composite membrane. The picture is false colored to distinguish PDMS (blue) from steel mesh(red)

Once prepared, the devices undergo integrity testing. This step is done to ensure reliability and consistency in performance of the device in the subsequent testing. Water is made to flow through the device at the operating pressures and flow rates. Devices able to withstand

such conditions are promoted to subsequent testing with blood. In the next section, experimental procedure to measure oxygen uptake capacity and pressure drop is detailed.

4.4 Experimental Setups

Experimental setups used to test the performance of the fabricated devices have been presented in this section. In particular, the setups are used to measure burst pressure, membrane expansion, hydraulic resistance for water, oxygen uptake of an oxygenator and hydraulic resistance for blood. The setup to measure oxygen uptake and hydraulic resistance for blood are identical, while for other applications separate setups are used.

4.4.1 Experimental Setup for Burst Pressure Measurement

Burst pressure is a critical parameter that determines the operational range of the device. Typically the operating pressure range is set to a factor smaller than the measured burst pressure. This factor is known as the factor of safety and typical values range from 2-3. Therefore, required operating pressures of (20 – 50 mmHg) require the burst pressure to be higher than 100-150 mmHg.

In order to measure the burst pressure of the device, a serial fluidic circuit containing a syringe, pressure transducer, and oxygenator connected by PVC tubing was used (figure 4.6). The syringe was filled with water and was used to perfuse the circuit. A pressure transducer (TruWave Transducer, Edwards Lifesciences LLC, Irvine, CA, USA) is used to measure the pressure in the system. The pressure transducer was connected to a pressure monitor (SpaceLabs 90369 Patient Monitor, SpaceLabs Medical Inc) which reports the pressure value. At the end of the circuit, a 3-way connector was added at the outlet to control the flow of water.

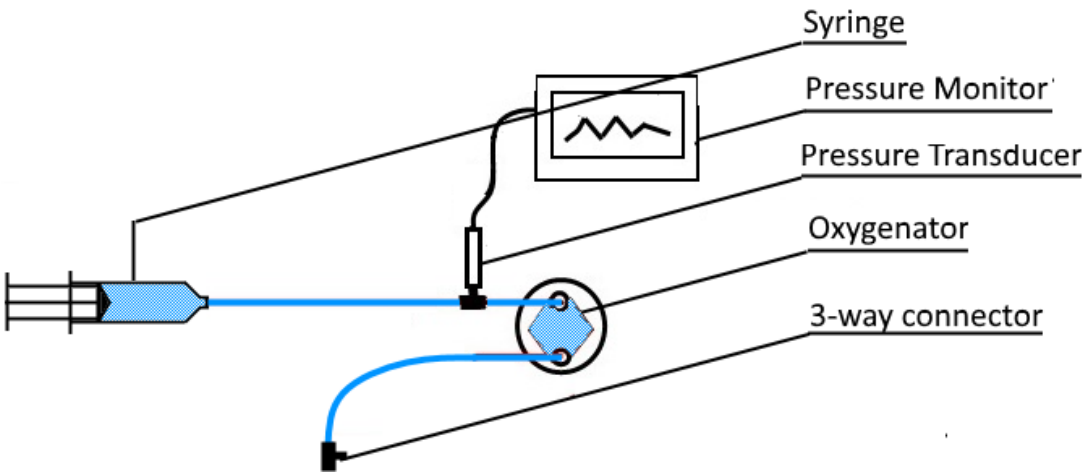

Figure 4.6 Experimental setup for burst pressure measurement.

First, the 3-way connector was kept open to the atmosphere and the circuit was perfused with water using syringe. Once the circuit was perfused, the outlet was tightly closed by closing 3-way connector and the pressure was set to zero. Now, water was manually forced into the circuit using syringe causing pressure to rise and oxygenator membrane to expand. The process is continued till the device failed. The pressure at failure was recorded with an error of ±1 mmHg

4.4.2 Membrane Expansion

The membrane used in the current study is made out of silicone and is flexible in nature. As a result, when a device is under operation the membrane expands under hydraulic pressure. It is essential to gather data on membrane expansion to further the understanding of oxygen uptake. As a result, a setup to measure membrane expansion was built.

The setup is shown in figure 4.7. A fluidic circuit containing syringe, pressure transducer, and oxygenator connected with PVC tubing was built. The syringe was filled with water and was used to perfuse and pressurize the system. The pressure transducer (TruWave transducer, Edwards Lifesciences LLC, Irvine, CA, USA) was used to measure the pressure

in the circuit. The oxygenator was laid out flat under an optical surface profiler (Newview 5000, Zygo) for inspection. A 3-way connector was added at the outlet of the oxygenator to control the flow.

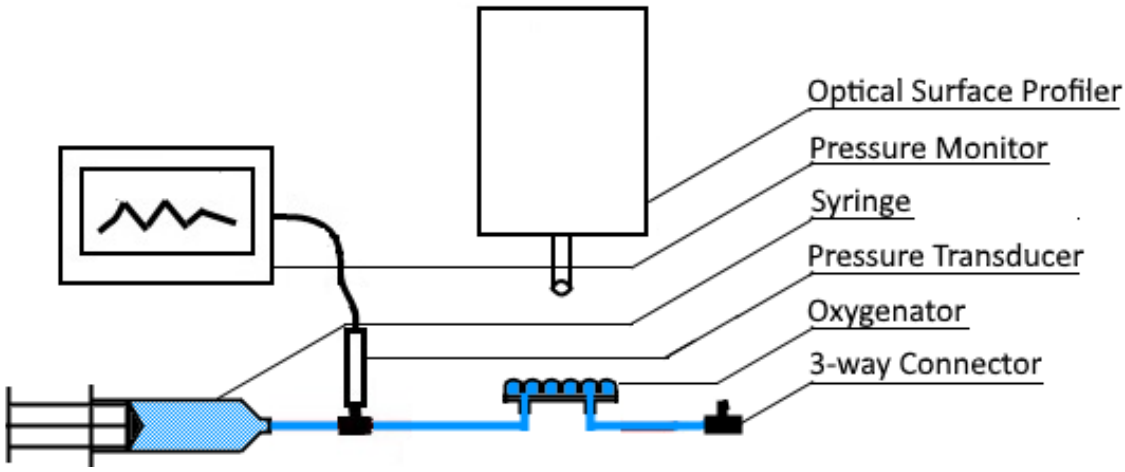

Figure 4.7 Experimental set up for measuring membrane expansion.

In the beginning, the outlet of the oxygenator was open to the atmosphere and the circuit was perfused with water. Once the circuit was perfused, the outlet of the oxygenator was tightly closed using 3-way connector and the pressure was set to zero. The coordinates of the plane of the membrane were measured using the surface profiler for reference. Then, water was forced into the circuit using syringe. As a result, the pressure rose and the membrane expanded. Then maximum height was measured in two different zones (figure 4.8) by measuring the difference between the coordinates of the plane of the membrane when it is at rest and the plane that touches the membrane surface profile in different zones. Zone 1 represents the area at the center of four adjacent pillars located on the corner of a square. Zone 2 represents the region between any two adjacent pillars in the horizontal or the vertical direction.

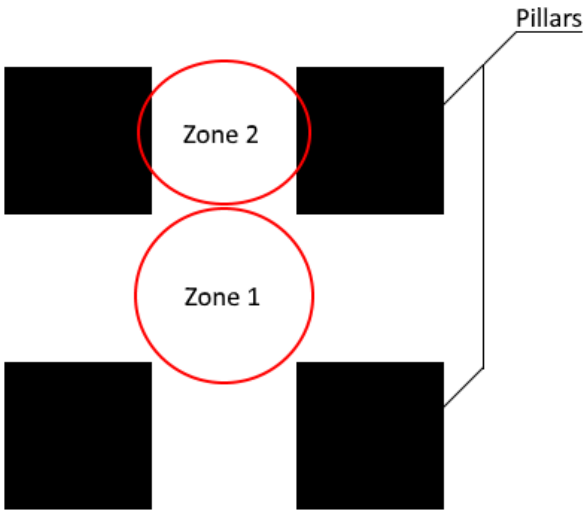

Figure 4.8 Illustration of zones for which the maximum deflection is measured.

4.4.3 Hydraulic Resistance with Water

The flow characteristics of each of the fabricated oxygenator device was tested using water, to ensure that they were similar and could sustain similar flow under the pressures applied.

The setup is shown in figure 4.9. A closed circuit containing water container, peristaltic pump (ISM832C, Ismatec), pressure transducer (Edwards Lifesciences LLC, Irvine, CA, USA), and oxygenator connected with tubing was built. The water was withdrawn from the container using peristaltic pump and passed through the oxygenator. The water coming from the outlet of the oxygenator was returned back to the container.

Water flow rate was increased at a constant rate from 1 ml/min up to 20 ml/min and corresponding pressure was recorded. Once the pressure reached the maximum operating pressure (50 mmHg), the flow rate was maintained for 30 minutes. If the device did not fail during the operation and its hydraulic pressure was within ±5 mmHg of the mean of the pressure drop of all the devices in that design, the device was considered to have passed the integrity testing.

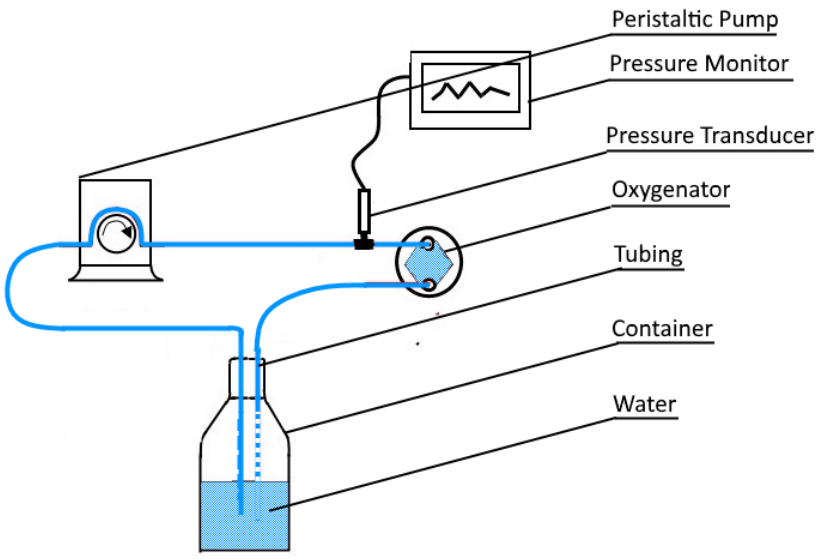

Figure 4.9 Experimental setup to measure hydraulic resistance of an oxygenator for water.

4.4.4 Measurement of Oxygen Uptake and Hydraulic Resistance using Blood

The experimental procedure to measure the performance of an oxygenator is presented in this section. This is an essential step in the development of oxygenator as it lays down the framework to test, validate, and compare various designs of oxygenators. The key performance indicators are the change in oxygen saturation of the blood from the inlet to the outlet of the device, and the pressure drop generated. The performance of an oxygenator is characterized by measuring these indicators at a number of flow rates.

However, before oxygen uptake can be measured, the oxygen saturation of the blood at the inlet needed to be maintained at a set oxygen saturation level during the entirety of the testing duration. The average length of each experiment to measure the performance of a device was between 30-45 min. Therefore, it would take ~2-3 hours to make complete measurements on 4-5 devices that were typically required. Various configurations of

experimental setups were considered in order to maintain oxygen saturation levels in blood for this duration of time and are described below.

4.4.4.1 Deoxygenated Static Blood in a Container

The first configuration considered is shown in figure 4.10. It consisted of a closed loop containing a blood reservoir, a peristaltic pump, a hollow fiber oxygenator, appropriate gas supply and 3 way valve for sample extraction. The blood (Bovine 7200807-500ML, Lampire Biologics) was stored in a reservoir from which it was withdrawn by a peristaltic pump (ISM832C, Ismatec) at a flow rate of 4 ml/min. The pump pushed the blood through a hollow fiber oxygenator (OXR, Living Systems Instrumentation) where it was exposed to a mixture of 5% carbon dioxide and 95% nitrogen at 5 L/hr. This caused the oxygen in the blood to diffuse out leading to a drop in oxygen saturation as a result. The blood at the outlet of the oxygenator was fed back to the reservoir. The blood was sampled from the reservoir and its oxygen saturation was measured at regular intervals using a blood-gas analyzer (GEM3000, Instrumentation Laboratory). Once the oxygen saturation decreased to a desired level, the connection between the reservoir and the pump is closed and all the blood in the system was delivered to the reservoir.

The set point for oxygen saturation in the reservoir for all cases was chosen as 46%. This was done because the relationship between oxygen saturation and the partial pressure of oxygen is linear at 46% oxygen saturation. After achieving the set oxygen saturation level in the reservoir, the system was kept unchanged and the oxygen saturation levels in the reservoir monitored every 5 min for about an hour. This procedure was repeated 5 times.

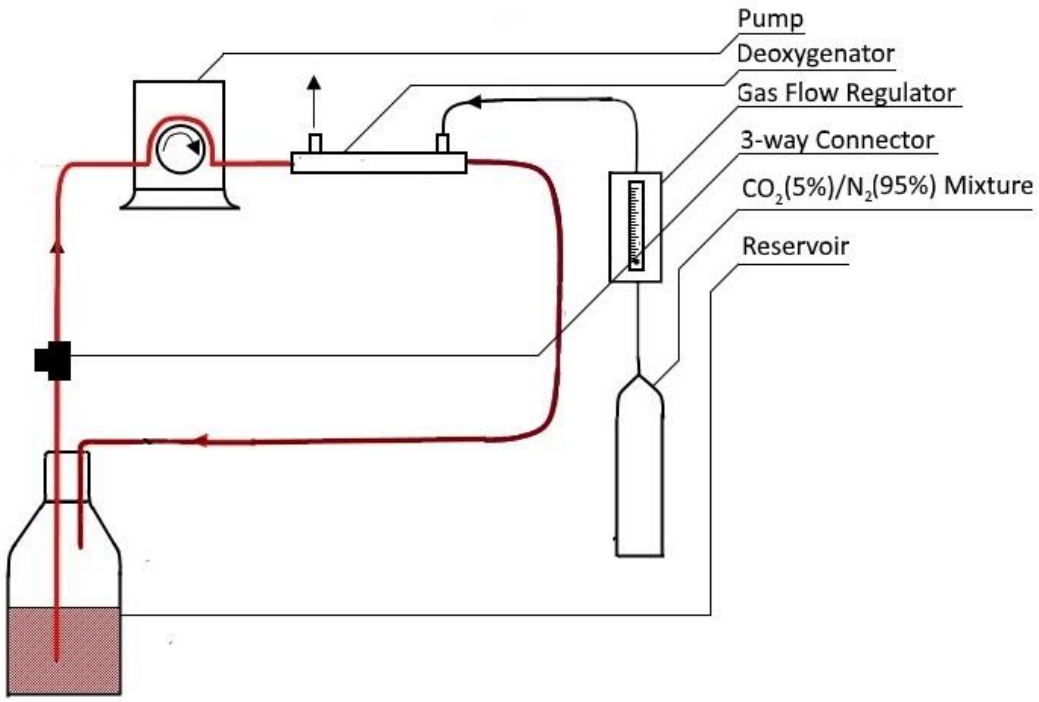

Figure 4.10 Experimental setup to set the oxygen saturation of the blood

The results are plotted in figure 4.11. The set oxygen saturation (46%) was reached using the experimental setup in all 5 cases, with time taken to reach the point varying between 1-2 hours (data not shown). Nevertheless, when the blood in the reservoir was maintained static over an hour the oxygen saturation was found to increase with time and changes by more than 9% from the set point. The increase in oxygen saturation was due to the diffusion of oxygen from the ambient where its partial pressure is 156 mmHg into the blood where its partial pressure is only 27 mmHg at 46% saturation. It can be seen that the variation of saturation over the duration of just one hour crossed the limit of +/-5%. Therefore, this configuration was found unsuitable to maintain the oxygen saturation levels in the blood reservoir over the intended duration of time required for the experiments.

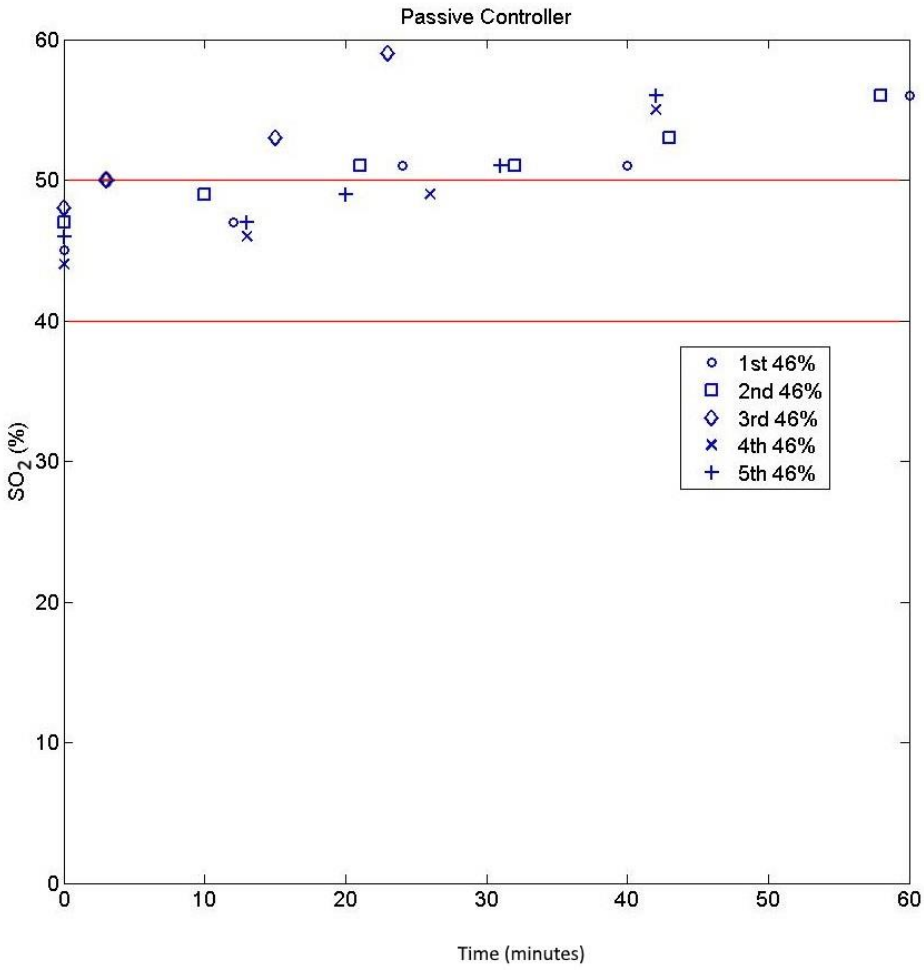

Figure 4.11 Variation of oxygen saturation of the blood in the system with time for passive controller. The oxygen saturation is set at 46% also the maximum deviation (sO_2 = ±5%) from the set point is indicated on the graph by red lines.

4.4.4.2 Active Controller

The new experimental setup is termed active controller is shown in figure 4.12. The system consisted of a reservoir containing bovine blood, peristaltic pump, an oxygenator, oxygen gas flow regulator, 3-way connectors for sampling, carbon dioxide/nitrogen mixture flow regulator and a deoxygenator. Blood (Bovine 7200807-500ML, Lampire Biologics) was stored in a container and a peristaltic pump (ISM832C, Ismatec) was used to pump it through two hollow fiber oxygenators connected in series at a flow rate of 4 ml/min. The first oxygenator (CAPIOX RX05, Terumo) immediately next to the pump used 20 L/hr of

oxygen and fully oxygenated the blood (100% saturation). In the second oxygenator that is located downstream (OXR, Living Systems Instrumentation), the blood was deoxygenated to the desired setpoint by controlling the flow rate of carbon dioxide and nitrogen (5%/95% v/v) to it. The flow rate of the deoxygenating gases in the second oxygenator was titrated by measuring the oxygen saturation of blood at the sampling point every 5 min till it reached the set point and remained steady.

The active controller was later tested for its ability to keep the oxygen saturation at the set level for an hour. The oxygen saturation is set at 46%. The test was repeated n=5 times for reliability for different blood samples. If a variation of ±5% was observed, then the controller was shut off.

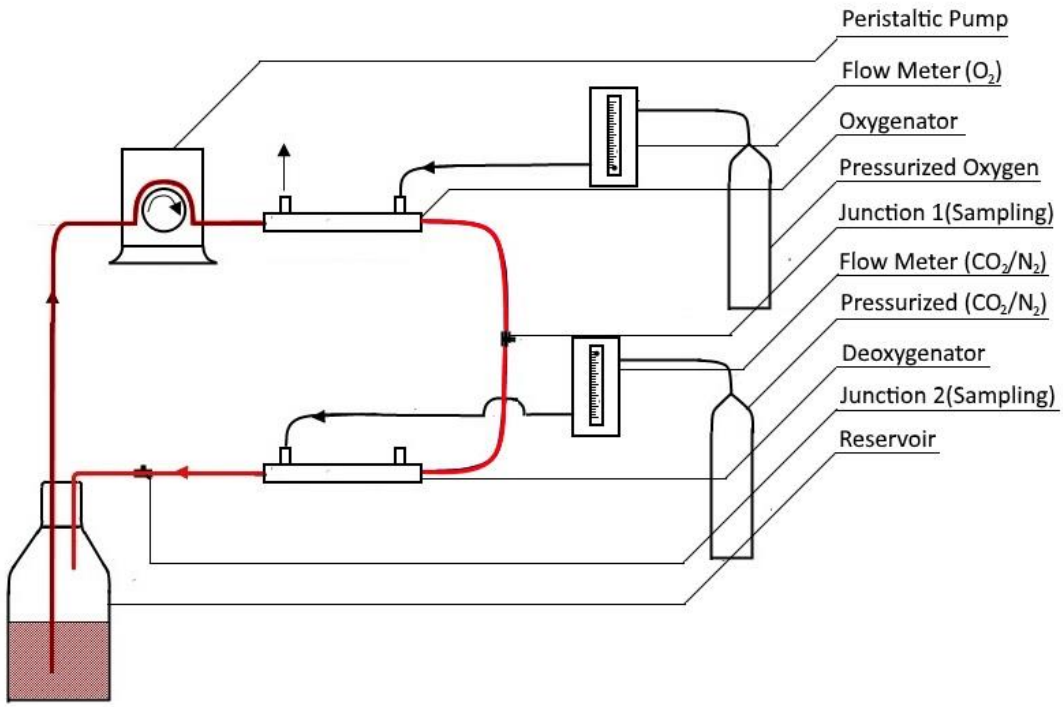

Figure 4.12 Illustration of the experimental setup of the modified setup.

The results are shown in figure 4.13. The oxygen saturation remained within the limit of ±5%, represented by two parallel horizontal red lines, for at least an hour for active controller. Maximum deviation observed from the set point was ±3%. The results aligned with the expectations as the controller balanced oxygen uptake by the ambient atmosphere and the oxygenator, and oxygen release by the deoxgenator. It was established that active controller is a reliable method to test the devices in subsequent experiments.

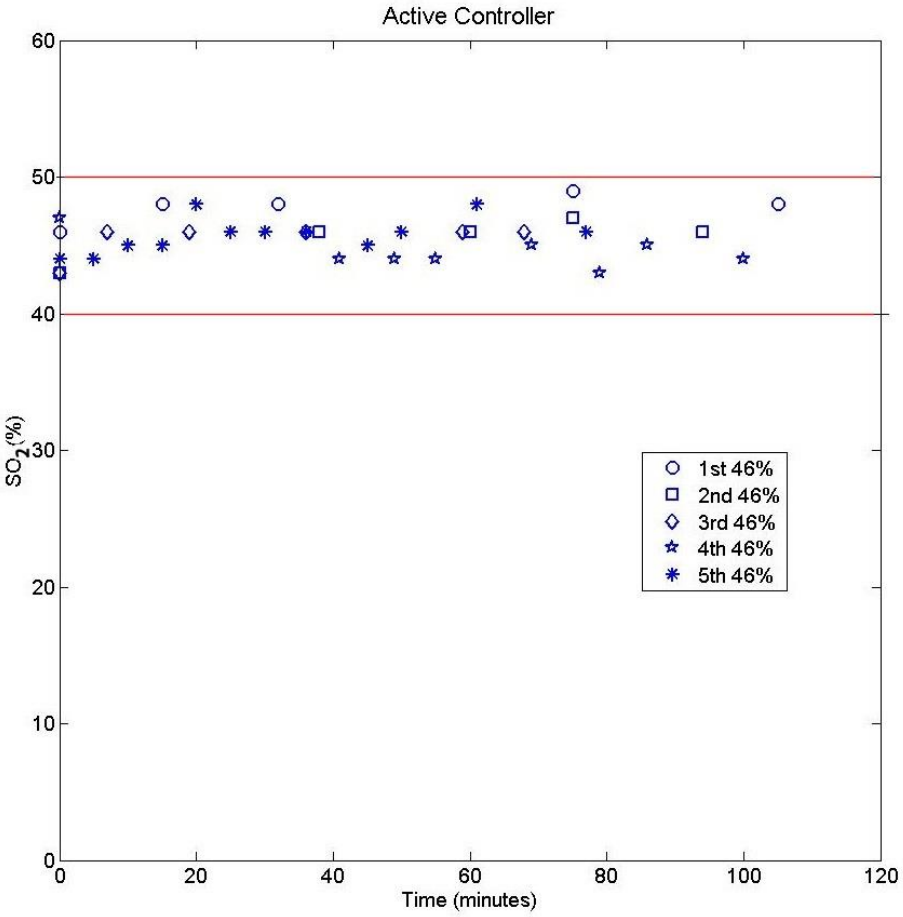

Figure 4.13 Variation of oxygen saturation of the blood in the system with time using active controller.

Once the oxygen saturation was set, the performance of an oxygenator characterized by change in oxygen saturation and pressure drop as a function of flow rate could be measured.

4.4.4.3 Performance Measurement

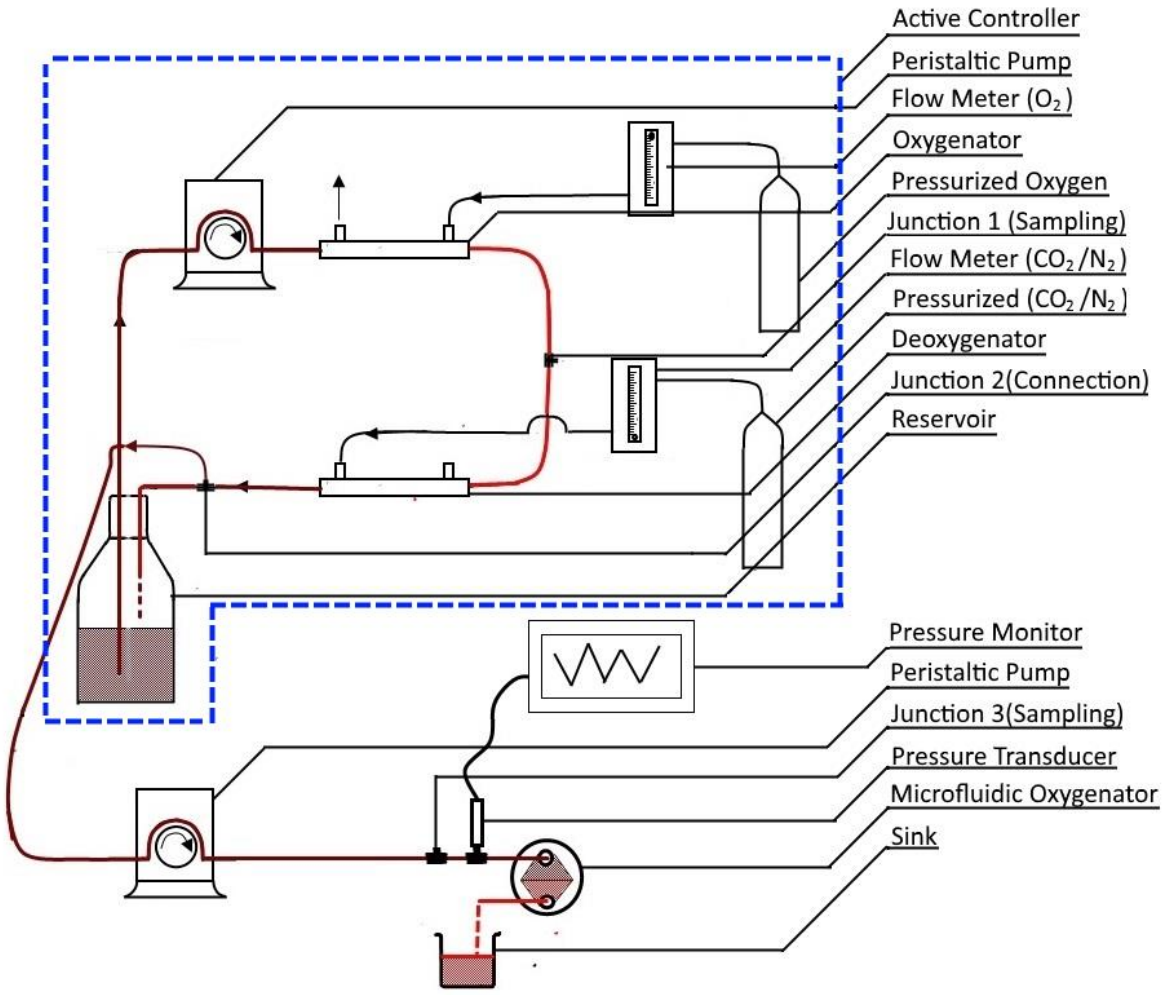

Figure 4.14 Experimental setup to test the oxygenator

Figure 4.14 shows the experimental set up consists of an active controller as previously described, a peristaltic pump, a 3-way connector as a junction for sampling, pressure transducer, pressure monitor, microfluidic oxygenator, and a sink. The blood (Bovine 7200807-500ML, Lampire Biologics) was contained in a reservoir and its oxygen saturation was maintained at a set point using active controller as explained above. The blood withdrawn from the reservoir using a peristaltic pump (ISM832C, Ismatec) with flow rate ranging in between 0.5 – 4 ml/min and pushed through the oxygenator device. Blood

was sampled at the entry and the exit of the device, and analyzed using a blood gas analyzer (GEM3000, Instrumentation Laboratory). Difference between the oxygen saturation of the blood reflected the oxygen uptake capacity of the device at the given blood flow rate. Also, a pressure transducer (TruWave Transducer, Edwards LifeSciences LLC, Irvine, CA, USA) was connected immediately before the device to measure the pressure drop.

In summary, the chapter discussed various designs tested in this study. Each design featured a vascular network that sits on top of a gas permeable membrane. The height distribution of the fluid channels in the network may have a sloping or a uniform profile. Two different configuration of the gas permeable membrane - homogenous PDMS membrane or steel mesh reinforced PDMS membrane - were considered.

The fabrication process of the microfluidic device was discussed. The vascular network was fabricated by conventional molding technique, by curing PDMS onto a mold. Membrane was fabricated by spin coating PDMS on a Teflon substrate and subsequently curing it in an oven. For the composite membrane, the mesh was placed on the uncured PDMS immediately after spin coating the substrate. Once parts were fabricated, they are exposed to oxygen plasma and joined by bringing them in contact.

The first step in the experimental procedure to test these devices was to set the blood oxygen saturation level. The blood was then pumped through the device at a set of flow rates. The device performance was characterized by the change in oxygen saturation of the blood and the pressure generated across the device.

Finally, the experimental setup to control the oxygen saturation level was tested in the chapter. The results showed the setup to be unreliable and hence, a new setup was

developed. The new setup featured a pair of hollow fiber oxygenators, oxygenating and deoxygenating the blood in conjunction. The oxygen uptake by the oxygenating units was balanced by the deoxygenating units. The results showed the modified system to be reliable.

In the next chapter, development of a mathematical model is presented and validated. The model was developed to be able to choose the optimum geometrical parameter for a certain design.

Chapter 5 – Mathematical Modeling

A mathematical model was built to simulate the oxygen uptake and the pressure drop in an oxygenator device. In this chapter, the mechanism of oxygen uptake inside the oxygenator and the processes involved are detailed first. In particular, the four processes at play that affect oxygen uptake: oxygen diffusion, oxygen uptake by hemoglobin, membrane deflection, and generation of hydraulic pressure are explained. Then, the underlying governing equations for each of these processes are determined. Next, the model is simplified by applying various assumptions. In later sections, modifications of the model are developed to simulate various conditions encountered in the experiments. Finally, the model is integrated and validated against the experimental results of a flat device.

5.1 Mechanism of Oxygen Uptake

The mechanism of oxygen uptake in the device can be explained using the schematic in figure 5.1. The blood flows in the channels from the left to the right through the network of microchannels. A gas permeable membrane made out of silicone sits at the bottom of the channels and it separates the blood from the external gas. The device exterior (ambient atmosphere) is rich in oxygen and has a higher partial pressure of oxygen compared to blood inside the device. The gradient in the partial pressure of oxygen causes the external oxygen to diffuse through the gas permeable membrane and into the blood plasma. The diffusing oxygen is initially taken up by the plasma and then subsequently taken up by the red blood cells. This causes oxygen saturation and partial pressure of the blood to rise.

The oxygen diffusion and uptake critically depends on the height of the blood channel and the membrane thickness. The membrane thickness remains unchanged during the operation, however the channel height may change depending on the operating condition. This effect is the result of the elasticity of the membrane. The applied pressure causes the blood to flow through the device and the membrane to expand. The membrane keeps expanding till the applied pressure balances the stresses generated in the membrane.

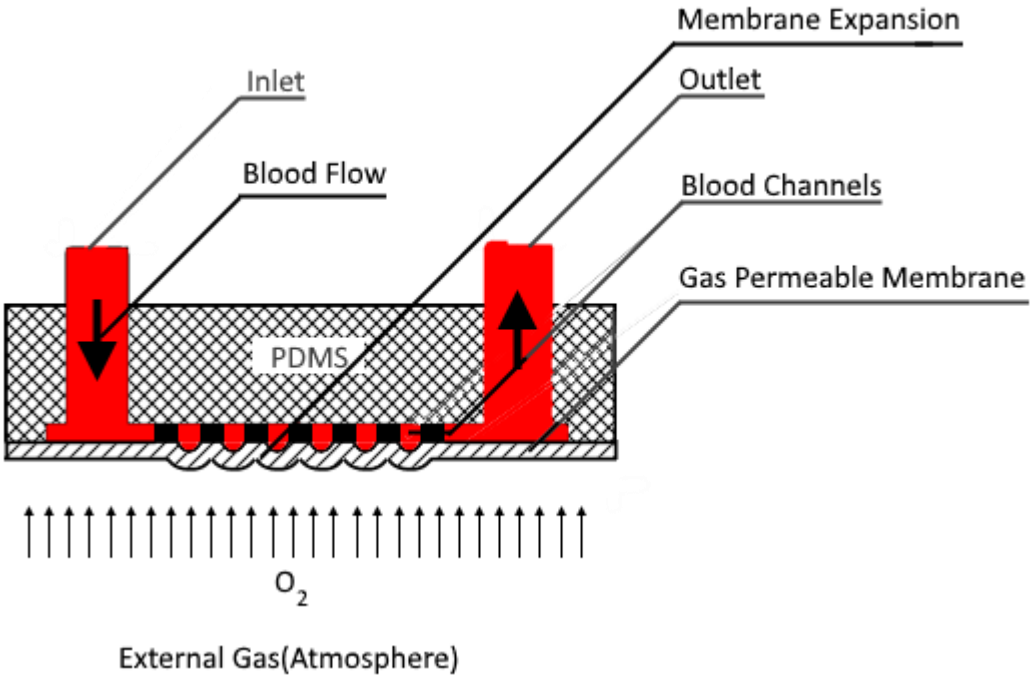

Figure 5.1 Illustration of the mechanism of oxygen uptake. The membrane expands as a result of the applied hydrodynamic pressure. The oxygen flows in the device as a result of the gradient in partial pressure of oxygen.

As a result, it is necessary that the final model incorporates membrane expansion and pressure drop, and couples them with the model to calculate oxygen uptake to accurately predict the performance of the device. In the next section, an overview of the model and the underlying governing equations have been explained.

5.2 Governing Equations, Assumptions and Boundary Conditions

The development of the model followed a multi-step approach. A schematic diagram illustrating the process flow of the development is shown in figure 5.2. First, a model to calculate oxygen saturation is built and validated. Later, a model to calculate the pressure drop is added to the existing code. Finally, a model to simulate membrane expansion is added to the existing code.

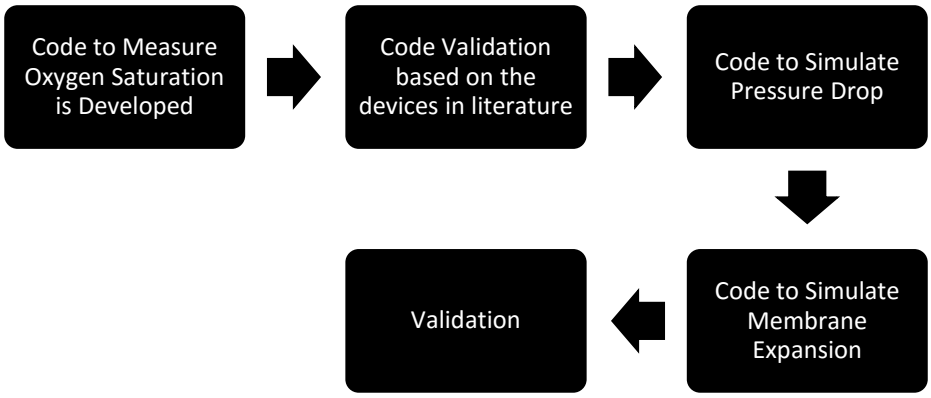

Figure 5.2 Process flow for the development of the mathematical model

Table 5.1 summarizes various governing equations used to calculate oxygen uptake, pressure drop, and membrane expansion. For oxygen uptake, Fick's law is used to calculate the total flux of oxygen diffusing in the blood (see equation (5.1.1)). For any gas G, Fick's law [66] expresses a relationship between the flux (J_g) of the gas through a membrane of permeability $\wp_m$ and thickness t_m, when a partial pressure ΔP_g is applied across it. Once the flux is calculated, corresponding rise in oxygen saturation and partial pressure is calculated using the equation for the oxygen content of the blood and the relationship between the oxygen saturation and the partial pressure of oxygen in the blood. The oxygen content of the blood cO_2 is the sum of the amount of oxygen taken up

by the hemoglobin and the amount of oxygen dissolved in the blood plasma (equation (5.1.3)). The relationship between oxygen saturation and the partial pressure of oxygen in the blood is given by Hill's equation [67].

Table 5.1 List of governing equation for various models

Model	Governing Equations	
Oxygen Uptake	Fick's Law [66]: $J_g = \wp_m \frac{\Delta P_g}{t_m}$	(5.1.1)
	Hill's Equation [67]: $sO_2 \approx \frac{K_{HbO_2}[O_2]}{1+K_{HbO_2}[O_2]}$	(5.1.2)
	Henry's law [68]: $[G] = \alpha_G * pG$	(5.1.3)
	Oxygen Content of Blood [69]: $cO_2 = 1.34 * ch_b * sO_2 + 0.000031 * pO_2$	(5.1.4)
Pressure drop	Ohm's law for Fluid Mechanics [70]: $\Delta P = Q * R_h$	(5.1.5)
	Hydraulic resistance of a rectangular channel [71]: $R_h \approx \frac{12\mu l}{wh^3\left(1-0.63\frac{h}{w}\right)}$	(5.1.6)
	If $\frac{h}{w} \ll 1$, $R_h \approx \frac{12\mu l}{wh^3}$	(5.1.7)
	Carreau Model for Blood Viscosity [72]: $\mu = \mu_\infty + (\mu_0 - \mu_\infty)[\,1 + (\lambda\dot{\gamma})^2]^{\frac{n-1}{2}}$	(5.1.8)
Membrane Expansion	Deflection of a membrane under uniform pressure [73]: $W(r) = W_o\left(1 - \frac{r^2}{R^2}\right)$	(5.1.9)
	Hooke's Law in radial direction [73]: $\in_r = \frac{\sigma_M}{E_r} + \vartheta\frac{\sigma_\theta}{E_\theta}$	(5.1.10)

Hooke's Law in angular direction [73]: $\in_\theta = \frac{\sigma_\theta}{E_\theta} + \vartheta \frac{\sigma_M}{E_r}$	(5.1.11)

The amount of oxygen taken up by the hemoglobin is given by the product of the maximum amount of oxygen in ml taken up by a gram of hemoglobin (1.34 ml/ml), concentration of the hemoglobin in the blood ch_b, and the oxygen saturation sO_2 [69]. The amount of oxygen dissolved in the blood plasma is given by Henry's law [68](see equation (5.1.4)). For any gas *G*, Henry's law [68] relates the concentration of the gas dissolved in the liquid $[G]$ and the partial pressure of the gas pG by a proportionality constant α_G. For oxygen dissolved in blood, the constant of proportionality for Henry's law is 0.000031 ml/mmHg [69]. Hill's equation relates oxygen saturation of the blood sO_2 and the concentration of oxygen $[O_2]$ through a variable K_{HbO_2}, which depends on partial pressures of gases in the blood and the temperature of the blood (see equation (5.1.2)).

The pressure drop is calculated by applying Ohm's law for fluid mechanics, which relates the flow rate Q and the pressure drop ΔP through the hydraulic resistance, which depends on the fluid viscosity, the characteristic dimension, and the length of the channel (equation (5.1.5)) [70]. The blood channels analyzed in the study have a rectangular cross-sectional area. For rectangular cross section area, the hydraulic resistance is given by the expression in equation (5.1.6) [71]. In the expression, μ, w, h and l are the viscosity of the blood, channel width, channel height, and channel length. If the channel width is high compared to the channel width, then the expression can be simplified to the one in equation (5.1.7). The viscosity of the blood is calculated using Carreau model [72] (equation 5.1.8), which relates the viscosity μ at any given shear rate $\dot{\gamma}$ with the viscosity

of the blood at zero shear rate μ_0, viscosity at infinite shear rate μ_∞ and given shear rate $\dot{\gamma}$ through a constant λ and an exponent *n*.

As previously mentioned, the deflection of the membrane and the pressure drop in the device is two way coupled. This is because, the deflection of the membrane leads to a larger cross-sectional area which reduces the pressure drop across the device and consequently the pressure difference across the membrane which then subsequently affects its deflection. Ideally these equations are then solved in an iterative fashion. In addition, the complex geometry of the membrane deflection due to multiple constraints imposed by the pinning of the membranes to the pillars make simulation of the exact membrane deflection profile computationally intensive. As a result, the membrane was modeled by assuming the simplest form of geometry, by using the deflection of a circular membrane under uniform pressure. The expression of the deflection of a circular membrane $W(r)$ at any given radial distance '*r'* under uniform pressure relates the deflection with the radial distance '*r'*, the radius of the membrane '*R'*, and the deflection at the center of the membrane W_o (see equation (5.1.9)) [73]. Hooke's law is used to develop relationship between the shear stress generated by the pressure in the membrane and the deflection (see equation (5.1.10) and (5.1.11)) [73]. Hooke's law for 2D gives two equations. One of the equation relates the shear strain $\in_r$ in radial direction with the shear stress along the radial direction σ_M, the shear stress along the angular direction σ_θ, the Young moduli in the respective directions (E_r and E_θ) , and the Poisson's ratio ϑ. Similarly, the other equation of Hooke's law relates the shear strain $\in_\theta$ in angular direction with the shear stress along the radial direction, the shear stress along the angular direction, the Young moduli in the respective directions, and the Poisson's ratio.

Many simplifications have been made about the physical reality of the oxygen uptake to avoid capturing its microscopic details, while accurately calculating the performance of the device. As a result, following assumptions have been made regarding the model:

1. The flow is uniformly distributed along the width of the device.

   The fluid path length is independent of the path from inlet to outlet in the designs being tested. As a result, the flow is uniformly distributed.

2. The diffusional boundary layer thickness on the blood side is equal to half the channel height.

   The oxygen attempts to travel from the bottom of the channel to the top of the channel, but some of it reacts with hemoglobin on its way. At the beginning of the device, the oxygen binds with hemoglobin as soon as it enters the device, hence less of oxygen travels from the bottom to the top. But in the downstream location, the oxygen has to travel some distance in the channel before binding with hemoglobin. Hence, more oxygen gets travels from the bottom to the top of the channel. Hence, it can be assumed that the average diffusional length of oxygen is half the channel height.

3. Oxygen uptake by red blood cells is instantaneous.

   Once the oxygen diffuses into the blood, it gets dissolved in the plasma. From there, it may remain dissolved in the plasma or bind with hemoglobin. It takes around 20 ms for the oxygen to react with hemoglobin and reach equilibrium. It is assumed the reaction time of oxygen with hemoglobin is negligible as compared to the time oxygen takes to diffuse from the atmosphere. The assumption may not be applicable as the channel dimension reach that of a cell.

4. Partial pressure only varies in the stream-wise direction.

   Averaged partial pressure of oxygen along the height is used to calculate oxygen flux. Partial pressure of oxygen is a 3D function. Since the flow is uniform, partial pressure of oxygen is unlikely to get affected in the span-wise direction. The gradient in partial pressure along the height produces oxygen flux. To simplify the analysis, the partial pressure is averaged over the height and is used to compute oxygen uptake. Hence, the partial pressure can be assumed to vary in the stream-wise direction only.

5. Variation of solubility and diffusivity of blood with partial pressure has little effect on the oxygen uptake.

   Effective solubility and effective diffusivity are used [74]. *These values are obtained by averaging the solubility and the diffusivity over a range of partial pressure of oxygen blood is likely to develop in the device. The averaging is done to simplify the analysis.*

6. The geometry can be simplified by removing the pillars for the simulation (see figure 5.3 for illustration).

   As stated earlier, the flow has been assumed to be uniformly distributed. Since the blood flow in individual stream is the same, the streams will oxygenate at the same rate. As a result, multiple branches can be combined into a single equivalent one for analysis. Similarly, pressure drop of a rectangular stream is the function of its height, aspect ratio, length, and flow rate. Since an individual stream has the same blood flow, and geometric parameters, the pressure drop will be also the same. As a result, the streams can be combined into a single equivalent one for simulating

pressure drop. Hence, the reduced geometry works for both the models to calculate oxygen uptake and pressure drop.

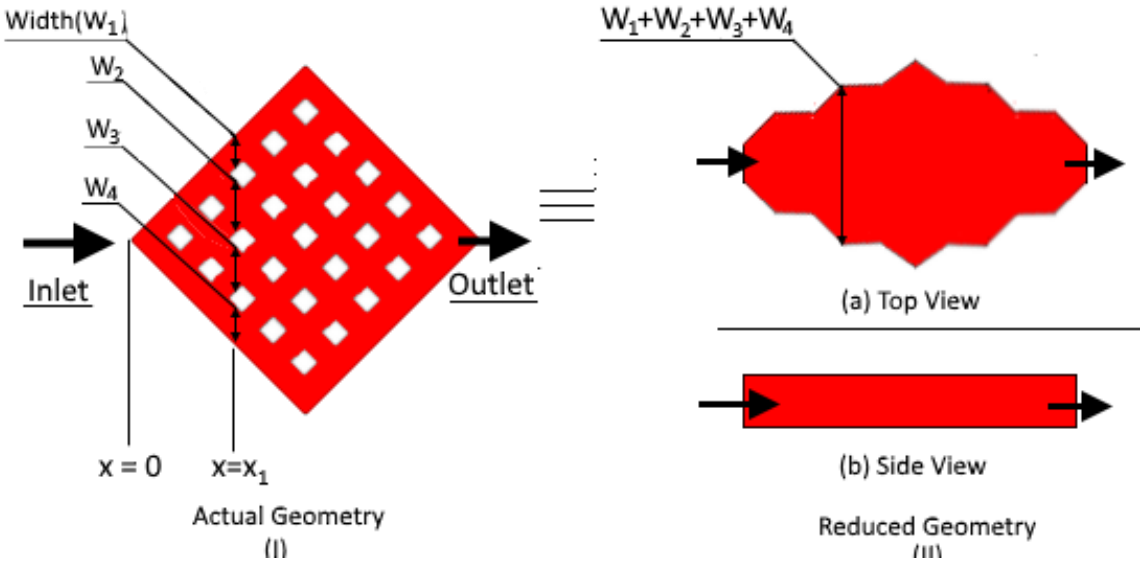

Figure 5.3 Process of the simplification of the geometry is illustrated. (I) Actual geometry is shown. (II) The pillars are removed to reduce the geometry to a simpler form.

Various boundary conditions have been applied for the simulation based on the assumptions above. To calculate oxygen saturation, the properties of the blood such as temperature, partial pressure of oxygen and carbon dioxide, and pH are fixed at the inlet and are given as input to the simulation. The properties of the input blood depend on the simulation; their values are prescribed later as the model is validated. Also, the partial pressure at the interface of the external gas and the membrane is equal to the partial pressure of oxygen in the external gas. To calculate pressure drop, the pressure at the outlet of the device is equal to zero. The flow rate is fixed and given as input to the simulation. To calculate membrane expansion at any location, the applied pressure is given by the hydraulic pressure at that location. Also, condition of no deflection on the

walls is applied. The boundary conditions will be expressed mathematically when the solvers for various model are explained.

In the next few sections, the governing equations explained in this section will be used along with the assumptions to model various parts of the oxygenator.

5.3 Oxygen Uptake

5.3.1 Model

As per the assumptions stated previously, there is no variation in pressure, flow rate and oxygen saturation in the span wise directions. Hence, the actual geometry with pillars can be simplified to a channel with varying rectangular cross section by removing the pillars in the actual geometry (figure 5.3). The width at any cross section of simplified geometry is the sum of the width of all channels in the cross-section of the actual geometry at the same stream-wise location.

The model uses an explicit technique to calculate the oxygen saturation at the outlet of the device. The domain is divided into small elements in the stream-wise direction as shown in figure 5.4. The simulation begins at the element at the inlet of the device. It uses the given oxygen saturation of the blood at the inlet and step-by-step calculates the oxygen saturation of the blood in the elements downstream.

At each step, the oxygen diffusing through the respective element is calculated using Fick's law. Based on the amount of oxygen diffusing in, the blood oxygen saturation and partial pressure are updated in the following element. The code continues till the blood properties at the outlet of the device are calculated.

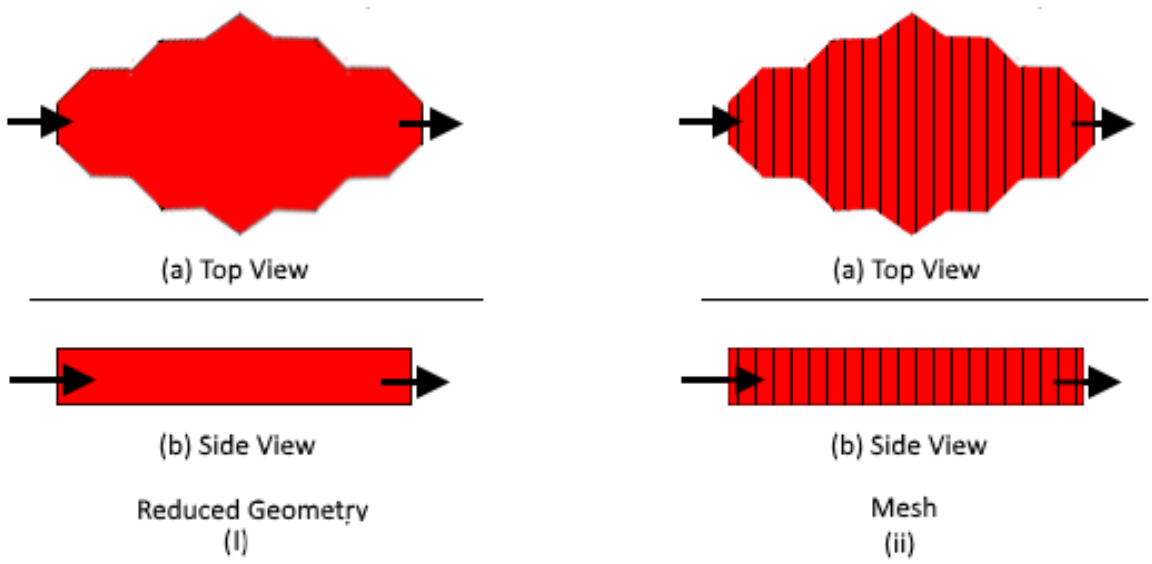

Figure 5.4 Process of meshing is demonstrated

The domain is first divided into smaller elements. Fick's law of diffusion is applied to these individual elements and it is used to calculate the oxygen diffusion. Membrane and blood plasma are regarded as layers providing resistance to the flow of oxygen. Based on the oxygen uptake, change in oxygen saturation and partial pressure of oxygen are calculated.

The flux of any gas(J_G) through a membrane of permeability ($\wp_m$) and thickness (t_m) is given by Fick's law as follows:

$$J_G = \wp_m \frac{\Delta P_G}{t_m} \tag{5.3.1}$$

Here ΔP_g is the difference in partial pressure of the gas 'G' on the either sides of the membrane.

In the case of an oxygenator, two such permeable layers exist in series; they are gas permeable membrane made out of silicone and blood layer. The permeability of the blood

layer is the product of its solubility and its diffusivity. As previously mentioned, the effective thickness of the blood for oxygen diffusion is equal to the boundary layer thickness, which is assumed to be half the channel height. The oxygen flux is then given by the following equation:

$$J_{O_2} = \wp_{eq} \frac{\Delta P_{O_2}}{h/2 + t_m} \tag{5.3.2}$$

Here, $\wp_{eq,}$ $\Delta P_{O_2,}$ h and t_m are the equivalent permeability of membrane and blood layer, difference in partial pressure, channel height, and membrane thickness.

Since the gas diffuses through the membrane and the blood in series, the equivalent permeability will be the harmonic mean of the ratio of the permeability and the thickness of both the membrane and the blood layer, multiplied by the sum of their thicknesses. The equivalent permeability will be given by the following equation:

$$\wp_{eq} = (h/2 + t_m) * \left(\frac{1}{\frac{1}{\wp_m / t_m} + \frac{1}{(S_b * D_b)/(h/2)}} \right) \tag{5.3.3}$$

Here $\wp_m, S_b$ and D_b are the permeability of the membrane, effective solubility, and effective diffusivity of blood. Substituting expression of equivalent permeability from equation (5.3.3) in (5.3.2), following expression for the oxygen flux is obtained:

$$J_{O_2} = \wp_m * S_b * D_b \frac{P_{O_{2,e}} - P_{O_2}(x)}{t_m * S_b * D_b + h/2 * \wp_m} \tag{5.3.4}$$

Here, $P_{O_{2,e}}$and $P_{O_2}(x)$ are the partial pressure of oxygen in the external gas and the partial pressure of oxygen in blood at the stream-wise location 'x'.

As mentioned before, solubility and diffusivity of the blood depends on the partial pressure of oxygen and other factors. However, as shown by Potkay [74], using effective solubility and effective diffusivity accurately predicts the oxygen uptake. Similarly in this study, their effective values are used. They are defined as the averaged value over a range of pressures likely to be experienced by the blood. Effective solubility and effective diffusivity are defined as follows:

$$\mathrm{S_b} = \frac{\int_{\mathrm{pO_{2,L}}}^{\mathrm{pO_{2,H}}} \mathrm{S_{O_2}}\,\mathrm{dpO_2}}{\mathrm{pO_{2,H}} - \mathrm{pO_{2,L}}} \tag{5.3.5}$$

$$\mathrm{D_b} = \frac{\int_{\mathrm{pO_{2,L}}}^{\mathrm{pO_{2,H}}} \mathrm{D_{O_2}}\,\mathrm{dpO_2}}{\mathrm{pO_{2,H}} - \mathrm{pO_{2,L}}} \tag{5.3.6}$$

Where, $pO_{2,H}$ and $pO_{2,L}$ are the highest and the lowest partial pressure of the blood in the device. S_{O_2} and D_{O_2} are solubility and diffusivity defined at the specific pO_2. Vaslef *et al* [75] defined the diffusivity at a specific dpO_2 by the following equation:

$$\mathrm{D_{O_2}} = \frac{\mathrm{D_{PL,O_2}}}{1 + \mathrm{c_T}\lambda_{\mathrm{O_2}}/\mathrm{S_{PL,O_2}}} \tag{5.3.7}$$

Here D_{PL,O_2} and S_{PL,O_2} are the diffusivity of oxygen in blood plasma (1.8×10^{-5} cm^2/s) [74] and the solubility of oxygen in blood plasma (3 x 10^{-5} ml O_2/ml blood/mmHg) [74]. Similarly, Hewitt *et al* [76] defined effective solubility at a specific dpO_2 by the following equation:

$$\mathrm{S_{O_2}} = \mathrm{S_{PL,O_2}} + \mathrm{c_T}\lambda_{\mathrm{O_2}} \tag{5.3.8}$$

$\lambda_{O_2}$is the slope of oxy-hemoglobin equilibrium curve (dsO_2/dpO_2) depends on the partial pressure of oxygen. c_T is the oxygen binding capacity of the blood. It is

proportional to the concentration of hemoglobin(ch_b) and is given by the following equation [76]:

$$c_T = 1.34 * ch_b \tag{5.3.9}$$

Now, the total amount of oxygen flowing inside the device through any infinitesimal element at stream-wise location 'x' is the product of the flux at that point and the area in contact with the oxygen. The area in contact is the product of the width and the length of the element. Since, the device is sliced along span-wise planes, the area in contact will be given by the following equation:

$$Contact\ Area = w(x) * \Delta x \tag{5.3.10}$$

Here w(x) and Δx are the width and the length of an infinitesimal element at a stream-wise location x. Hence, the resulting expression for the total amount of oxygen flow through such an element will be as follows:

$$\Delta Q_{O_2} = \wp_m * S_b * D_b \frac{P_{O_{2,e}} - P_{O_2}(x)}{t_m * S_b * D_b + h/2 * \wp_m} * w * \Delta x \tag{5.3.11}$$

Here, w is the total width of the element.

The amount of oxygen flowing through an element can also be found by the product of change in concentration of oxygen per ml of blood in an element, volume of the blood in the element, and inverse of the time taken by the volume of the blood to pass through the element. Following equation is obtained:

$$oxygen\ flow\ rate = \frac{change\ in\ concentration * volume\ of\ blood}{time} \tag{5.3.12}$$

The equation can be restructured as follows:

$$oxygen\ flow\ rate = \frac{change\ in\ Concentration * volume\ of\ blood}{volume\ of\ blood/blood\ flow\ rate} \quad (5.3.13)$$

Hence, the equation reduces to the following:

$$oxygen\ flow\ rate = blood\ flow\ rate\ * change\ in\ Concentration \quad (5.3.14)$$

As previously mentioned, the concentration of oxygen in blood (ml/ml) at a given oxygen saturation and partial pressure of oxygen is given by the following equation:

$$\mathrm{cO_2} = 1.34 * ch_b * \mathrm{sO_2} + 0.000031 * \mathrm{pO_2} \quad (5.3.15)$$

Here, $hct, sO_2,$ and pO_2 are blood hematocrit, oxygen saturation, and the partial pressure of oxygen respectively. The change in concentration of oxygen across any element can be written down in terms of oxygen saturation and partial pressure as follows:

$$\Delta\mathrm{cO_2} = 1.39 * ch_b * \Delta\mathrm{sO_2} + 0.000031 * \Delta\mathrm{pO_2} \quad (5.3.26)$$

Substituting the expression for ΔcO_2 from equation (5.3.16) in equation (5.3.14), we get:

$$\Delta\mathrm{Q_{O_2}} = \mathrm{Q_b} * (1.39 * ch_b * \Delta\mathrm{sO_2} + 0.000031 * \Delta\mathrm{pO_2}) \quad (5.3.37)$$

Rearranging equation 5.3.17, the change in the partial pressure of oxygen can be expressed as:

$$\Delta\mathrm{pO_2} = \frac{\Delta\mathrm{Q_{O_2}}}{\mathrm{Q_b} * \left(1.39 * ch_b * \frac{\Delta\mathrm{sO_2}}{\Delta\mathrm{pO_2}} + 0.000031\right)} \quad (5.3.48)$$

Similarly, the change in oxygen saturation can be expressed as

$$\Delta sO_2 = \frac{\Delta Q_{O_2}}{Q_b * \left(1.39 * ch_b + 0.000031 * \frac{\Delta pO_2}{\Delta sO_2}\right)} \tag{5.3.59}$$

The equations 5.3.18 and 5.3.19 will give the increase in the partial pressure of oxygen and the oxygen saturation, when the oxygen is flowing at Q_{O_2}inside an element of volume $w * h * \Delta x$ through which the blood is flowing at Q_b.

To find $\frac{\Delta pO_2}{\Delta sO_2}$ and $\frac{\Delta sO_2}{\Delta pO_2}$, a separate code was built to calculate the relationship between the oxygen saturation and the partial pressure of oxygen. The methodology is adapted from Dash *et al* [77]. A number of biochemical reactions are assumed to be happening inside red blood cells. Based on the equilibrium constants and rate constants for each of these reactions, an equation relating oxygen saturation and partial pressure of oxygen is built. As previously mentioned, the equation describing relationship between oxygen saturation and partial pressure of oxygen is assumed to be similar to Hill's equation, which is given by the following expression:

$$sO_2 \approx \frac{K_{HbO_2}[O_2]}{1 + K_{HbO_2}[O_2]} \tag{5.3.20}$$

Here K_{HbO_2} is a variable that depends on the partial pressures of oxygen and carbon dioxide, temperature, pH, and equilibrium constants for all the different reactions taking place in a red blood cell. The expression for K_{HbO_2} is given by the following expression [77]:

$$K_{HbO_2} = \frac{K_4'\left(K_3'[CO_2]\left\{1+\frac{K_3''}{[H^+]}\right\}+\left\{1+\frac{[H^+]}{K_6''}\right\}\right)}{\left(K_2'[CO_2]\left\{1+\frac{K_2''}{[H^+]}\right\}+\left\{1+\frac{[H^+]}{K_5''}\right\}\right)} \quad (5.3.21)$$

The equilibrium constants K_2'', K_3'', K_4'', K_5'', and K_6'' are 10^{-6} M, 10^{-6} M, 202123 M, 2.63 x 10^{-8} M, and 1.91 x 10^{-8} M. The equilibrium constants K_2' and K_3' are 29.5 M^{-1} and 25.1 M^{-1} respectively [77]. The expression for K_4' is given by the following equation [77]:

$$K_4' = K_4''\left\{\frac{[O_2]}{[O_2]_s}\right\}^{n_o}\left\{\frac{[H^+]}{[H^+]_s}\right\}^{-n_1}\left\{\frac{CO_2}{[CO_2]_s}\right\}^{-n_2}\left\{\frac{T}{T_s}\right\}^{-n_4} \quad (5.3.22)$$

Here, $[O_2]_s$, $[H^+]_s$, $[CO_2]_s$, and T_s are the concentrations and temperature at standard physiological conditions; their values are 146 µM, 57.5 nM, 1.31 mM, and 310 K respectively [77]. Here, n_o, n_1, n_2, and n_4 are exponents and their values are 1.7, 1.06, 0.12, and 4.65 respectively [77].

Please note that in equation 5.3.22, concentrations of oxygen and carbon dioxide are used instead of their partial pressure. The relationship between their concentration and partial pressure can be described by Henry's law. For any gas G, Henry law is given by the following equation:

$$[G] = \alpha_G * pG \quad (5.3.23)$$

α_G is Henry's constant and it varies with temperature. For oxygen and carbon dioxide, Dash *et al* [77] used a quadratic expression to represent the relationship between Henry's constant and temperature. The relationships are as follows:

$$\alpha_{O_2} = \frac{(1.37 - 0.0137 * (T - 37) + 0.00058 * (T - 37)^2) * 10^{-6}}{0.94} \quad (5.3.24)$$

$$\alpha_{CO_2} = (3.07 - 0.057 * (T - 37) + 0.002 * (T - 37)^2) * 10^{-6}/0.94 \quad (5.3.25)$$

Here, the temperature is in Kelvin.

For any given set of blood properties, corresponding OHEC can be found using equation (5.3.20). This OHEC can be used in calculating $\frac{\Delta pO_2}{\Delta sO_2}$ and $\frac{\Delta sO_2}{\Delta pO_2}$.

Since, sO_2 is a function of pO_2, T and $[H^+]$, the total derivative $\frac{\Delta sO_2}{\Delta pO_2}$ is be given by the following equation:

$$\frac{\Delta sO_2}{\Delta pO_2} = \frac{\partial sO_2}{\partial pO_2} + \frac{\partial sO_2}{\partial T}\frac{\Delta T}{\Delta pO_2} + \frac{\partial sO_2}{\partial ([H^+])}\frac{\Delta ([H^+])}{\Delta pO_2} \quad (5.3.26)$$

Temperature and partial pressure are independent as increasing partial pressure of oxygen does not add or remove the energy to the blood that may change the temperature. Also, since the blood is buffered with sodium bicarbonate, its pH is unlikely to change with a change in partial pressure of oxygen. The equation will reduce to the following:

$$\frac{\Delta sO_2}{\Delta pO_2} = \frac{\partial sO_2}{\partial pO_2} \quad (5.3.27)$$

The derivative $\frac{\partial sO_2}{\partial pO_2}$ can be approximated as follows:

$$\frac{\partial sO_2}{\partial pO_2} = \frac{sO_2([pO_2 + 0.01, T, [H^+]]) - sO_2([pO_2, T, [H^+]])}{0.01} \quad (5.3.28)$$

An increase of 0.01 mmHg is used to approximate the derivative because the relationship between the oxygen saturation and the partial pressure of oxygen is going to be linear in any interval of size 0.01 mmHg

Using equation (5.3.30), the derivatives $\frac{\Delta sO_2}{\Delta pO_2}$ and $\frac{\Delta pO_2}{\Delta sO_2}$ at any stream-wise location 'x_1' can be written as follows:

$$\left(\frac{\Delta sO_2}{\Delta pO_2}\right)_{x=x_1} = \frac{sO_2([pO_2(x_1) + 0.01, T(x_1), [H^+](x_1)]) - sO_2(x_1)}{0.01} \tag{5.3.29}$$

$$\left(\frac{\Delta pO_2}{\Delta sO_2}\right)_{x=x_1} = \frac{1}{\left(\frac{\Delta sO_2}{\Delta pO_2}\right)_{x=x_1}} \tag{5.3.30}$$

Now that the derivative of oxygen saturation with respect to the partial pressure of oxygen can be calculated, the model can be used to solve the change in oxygen saturation of the blood from the inlet to the outlet of a device.

5.3.2 Solver

The section describes the solver for oxygen uptake.

The solver begins at x = 0 with given blood properties as follows:

$$[sO_2, pO_2, T, [H^+]]_{x=o} = \left[sO_{2,i}, pO_{2,i}, T_i, [H^+]_i\right] \tag{5.3.31}$$

Here subscript 'i' represents the properties of the blood at the inlet. Once the condition is applied, the flux through the first element at the inlet is calculated using equation (5.3.11). Then the oxygen flow through the first element is found using equation (5.3.11). Then $\frac{\Delta sO_2}{\Delta pO_2}$ and $\frac{\Delta pO_2}{\Delta sO_2}$ are found using equation (5.3.29) and (5.3.30). Then the oxygen flow

and the derivatives are plugged in to find the increase in the partial pressure of oxygen and the oxygen saturation using equation (5.3.19) and (5.3.20) respectively. Then, the partial pressure of oxygen and the oxygen saturation of the blood in the adjacent element can be found as follows:

$$sO_2(x + \Delta x) = sO_2(x) + \Delta sO_2 \tag{5.3.32}$$

$$pO_2(x + \Delta x) = pO_2(x) + \Delta pO_2 \tag{5.3.33}$$

The solver then runs in a loop incrementing 'x' by 'Δx' at each step and finding the partial pressure of oxygen and the oxygen saturation of the blood in the adjacent element using equation (5.3.33) and (5.3.32) at each step.

5.3.3 Validation

In this section, the model generated to calculate the oxygen saturation in the previous section is validated. The model is applied to the experimental results of open rectangular channel [1] and branched network of open rectangular channels [78] for validation. The experimental conditions and geometrical parameters used in those papers were entered into the model to obtain the simulated results. Later these results are compared with the experimental results from those papers.

5.3.3.1 Application to Lee's open rectangular blood channels [1]

Lee *et al* [1] used a microfluidic artificial lung with 15 um tall blood channel. The total capillary length and width for the channels are 3 mm and 46 mm respectively. The channels sit on top of a 130 um thick gas diffusion membrane. In this section, device is simulated using the model above and compared with the experimentally measured performance of the device.

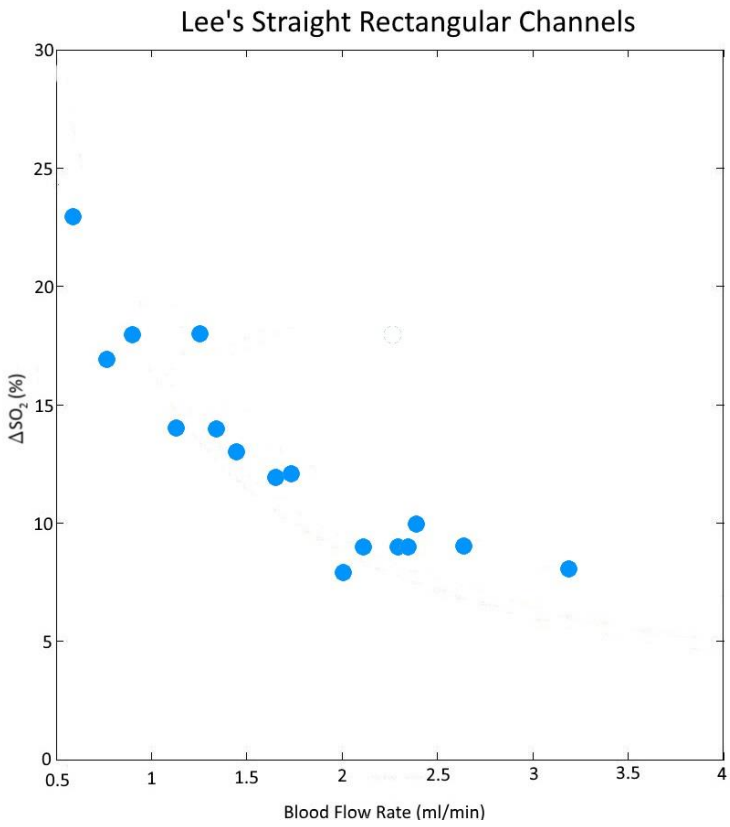

Figure 5.5 Variation of the change in oxygen saturation of the blood with the flow rate for Lee's device with straight rectangular channels [1].

The results of the experiments, taken from the paper, are shown in figure 5.5 as a variation of the change in oxygen saturation of the blood form the inlet to the outlet with the blood flow rate. As the flow rate is increased, the change in oxygen saturation decreases as the residence time decreases and the less amount of oxygen is taken up by the similar amount of blood.

Later, the device was simulated using the model developed and compared against the experimental results discussed above Bovine blood is used for experimentation with 70% blood oxygen saturation and 30% hematocrit. The solubility and diffusivity of the blood at the operating conditions is calculated to be 1.013×10^{-3} ml O_2/ml of blood/ mmHg and 1.02×10^{-6} cm^2/s respectively are used for the simulation based on the estimated range (35

– 80 mmHg) of oxygen partial pressures in blood in the experiment. The permeability of the gas membrane is taken as 6 x 10^{-9} ml O_2/s/cm^2/mmHg. Since pure oxygen was used to oxygenate the device, the partial pressure of the oxygen in the device exterior is input as 760 mmHg.

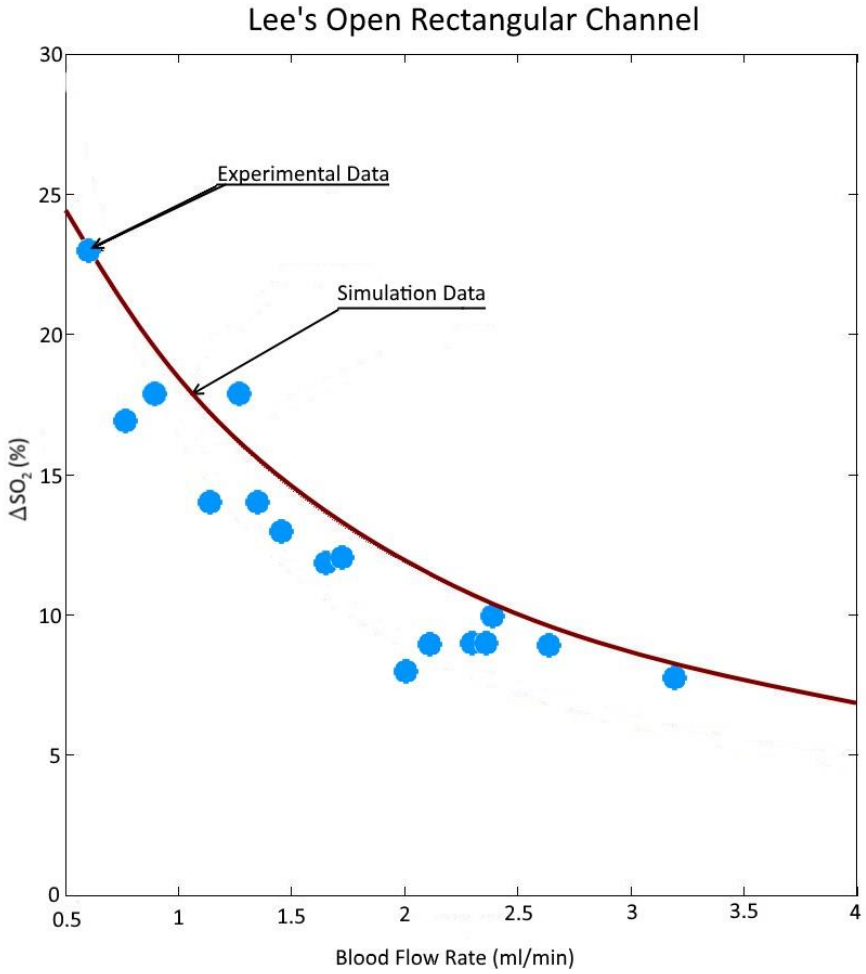

Figure 5.6 Validation of oxygen uptake model against the results of Lee et al [1]

The experimental data taken from the paper and the results of the simulation of the device using the model explained previously are plotted in figure 5.6 as points and line respectively. The change in oxygen saturation of the blood as it passes through the lung is taken as the performance indicating parameter and it is plotted as a function of flow rate.

As the flow rate increases, the change in oxygen saturation decreases for both the experiment and the simulation. This is in accordance with expectations as increasing blood flow rate decreases the residence time for blood. Also, the oxygen flux is dependent on the diffusion coefficient and thickness of the membrane and the plasma layer, and the oxygen partial pressure gradient. The diffusion coefficients and the thicknesses remain unchanged while the partial pressure gradient changes slightly with increased flow rate. Hence, the oxygen flow changes slightly with the blood flow rate while the blood residence time decreases greatly. As a result, the oxygen uptake by a blood cell decreases. Also, the results from simulation closely agree with the experimental results.

5.3.3.2 Application to the Branched Network of Open Rectangular Channels [78]

Later the artificial lung experimented by [78] is simulated and validated against. Individual channel in this case is 20 um tall, 88 um wide, and 750 um long. There are estimated 4400 such channels in bundle. The channels sit on top of a 15 um thick gas permeable membrane. Potkay [78] introduced square pillars in the device to provide stability to the membrane. This reduces the gas exchange area by 20%.

Results of the experimentation, taken from the paper, are presented in figure 5.7 as the variation of the total oxygen uptake by the device with the blood flow rate. As the blood flow rate increases, total oxygen uptake increases. It has already been established that increased flow rate implies lowered residence time, which in turn implies lowered change in oxygen saturation. Also, smaller change in oxygen saturation implies smaller change in partial pressure of oxygen in blood. Referring to equation 5.3.11 the amount of oxygen flowing in is directly proportion to the gradient in partial pressure of oxygen across the

gas permeable membrane. Lowered change in partial pressure of oxygen in blood implies higher partial pressure gradients across the gas permeable membrane, which in turn implies higher amount of oxygen flowing in. Later simulation was done using the model developed above. Bovine blood with oxygen saturation and hematocrit of70% and 34% respectively was used. The solubility and diffusivity of the blood at the operating conditions is calculated to be 9.63 x 10^{-4} ml O_2/ml of blood/ mmHg and 1.24 x 10^{-6} cm^2/s respectively. The permeability of the gas membrane is taken as 6 x 10^{-9} ml $O_2/s/cm^2/mmHg$.

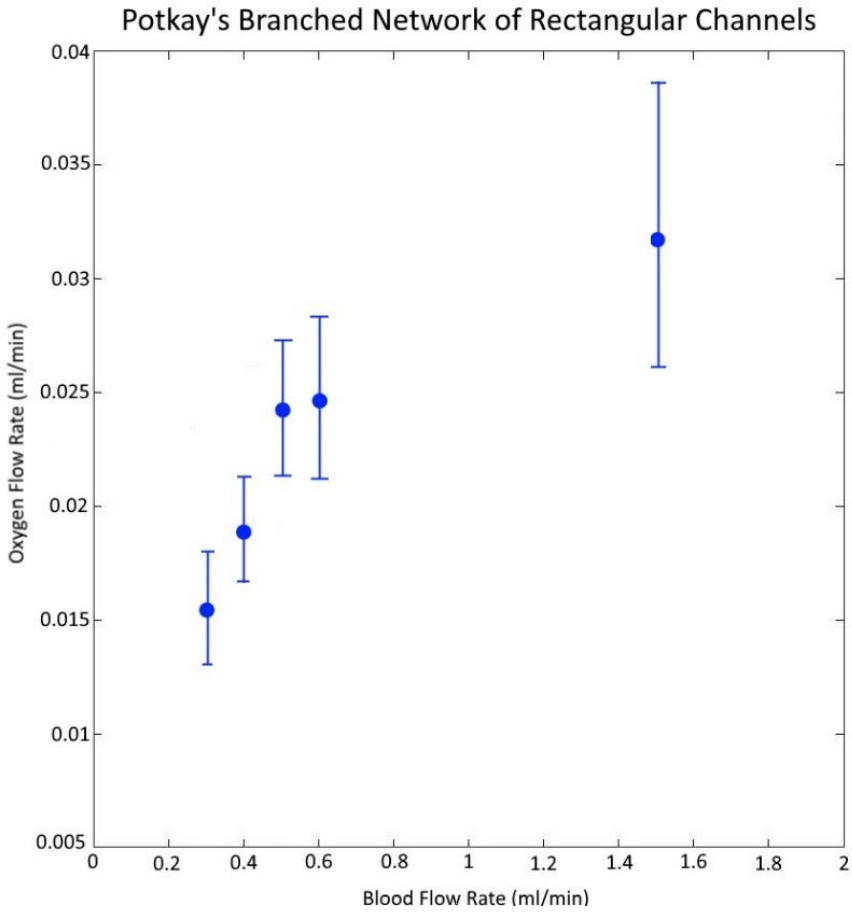

Figure 5.7 Variation of total oxygen uptake with the blood flow rate for Potkay's branched network of rectangular channels [78].

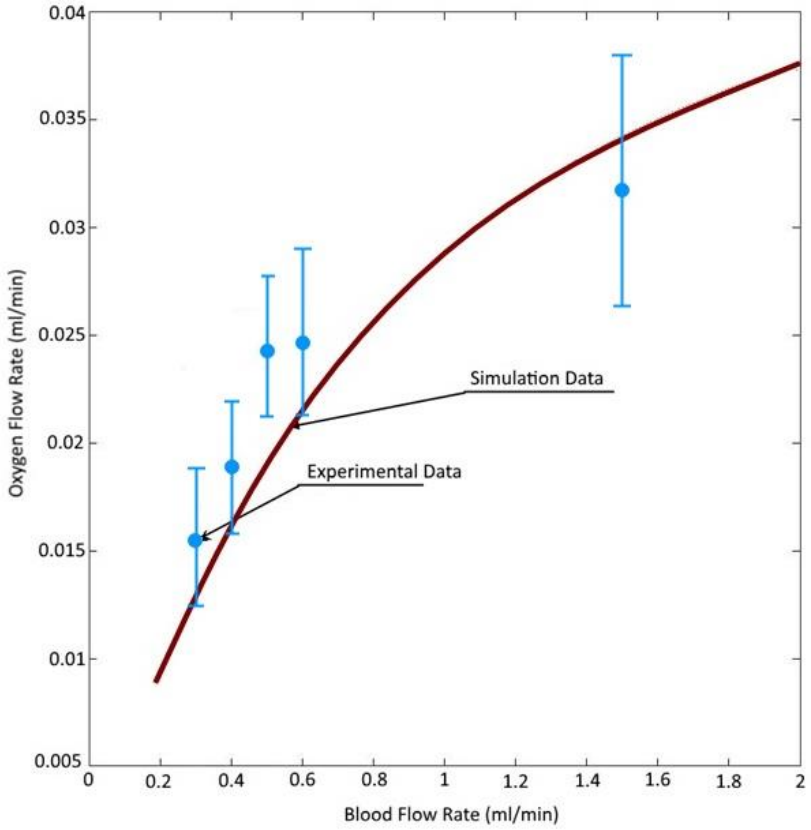

Figure 5.8 Validation of the oxygen uptake model against the experimental results of Potkay et al [78]

The experimental results and its corresponding simulation results are plotted in figure 5.8. In the plot, the amount of oxygen flowing in the device increases with increasing flow rate. The simulation results follow the same trend as the experimental results, but underestimate the oxygenation capacity of the device. As the simulation only takes the smallest capillaries into account and ignore the distribution network that leads to the capillaries. As a result, the oxygenation done in the distribution network is accounted and the simulation underestimates the oxygenation capacity, but closely follow the experimental results.

5.4 Pressure Drop

Instead of calculating the minute details of flow to calculate pressure drop, an alternate approach is employed. The calculation of overall pressure drop is done by simulating the different parts of the oxygenator, calculating the pressure drop across these parts, and subsequently adding them to get the total pressure drop. The parts are categorized based on the nature of fluid path in it. There are three such parts identified in a flat design. Such parts are inlet and outlet, and micro vascular network. At the inlet and the outlet, the fluid takes a sharp 90 degree turn as it enters or exits the device, while in the vascular network the fluid path is smooth. Different strategies are need to calculate the pressure drop across them.

The approach to calculate pressure drop in vascular network follows slicing the geometry into infinitesimal elements. Each of these elements can be assumed to be rectangular channels. Their hydraulic resistance can be calculated using standard expression. If the entry and exit effects of flow on these elements are small enough and the flow remains fully developed through out, then the total pressure drop across the whole device will be the sum of the pressure drop across the individual element.

5.4.1 Pressure Distribution in Micro Vascular Network

For a straight rectangular channel of length l, width w, and height h; the hydraulic resistance is given by the following expression [71]:

$$R_h \approx \frac{12\mu l}{wh^3\left(1 - 0.63\frac{h}{w}\right)} \tag{5.4.1}$$

As mentioned previously in section 5.2, the channel width is very high as compared to the channel height. Hence, the expression can be simplified to the following:

$$R_h \approx \frac{12\mu l}{wh^3} \tag{5.4.2}$$

Note that the above expression will give a lower bound for the resistance and the actual resistance is likely to be higher.

As previously mentioned, since the channel width is high compared to the channel high, the geometry can be reduced the same way as it was to calculate oxygen saturation. The procedure has been shown in figure 5.3. As a result, the hydraulic resistance of an element at location 'x' will be given by the following expression:

$$R_h(\mathrm{x}) \approx \frac{12 * \mu * \Delta x}{w(x) * h(x)^3} \tag{5.4.3}$$

Here, $w(x)$ is the width of an element in a reduced geometry.

Since all the elements are in series, the total hydraulic resistance of the microvascular network will be given by the following expression:

$$R_h = \int \frac{12\mu \Delta x}{w(x)h(x)^3} \tag{5.4.4}$$

As previously mentioned in section 5.1, Carreau model [72] for blood viscosity is used and it is given by the following expression:

$$\mu = \mu_\infty + (\mu_0 - \mu_\infty)[\,1 + (\lambda\dot{\gamma})^2]^{\frac{n-1}{2}} \tag{5.4.5}$$

Here, $\dot{\gamma}$ is the shear rate. $\mu_\infty = 0.0035$ and $\mu_0 = 0.056$ Pa-s are viscosities of blood at infinite and zero shear rate respectively. Also, λ = 3.133 s and n = 0.3568 are constants.

The shear rate is approximated as the ratio of average velocity and height of the channel. The average velocity can in turn be written in terms of the flow rate and the cross section area. The resulting expression for the shear rate will be given by the following equation:

$$\dot{\gamma} = \frac{Q_b}{w(x)h(x)^2} \tag{5.4.6}$$

Substituting the expression for shear rate (equation (5.4.6)) and the expression for viscosity (equation (5.4.5)) into the expression for hydraulic resistance (equation (5.4.4)), following expression is obtained:

$$R_h = \int \frac{12(\mu_\infty + (\mu_0 - \mu_\infty)\left[1 + \left(\frac{\lambda Q_b}{w(x)h(x)^2}\right)^2\right]^{\frac{n-1}{2}})\Delta x}{w(x)h(x)^3} \tag{5.4.7}$$

5.4.2 Pressure Drop at the Inlet and the Outlet

The pressure drop at the inlet and the outlet will require solving complex set of equations, which will be computationally intensive and will slow down the simulation if the equations are solved along with the existing. Hence, an empirical approach is taken to predict the pressure drop at the inlet and the outlet and a relationship between the characteristic dimensions of the geometry, the flow rate, and the pressure drop is built. The geometry shown in figure 5.9 is simulated in COMSOL for a range of flow rates and heights. The geometry includes the inlet tubing and a part of the micro vascular network. The relationship is assumed to be of the following form:

$$\Delta P = a_1 Q^{a_2} h^{a_3} \tag{5.4.8}$$

Here a_1, a_2 and a_3 are constants. Their value is found using regression analysis. Also, pressure drop, flow rate, and height are in mmHg, m^3/s, and m.

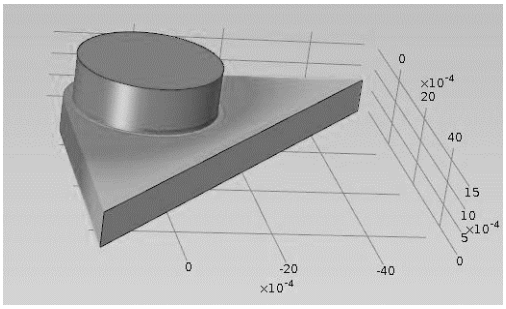

Figure 5.9 Illustration of the geometry used to simulate pressure drop at the inlet

The simulation models blood flow as incompressible, laminar, steady and non-Newtonian flow. Carreau model is used to simulate non-Newtonian behavior of the blood. Tetrahedral mesh elements are used to mesh the geometry. The pressure drop increases non-linearly as flow rate increases and as height decreases. The constants a_1, a_2 and a_3 are 0.0576, 0.946 and -2.717. Hence, the resulting equation is as follows:

$$\Delta P = 0.0576 * Q^{0.946} h^{-2.717} \tag{5.4.9}$$

5.4.3 Validation

In this section, the model developed in the previous section is validated. For validation, pressure drop across an oxygenator with flat design is measured for different flow rates. The oxygenator is fabricated with a very thick membrane (>1mm) so that the membrane expansion is virtually zero. Details of the experimental set up and the procedure have been presented in chapter 6.

The results are plotted in the figure 5.10. There is a linear and positive correlation between flow rate and pressure drop. This is in accordance with the theory as hydraulic channels are analogs to electrical elements. If the resistance is kept constant, the increase in pressure drop is proportional to the increase in flow rate. As can be seen from the graph, the results obtained from simulation closely agree with the experimental results.

The deviation increases as the flow rate is increased. This is likely the effect observed as a result of the flexible nature of the membrane. Even though the membrane is thick, it will expand under high pressure. As a result, the deviation is higher at high flow rates.

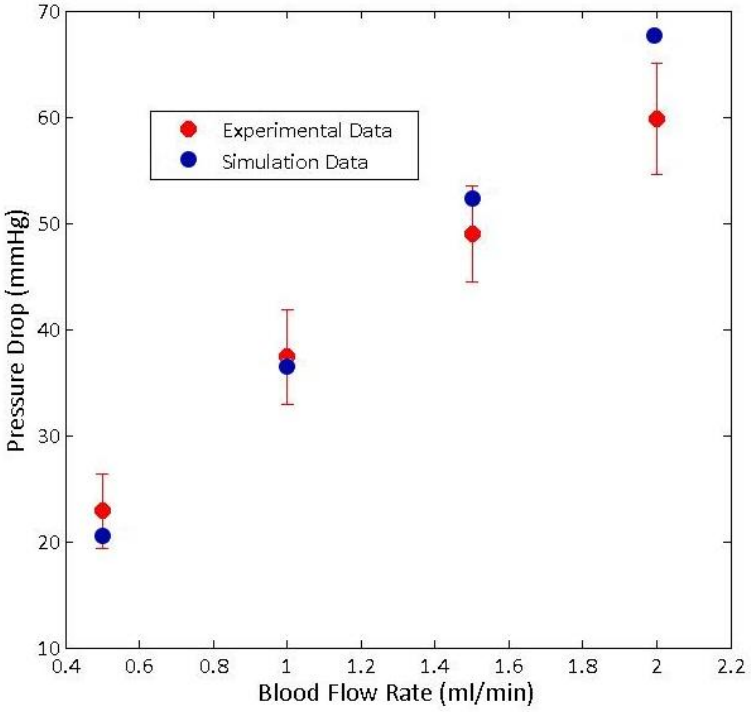

Figure 5.10 Validation of pressure drop model against experimental results

5.5 Membrane Expansion

5.5.1 Model

PDMS membrane is used as the interface for gas exchange between the blood and the atmosphere. PDMS is mechanically flexible and it deforms under pressure. In an operating oxygenator, the pressure on inside of the device is higher than the pressure outside. This disparity in pressure across the membrane causes it deform, which changes the geometry of the device. The change in geometry in turn causes the pressure drop and

the oxygen uptake to change. To accurately predict the oxygen uptake and the pressure drop, the membrane expansion of the membrane in our device must be calculated.

Modeling membrane expansion proves challenging owing to the intricate shape of its boundary. In a flowing medium, other factors such as non-uniform distribution of pressure and two way coupling between pressure drop and membrane deformation causes even more complications. A simpler model is chosen to minimize the computational cost. The model is illustrated in figure 5.11. At any cross section, the membrane deformation is modeled as a fixed membrane under uniform pressure. The pressure value came from the calculated pressure at the cross section from the model. The membrane deformation was assumed circular as it the simplest model possible. The model was validated by comparing the simulation results with the experimentally measured deflection of the membrane. When at rest the diameter of the membrane is equal to the pillar spacing.

The expression for the deflection of a circular membrane under uniform pressure [73] is given by the following expression:

$$W(r) = W_o\left(1 - \frac{r^2}{R^2}\right) \tag{5.5.1}$$

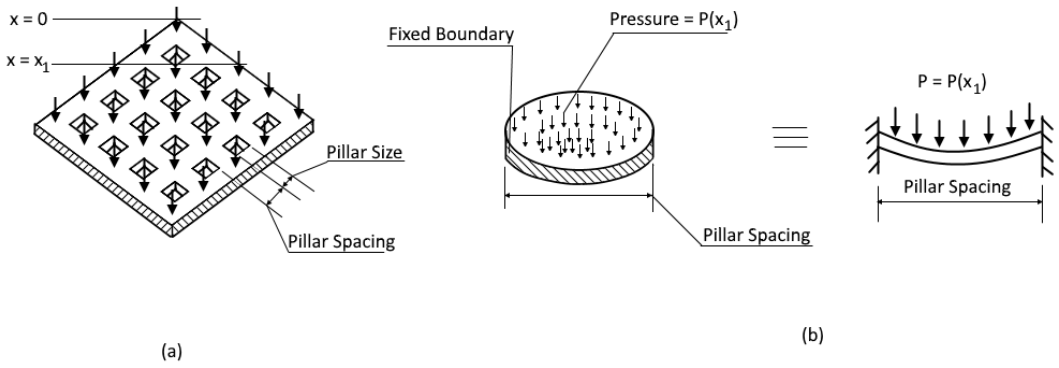

Figure 5.11 Process of calculating membrane expansion is illustrated. At any location x_1, the membrane expansion is calculated by assuming a circular membrane

Here, W_o, r, R and $W(r)$ are the maximum deflection, radial distance from the center, radius of the membrane, and deflection at a radial distance r from the center.

Force balance on the membrane results into the following equation:

$$2\sigma_M \sin\alpha = \Delta P * \mathrm{D} \tag{5.5.2}$$

Here σ_M is the shear stress in the membrane. α is the angle representing the slope of the membrane at the boundary. The angle is with the horizontal axis. Also, ΔP is the difference between the pressures applied on either sides.

$$\sin\alpha = \frac{tan\alpha}{sec\alpha} = \frac{tan\alpha}{\sqrt{sec^2\alpha}} = \frac{tan\alpha}{\sqrt{1+tan^2\alpha}} = \frac{\frac{dW}{dr}_{r=\mathrm{R}}}{\sqrt{1+\left(\frac{dW}{dr}_{r=\mathrm{R}}\right)^2}} \tag{5.5.3}$$

The expression for $\frac{dW}{dr}$ can be found by differentiating the expression for $W(r)$ as given in equation (5.5.1).

$$\frac{dW}{dr} = \frac{-8W_o r}{D^2} \underset{r=\mathrm{R}}{\Longrightarrow} \frac{-4W_o}{D} \tag{5.5.4}$$

$$\sin\alpha = \frac{-4W_o}{\sqrt{D^2+W_o^2}} \tag{5.5.5}$$

Hooke's law is invoked to find the axial stress:

$$\in_r = \frac{\sigma_M}{E_r} + \vartheta\frac{\sigma_\theta}{E_\theta} \tag{5.5.6}$$

$$\in_\theta = \frac{\sigma_\theta}{E_\theta} + \vartheta\frac{\sigma_M}{E_r} \tag{5.5.7}$$

Here ϑ, E_θ, and E_r are the Poisson's ratio, Young's modulus in tangential and radial direction respectively.

Now, if tangential strain ($\in_\theta$) is assumed to be zero, then the following expression is obtained:

$$\sigma_M = \frac{\in_r E}{1-\vartheta^2} \tag{5.5.8}$$

From equations (5.5.2), (5.5.5) and (5.5.8), following expression for pressure difference across the membrane in terms of shear strain is derived:

$$\Delta P = -\frac{\in_r E * \sqrt{D^2 + W_o^2}}{8W_o * D * (1-\vartheta^2)} \tag{5.5.9}$$

$$\in_r = \frac{\Delta l}{D} = \frac{l_{ex} - D}{D} \tag{5.5.10}$$

$$l_{ex} = \int \sqrt{dW^2 + dr^2} \tag{5.5.11}$$

Here, l_{ex} and R are the length and diameter of the membrane under stress and at rest respectively.

$$l_{ex} = \int_{-l/2}^{l/2} \sqrt{1 + \left(\frac{dW}{dr}\right)^2}\, dr \tag{5.5.12}$$

$$l_{ex} = \int_{-l/2}^{l/2} \sqrt{1 + \left(\frac{r}{\left(\frac{D^2}{8W_o}\right)}\right)^2}\, dr \tag{5.5.13}$$

$$l_{ex} = \frac{4W_0}{D^2}\left[D\sqrt{\frac{D^2}{4}+\left(\frac{D^2}{8W_0}\right)^2}+\left(\frac{D^2}{8W_0}\right)^2 ln\left(\frac{\sqrt{\frac{D^2}{4}+\left(\frac{D^2}{8W_0}\right)^2}+\frac{D}{2}}{\sqrt{\frac{D^2}{4}+\left(\frac{D^2}{8W_0}\right)^2}-\frac{D}{2}}\right)\right] \quad (5.5.14)$$

5.5.2 Solver

In most cases, pressure is already known and deflection is meant to be calculated. Here expression for pressure in terms of maximum deflection is derived. The expression is non-linear involving natural logarithms and square roots. To calculate deflection for a given pressure, an iterative algorithm is used.

The code takes pressure, pillar size and structural properties of PDMS as input.

$$l = f(\Delta P, P_s, E, \vartheta) \quad (5.5.15)$$

Here, $\Delta P, P_s, E$ and ϑ are pressure drop, pillar size, Young's modulus of PDMS and Poission's ratio of PDMS.

An initial value for deflection is assumed as W_i:

$$W_o = W_i \quad (5.5.16)$$

Extension in length is calculated using the equation (5.5.14) as follows:

$$l_{ex} = \frac{4W_{\mathrm{i}}}{{P_s}^2}\left[P_s\sqrt{\frac{{P_s}^2}{4}+\left(\frac{{P_s}^2}{8W_{\mathrm{i}}}\right)^2}+\left(\frac{{P_s}^2}{8W_{\mathrm{i}}}\right)^2 ln\left(\frac{\sqrt{\frac{{P_s}^2}{4}+\left(\frac{{P_s}^2}{8W_0}\right)^2}+\frac{P_s}{2}}{\sqrt{\frac{{P_s}^2}{4}+\left(\frac{{P_s}^2}{8W_{\mathrm{i}}}\right)^2}-\frac{P_s}{2}}\right)\right] \quad (5.5.17)$$

Shear strain is found using equation (5.5.10) based on extension in the length of the membrane. Corresponding pressure is calculated using equation (5.5.9)

$$\Delta P_i = -\frac{\in_r E * \sqrt{D^2 + W_o^2}}{8W_o * D * (1 - \vartheta^2)} \tag{5.5.18}$$

The calculated pressure is compared with the input pressure and the difference is calculated as the error:

$$\text{error} = \Delta P - \Delta P_i \tag{5.5.19}$$

The error is used to update the assumed initial value of the deflection as follows:

$$\mathrm{W}_i = (1 - error) * W_i \tag{5.5.20}$$

Now the solver repeats the procedure from equation (5.5.15) to equation (5.5.20) till the error reaches $1*10^{-6}$.

5.5.3 Validation

Like other models developed in the earlier sections, it is essential to validate the model for the membrane deflection to extend its applicability to an oxygenation under operation. This section presents the validation of the model against the experimental results of the deflection of a PDMS membrane under static pressure.

Experimental setup explained in section 4.4.2 was set up to measure the maximum deflection of a membrane attached to a sloping profile oxygenator (section 4.2 of chapter 4) under different static pressure (10, 40, and 70 mmHg). The results were compared against the simulation. Young's modulus, Poisson's ratio, the thickness and the radius of the equivalent circular membrane were taken as 2.5 MPa [79], 0.5 [79], 50 µm, and 1 mm.

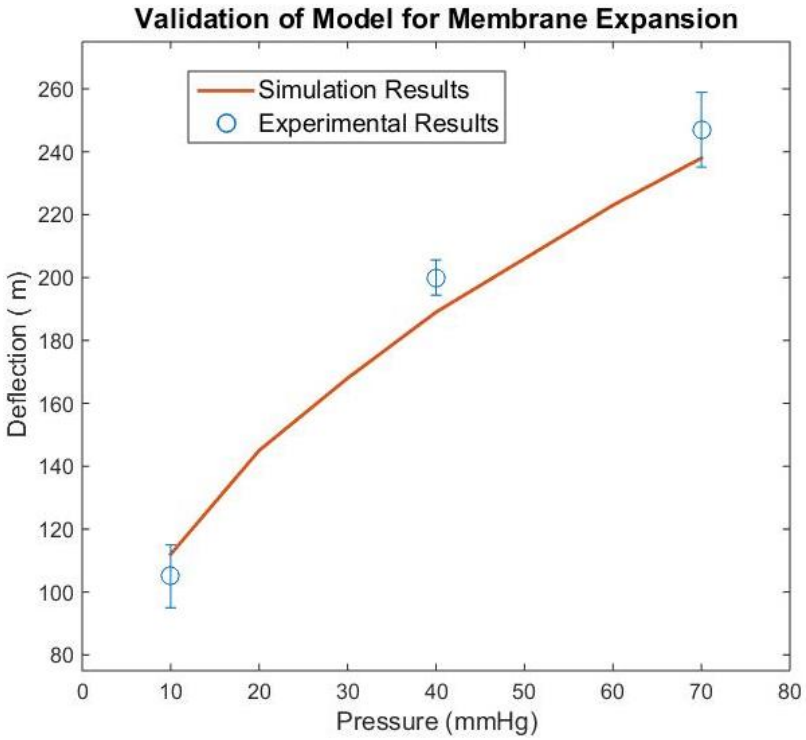

Figure 5.12 Validation of the model for membrane expansion. Maximum deflection is used to validate the results.

Figure 5.12 compares the experimental results with the simulation results for the membrane expansion. The deflection increases as the pressure drop is increased. This is in accordance with the expectations as increasing pressure will increase the stresses and larger deflection will be observed. Also, the simulation results closely agree with the experimental results, which validates the model.

5.6 Integrated Model

In the previous sections, separate parts of the model was validated with existing experimental data available in the literature. This section combines the individual parts into an integrated model to accurately predict the key performance indicators of oxygenators of our interest. Flat profile device with PDMS membrane as explained in section 4.2 of chapter 4 are modeled in this section. Experimentally measured

performance of flat design is used to validate the integrated model. 5 oxygenator units were tested using experimental procedure laid out in chapter 4. The oxygen saturation of the input blood was set at $55\% \mp 5\%$.

For the simulation, hematocrit, pH, pCO_2, pO_2, temperature, and sO_2 of the input blood were taken as 32%, 7.41, 29 mmHg, 30 mmHg, and 55%. The range of partial pressure of oxygen was 30 mmHg to 57 mmHg for which the effective solubility and the effective diffusivity were taken as 9.6×10^{-4} $mmHg^{-1}$ and 1.2×10^{-6} cm^2/s.

For experimentally measured performance, the oxygen saturation decreases as the blood flow increases for both the designs (figure 5.13). The results agree with the expectations. As increased flow rate indicates lowered residence time which in turn means the blood cells will spend lesser amount of time in the device to accept oxygen. The mathematical model also predicts similar behavior and agree within a maximum error of $\Delta sO_2 = \mp 10\%$. The difference between the experimental results and the simulation results is high at lower flow rates and low at higher flow rates. It is unlikely that the cause of deviation is the assumptions made in the oxygen uptake model, as it is previously seen in subsection 5.3.3 the model to calculate oxygen uptake predicts the experimental results with fair accuracy. The possible cause of deviation could be attributed to the model to calculate membrane expansion. It is likely that the model overestimates membrane expansion at low flow rates and hence the performance is underestimated as a result.

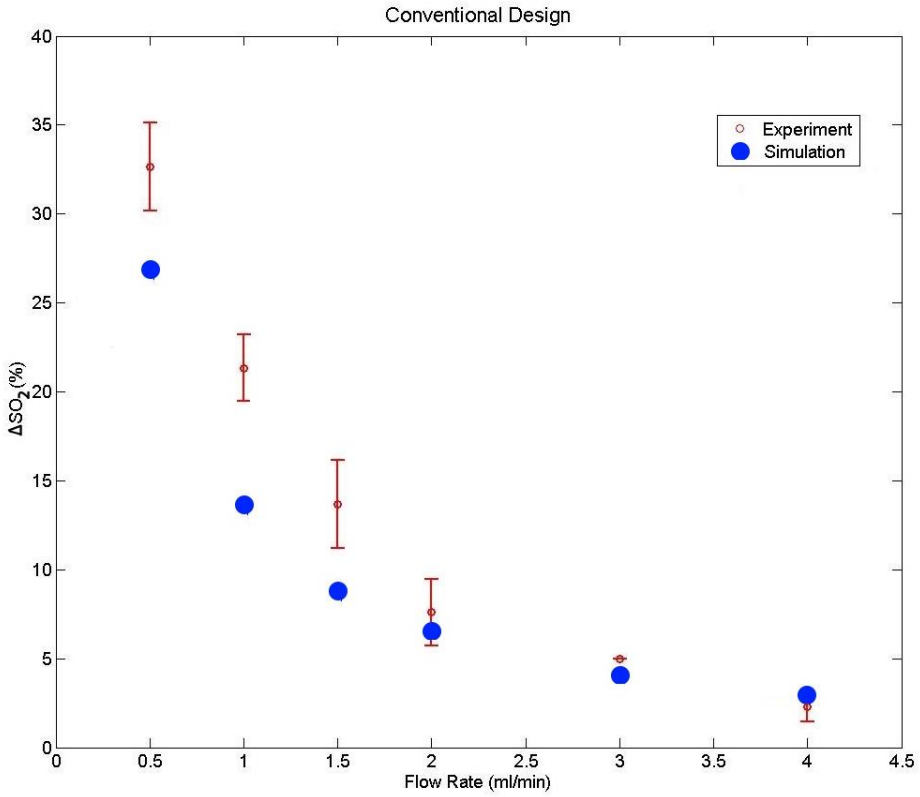

Figure 5.13 Variation of oxygen saturation with blood flow rate is plotted. In the plot, experimental results and mathematical predictions have been plotted.

The experimentally measured pressure drop increases as the blood flow increases (figure 5.14). The plot is non-linear in nature. The non-linearity of the plot is a result of the flexible nature of membrane. The membrane expands as a result of high pressure because of which the hydraulic resistance of the device is lowered and lower pressure drops are observed. Since the mathematical model incorporate membrane deflection, the pressure drops predicted by it agree with the experiment results within one standard deviation of the mean.

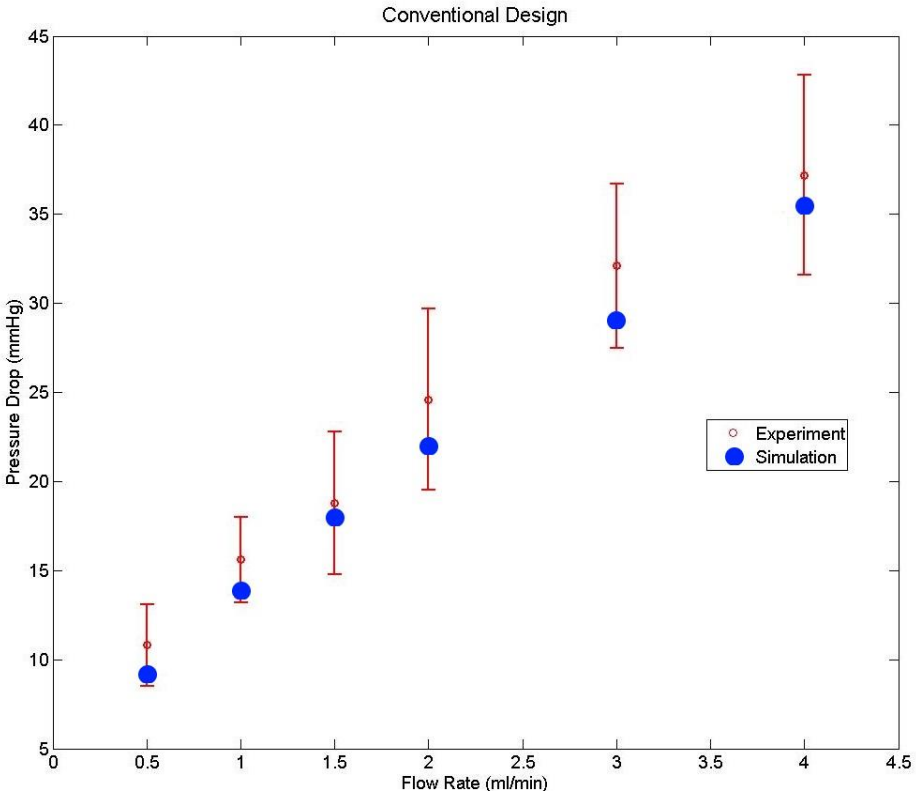

Figure 5.14 Variation of pressure drop with blood flow rate is plotted. In the plot, experimental results and mathematical predictions have been plotted.

In summary, the chapter presents the mathematical model to simulate oxygen uptake of the blood flowing in an oxygenator and the pressure drop generated across it. The model also calculates the membrane deflection at the operating pressure and update the geometry prior to calculating oxygen uptake. In order to develop the model, the models to calculate oxygen uptake, pressure drop, and membrane deflection are developed and validated separately and then integrated in a single model before validating.

Next chapter presents the results and the experimental testing of the devices explained in section 4.2 of chapter 4. In chapter 7, the model developed here will be used in doing a parametric analysis and optimization of those designs.

Chapter 6 – Experimental Results

This chapter presents results of experimental testing of various designs discussed in chapter 4. In particular, the flat and sloping cross sectional designs have been tested. Both designs were tested incorporating PDMS and composite membrane. First, results of burst pressure measurement are presented. Then, hydraulic resistance of devices was measured using water. Finally, oxygen uptake and hydraulic performance was characterized using blood.

6.1 Results & Discussion

6.1.1 Burst Pressure

Burst pressure for various devices was measured using the experimental setup described in section 4.4.1 of chapter 4. In particular, burst pressure was measured for (a) flat design with 500 µm wide pillars, (b) flat design with 1000 µm wide pillars, (c) sloping design with 170 µm maximum height and 60 µm minimum height, (d) flat design with composite membrane, and (e) sloping design with 170 µm maximum height and 60 µm minimum height and composite membrane with 10 devices tested for each design. Rest of the geometric parameters of all the designs were the same as mentioned in chapter 4. Also, PDMS membrane used for all devices unless otherwise specified.

The results for burst pressure for various designs are plotted along with their corresponding standard deviation in figure 6.1. The error associated with the pressure transducer is ±1 mmHg. The range of operating pressure normally encountered in actual operation is also indicated on the plot as a red stripped band. As it can be seen, the flat design with 500 µm

wide pillars had the lowest mean burst pressure at 68.5 mmHg with a standard deviation of 61.7 mmHg.

Flat design with 1000 µm wide pillars had a higher mean burst pressure of 145 mmHg with standard deviation of 51 mmHg. Increasing pillar size increased burst pressure as a result of increased contact area between individual pillar and the membrane. Hence, higher pressure needs to be applied to separate membrane from the pillars.

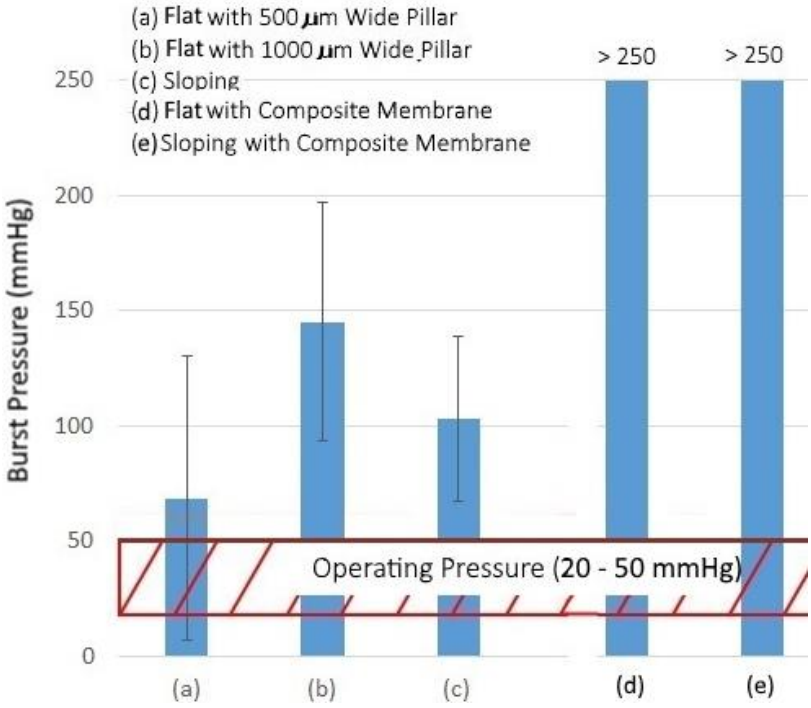

Figure 6.1 Burst pressure for various designs

Sloping devices had a mean burst pressure of 97.3 mmHg with a standard deviation of 29.7 mmHg, which is slightly lower than flat design with 1000 µm wide pillars. This reduction may be due to the different manufacturing processes used for sloping design and flat design. The mold for flat design was manufactured using photolithography, while sloping design was manufactured using micromilling. Photolithography gives smoother surfaces

as compared to micro-milling. Hence, bonding between membrane and pillars in sloping design was weaker as compared to flat design.

Composite membrane devices outperformed all other devices with none of the devices failing under the applied pressure ranging between 0 – 250 mmHg. The possible reasoning behind the superior performance of composite membrane as compared to PDMS membrane can be attributed to the high strength of composite membrane [80]. Figure 6.2 shows the cross-section of a part of the membrane attached to the pillars under pressure 'P'. A force acts on the membrane that separates it from the pillars. The PDMS membrane has a lower Young's modulus and undergoes large deflection under pressure. As a result, the separating force gets concentrated at the area near the periphery of the pillars. The composite membrane has high Young's modulus as it is reinforced with a steel mesh and hence it undergoes negligible deflection under pressure. As a result, the separating force gets uniformly distributed over the contact area between the membrane and the pillars. Since the area near the periphery of a pillar is small as compared to the whole contact area between the pillars and the membrane, the stresses separating the pillars and the membrane in case of composite membrane is low compared to the PDMS membrane under same applied pressure. Hence, the PDMS membrane has a low burst pressure as compared to the composite membrane.

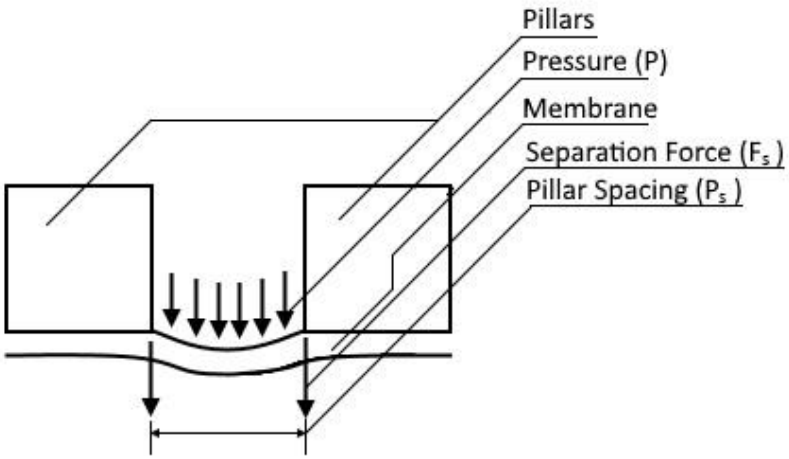

Figure 6.2 Figure illustrating membrane under pressure.

6.1.2 Hydraulic Resistance of the device to flow of Water

Hydraulic resistance of devices with water was measured using the experimental setup explained in chapter 4. The pressure drop was measured prior to performance characterization of devices with blood. This step was done to pick the devices with similar hydraulic resistance and to detect any potential device failure in the operating pressure range (20-50 mmHg).

Figure 6.3 shows variation of pressure drop across different devices for different flow rates of water. In particular, flat and sloping profile devices with PDMS membrane and composite membrane are plotted along with the simulation for flat and sloping devices with rigid membrane which does not undergo any deflection. The pressure drop increases with increasing flow rate for all designs as shown in Figure 6.3. This is in accordance with the expectations, as the pressure drop is the product of the hydraulic resistance of the device and the flow rate. Hence, as the flow rate is increased, the pressure drop will also increase.

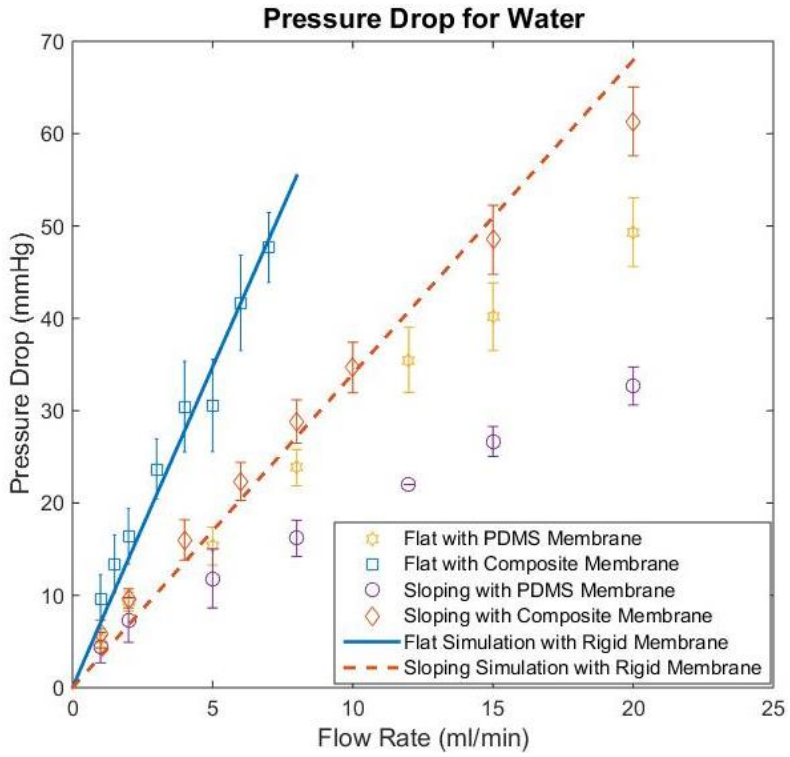

Figure 6.3 Pressure drop of various designs for water

Devices with composite membrane exhibit higher pressure drops as compared to the devices with PDMS membrane. This is in accordance with theory, as the composite membrane is stiffer as compared to PDMS membrane. As a result, composite membrane undergoes smaller deflection as compared to PDMS membrane under operation. Since hydraulic resistance inversely correlates with height, hydraulic resistance of devices with composite membrane will be higher as compared to devices with PDMS. Also, simulation results of flat and sloping devices closely match with the experimental results of devices with composite membrane at low flow rates and slightly deviate at high flow rates, indicating composite membrane undergoes negligible deflection under the operating pressures and flow rates.

6.1.3 Performance Characteristics of various configurations of oxygenator using Blood

In this section, performance for various designs have been characterized. In particular, results for flat design and sloping design with PDMS membrane and composite membrane have been reported. The designs have been discussed in detail in section 3.2 of chapter 4. The performance has been characterized by measuring pressure drop and change in oxygen saturation of blood for different flow rates. The experimental setup used to measure change in oxygen saturation and pressure drop has been explained in section 4.4.4 of chapter 4.

Experimental results and results of simulation have been plotted on the same graph. Pressure drop and change in oxygen saturation have been plotted for blood flow rates of 0.5, 1, 1.5, 2, 3, and 4 ml/min on the same graph. The experiment was repeated 5 times for each design. Bovine blood was used for the experiment as stated in section 4.4.4 of chapter 4 and the blood hematocrit ranged between 28% and 32%. The oxygen saturation, partial pressure of oxygen, partial pressure of carbon dioxide and pH of the input blood were in the range of 42 – 51%, 37 – 44 mmHg, 51 – 61 mmHg and 7.07 – 7.13 respectively. The effective solubility and effective diffusivity were taken as 1.03×10^{-3} $mmHg^{-1}$ and 1.33×10^{-6} cm^2/s for the partial pressure of oxygen ranging between 37 – 76 mmHg for the simulations.

6.1.3.1 Oxygenator with Flat Profile and PDMS Membrane

As mentioned earlier in chapter 2, the current study develops the configuration of flat profile by Wu *et al* [53]. Hence, initially the flat profile configuration was tested with

blood. The design is explained in chapter 4 along with the geometric parameters prescribed for the study.

Figure 6.4 presents the performance of the oxygenator of flat cross-sectional design at various flow rates. Change in oxygen saturation and blood flow rate at the mean operating pressure are used for comparative analysis. Here the operating pressure for the oxygenator was set at 30 mmHg which represents the mean expected arterio-venous pressure difference in a neonate. Since this is a driving source of the oxygenator and cannot be changed, its value is set constant and the oxygenator has to be designed in such a way that sufficient oxygenation of blood occurs in the design at sufficient flow rate to meet the needs of the neonate.

The change in oxygen saturation for flat design with PDMS membrane was 5% at a flow rate of 3 ml/min (figure 6.4) at 30 mmHg. In the case of flat design, the total oxygen uptake was calculated as 18.1 µL/min by using equation 5.4. The requirement for an oxygenating unit of an artificial placenta is to increase oxygen saturation by at least 35% while operating at the mean pressure to provide adequate respiratory support. Hence, this device configuration does not meet the requirement of an artificial placenta and will require additional development.

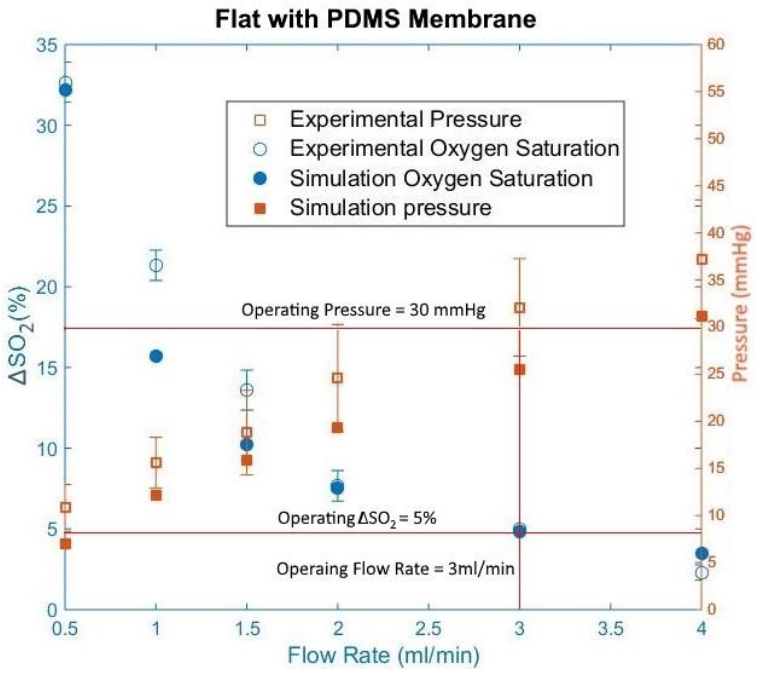

Figure 6.4 Variation of change in oxygen saturation and pressure drop with flow rate for flat device with PDMS membrane. The height of the channels and the width of the device are 100 µm and 43 mm at rest as previously explained in section 4.2 of chapter 4.

6.1.3.2 Oxygenator with Sloping Profile and PDMS Membrane

The cross-sectional area and gas exchange area per unit length of a flat device increases in the stream-wise direction from the inlet to the center of the device and decreases till the outlet of the device. Hence, the region close to the inlet and the outlet has lower contribution to the oxygen uptake and higher contribution to the pressure drop as compared to the region near and at the center of the device. As a result, a new design was conceived in which the flat height profile was redesigned to the sloping profile to improve oxygen uptake and reduce pressure drop. In a sloping height profile, the height of the device decreases linearly from the inlet to the center of the device and increases linearly from the center to the outlet of the device. Hence, the cross-sectional area in the region close to the inlet and the outlet is high. As a result, lower pressure drop would be

observed. Also, the channel height is low at the center of the device. Hence the oxygen uptake would also improve.

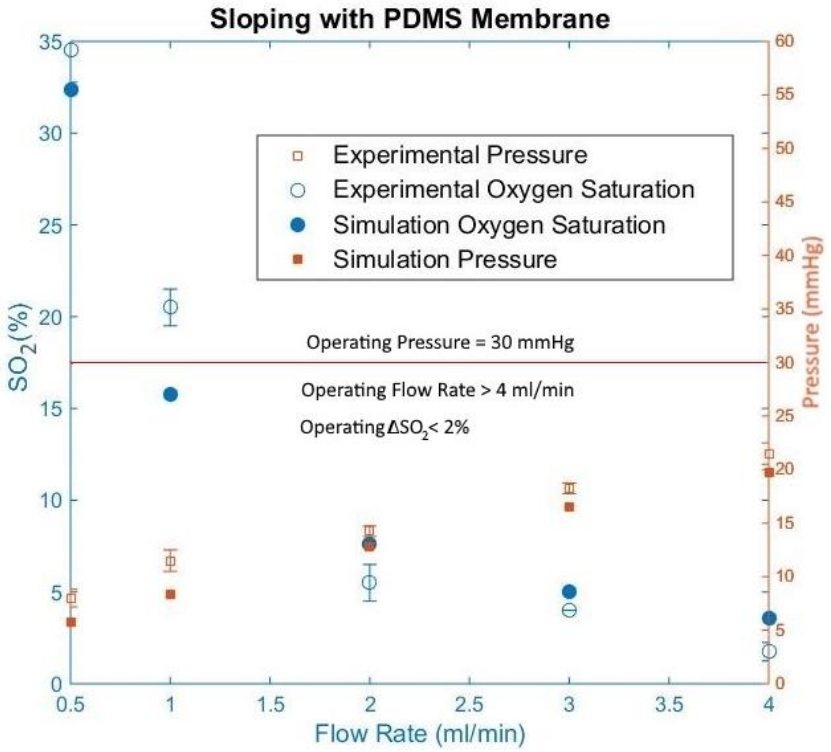

Figure 6.5 Variation of change in oxygen saturation and pressure drop with flow rate for sloping device with PDMS membrane. The height of the device varies from 170 µm to 60 µm and the device width is 43 mm as previously explained in section 4.2 of chapter 4.

Figure 6.5 presents the performance of the oxygenator of sloping cross-sectional design at various flow rates. Similar to flat cross-sectional design, change in oxygen saturation and blood flow rate at the mean operating pressure (30 mmHg) are used for comparative analysis

The change in oxygen saturation and blood flow rate at the operating pressure for sloping design with PDMS membrane was less than 2% and more than 4 ml/min respectively. The total oxygen uptake would likely to be around 9.6 µL/min. The sloping design was developed with the expectation that it would perform better than the flat design.

However, the designs were conceived under the assumption that the membrane does not expand. In reality, the membranes undergo significant expansion under higher operating pressures and the sloping design offers lower flow resistance and hence allows much larger flow rate. This reduces the residence time of the blood in the oxygenator significantly and affects the amount of increase in oxygen saturation that can be achieved under the operating pressure. Therefore, the sloping design does not fulfil the requirement of an artificial placenta as the change in oxygen saturation is 2% and the required change in oxygen saturation is 35%.

6.1.3.3 Oxygenator with Flat Profile and Composite Membrane

A composite membrane with steel mesh reinforcement was designed and used in order to prevent expansion of the gas exchange membrane under the operating pressure that led to the poor performance of the PDMS membrane as described in the previous section.

Figure 6.6 presents the performance of the oxygenator of flat cross-sectional design with composite membrane at various flow rates. Similar to devices analyzed so far, change in oxygen saturation and blood flow rate at the mean operating pressure (30 mmHg) are used for comparative analysis

The flat design with composite membrane exhibited a change in oxygen saturation of 18% at a flow rate of 1.2 ml/min at the operating pressure of 30 mmHg. In case of flat device with composite membrane, the total oxygen uptake is 26 µL/min, which is 44% higher than the oxygen uptake of flat design with PDMS membrane. The increase in oxygen uptake can be attributed to higher stiffness of composite membrane as compared to PDMS membrane because of which channels do not expand, which in turn causes the flow rate to reduce, which results in an increase in residence time that aids with the oxygenation. In

addition, the smaller expansion of the stiffer composite membrane maintains the oxygen diffusional length in the blood which also aids with the higher oxygenation. As a result, higher overall oxygen uptake was observed as compared to device with PDMS membrane, but the operating flow rate is lower.

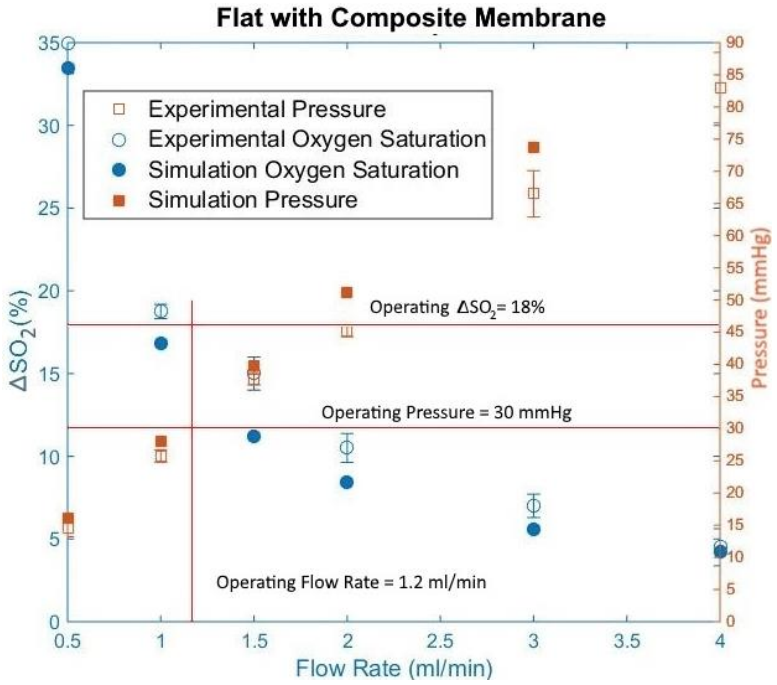

Figure 6.6 Variation of change in oxygen saturation and pressure drop with flow rate for flat device with composite membrane. The height and the width of the device are 100 µm and 43 mm as previously explained in section 4.2 of chapter 4.

6.1.3.4 Oxygenator with Sloping Profile and Composite Membrane

Similar to flat device, the sloping device was also used with composite membrane to improve the performance. Also, change in oxygen saturation and blood flow rate were measured at mean operating pressure (30 mmHg) for comparative analysis.

The change in oxygen saturation and blood flow rate at 30 mmHg pressure drop for sloping design with composite membrane is 8% and 2 ml/min respectively (figure 6.7). The overall oxygen uptake is 19.6 µL/min, which is 115% higher than the oxygen uptake

of the sloping design with PDMS membrane. This increase in performance can be attributed to the higher stiffness of the composite membrane because of which membrane deflection is avoided. When the channel height is maintained, the device offers high flow resistance and hence much smaller flow rates.

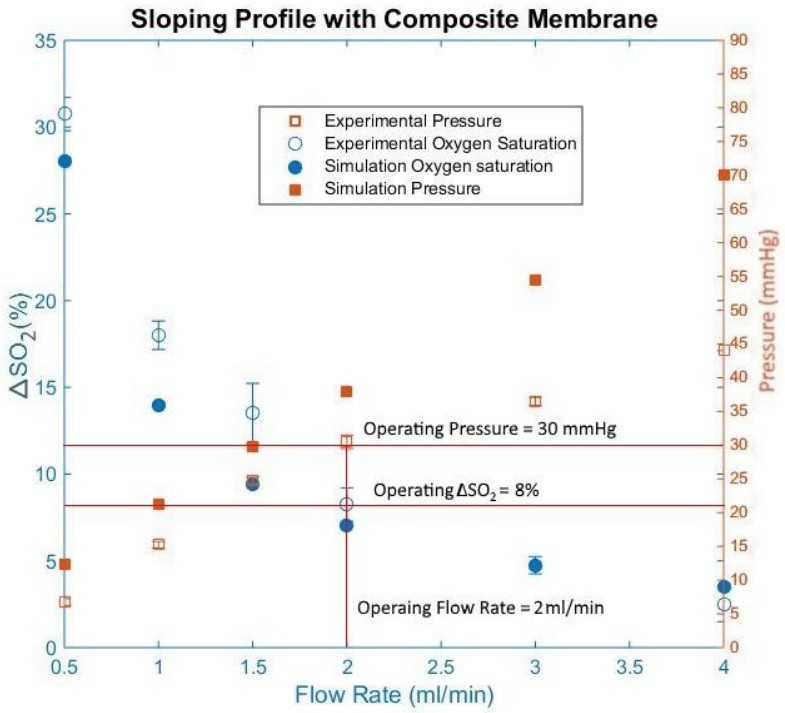

Figure 6.7 Variation of change in oxygen saturation and pressure drop with flow rate for sloping device with composite membrane. The height of the device varies from 170 µm to 60 µm and the device width is 43 mm as previously explained in section 4.2 of chapter 4.

This increases the residence time of the blood in the oxygenator significantly and improves the oxygen uptake. Flat profile device with composite membrane exhibited better performance than flat profile device with PDMS membrane because of the same reason. Hence, the designs with composite membrane performs better than the designs with PDMS membrane. The sloping design with composite membrane have similar performance as the flat design with composite membrane as both devices have similar oxygen uptake, but the

sloping design has higher operating flow rate and the flat design has higher change in oxygen saturation. Also, even though the performance has significantly improved by introducing composite membrane, the devices with composite membrane does not completely fulfil the requirement of an artificial placenta as the maximum change in oxygen saturation achieved at the operating pressure was 8% while the requirement is 35%. Hence, the designs need further optimization.

The chapter presents results of the experimental testing of various designs. Burst pressure testing show devices with composite membrane have the lowest failure rate as compared to devices with PDMS membrane. Performance characterization with blood show devices with composite membrane to have higher oxygen uptake at the operating pressure as compared to the devices with PDMS membrane. Therefore, it can be concluded that the use of a steel mesh reinforced PDMS composite membrane not only provides greater structural integrity but also provides higher oxygenation of blood. The flat-composite design provides higher oxygen saturation increase albeit at lower flow rate, while the sloping-composite design provides a slightly lower oxygen saturation increase at a slightly higher flow rate. Fabrication complexity of the sloping design is significantly higher than that of the flat design and must be taken into consideration when choosing an optimal design for the device. Nevertheless, a simulation based optimization of the dimensions of these designs will be needed to determine the right design choice and dimensions that can meet the oxygenation needs of neonates.

In next chapter, mathematical model will be used to do parametric analysis of flat and sloping design. The analysis will entail various strategies to improve the performance of a device.

Chapter 7 – Parametric Analysis

In this chapter, the mathematical model developed in chapter 5 has been applied to the sloping design and the flat design. A parametric analysis of the geometry of both the designs has been done. The analysis identifies trends device performance like change in oxygen saturation and pressure drop, to changes in the geometrical parameters such as channel height, membrane thickness, and device height and helps optimize the design to achieve better performance.

7.1 Analysis Methodology

Effect of geometric parameters of various designs has been analyzed using the model developed in chapter 5. The analysis was done for one parameter at a time, while the other parameters are kept constant. The analysis was done by assuming that the blood was at standard physiological conditions: pH = 7.4, pCO_2 = 27 mmHg, T = 37 degree Celsius. The oxygen saturation of the input blood was taken as 65%.

All geometrical parameters (channel height, device width, and membrane thickness) were analyzed in isolation; i.e. the parameter being analyzed was allowed to vary while the others are kept constant. The parameter was analyzed by plotting the characteristic curves representing variation of the change in oxygen saturation of blood and the pressure drop with the blood flow rate, which are the output parameters on the same graph. In the analysis, the axis for the change in oxygen saturation ranges from 0 – 35% and the pressure drop axis ranges 0-30 mmHg. The limit for oxygen saturation was chosen based on the physical limit. Typically the venous blood for neonates has an oxygen saturation of not less

than 65%. Therefore, it cannot gain more than 35% in oxygen saturation. The limit for pressure drop was chosen based on the observed artereo-venous pressure difference in neonates.

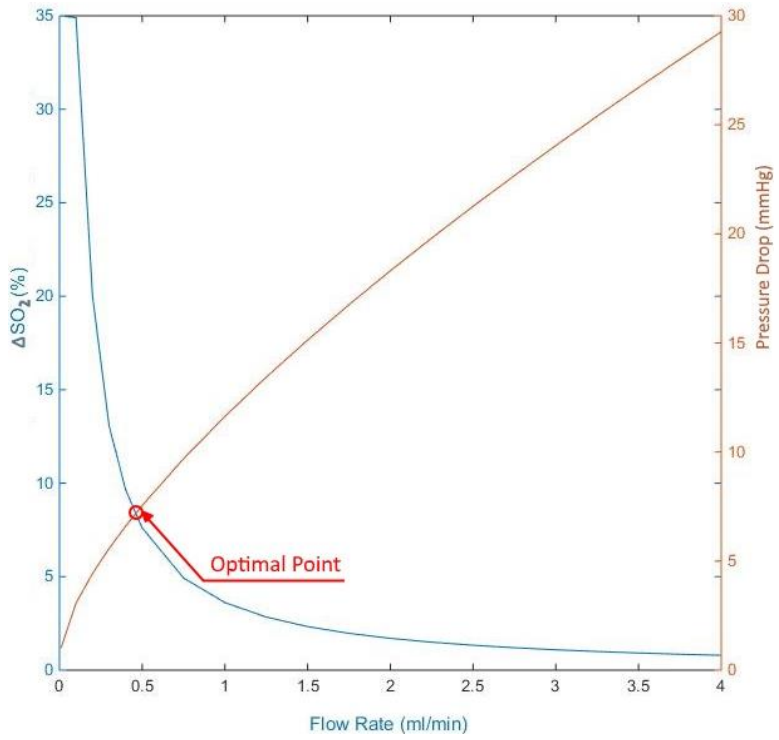

Figure 7.1 Illustration of oxygen saturation characteristic curve (Blue) and Pressure drop characteristic curve (brown). Point of intersection of these two curve is the optimal point of performance.

Figure 7.1 illustrates typical characteristic curves for oxygen saturation and pressure drop for an oxygenator. As the blood flow rate increases, the increase in oxygen saturation achieved decreases and the pressure drop increases. This is a universal observation among microfluidic oxygenators open to the atmosphere. The increase in saturation of blood as it flows through the oxygenator reduces with increase in flow rate as its residence time reduces. Pressure is the product of the hydraulic resistance and the flow rate. Hence, the pressure drop increases as the flow rate increases.

The point where the two curves meet is called the optimal point and can be used to assess the effect of varying a particular parameter on the performance of the device. The most desirable locus of the point is its movement towards the top-right corner of the graph, where the blood is highly oxygenated at a high flow rate and the device operates at the mean pressure (30 mmHg) for a neonate. If the point moves towards the bottom-right or the top-left corner, there is a trade-off to be made between the desirable changes in oxygen saturation and the flow rate.

The next few sections cover analysis of the effect of changes in geometric parameters on the output parameters performed for the various designs under consideration, namely: flat device with PDMS membrane, flat device with composite membrane, sloping design with PDMS membrane, and sloping design with composite membrane.

7.2 Oxygenator with Flat Profile and PDMS Membrane

In this section, geometric parameters of flat device (figure 3.1) with PDMS membrane have been analyzed. In particular, channel height, device width and membrane thickness are varied from a standard geometry within a set range and their effect on oxygen saturation and pressure drop as a function of flow rate have been analyzed. Also, pillar size, pillar spacing, channel height, device width, and membrane thickness of the standard geometry are kept at 1 mm, 1mm, 100 µm, 43 mm, and 50 µm respectively.

7.2.1 Channel Height

First, the channel height was varied from 20 µm to 120 µm in equal increments of 20 µm while keeping the other geometrical parameters of the oxygenator constant and the pressure drop and oxygen saturation increases obtained at various flow rates was plotted. The range

of channel height was chosen based on the manufacturability of the devices with such heights. Also, the height was normalized with respect to 100 µm, which can be considered as a characteristic dimension of channel height that can be fabricated using photolithography at our fabrication facility. So, the normalized height was varied from 0.2 to 1.2.

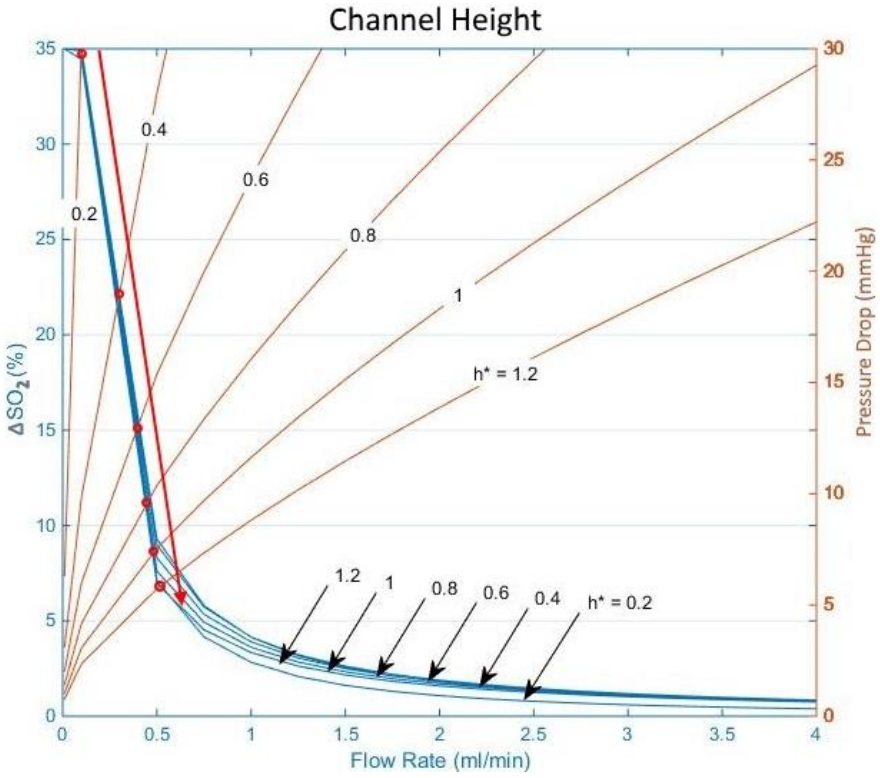

Figure 7.2 Variation of characteristic curves for varying height of a flat device with PDMS membrane. The optimal points are marked by red dots. Notice its downward trajectory as the height is increased.

Figure 7.2 shows the variation of characteristic curves for both pressure drop and oxygen saturation increase for increasing channel height. As it can be seen from the graph, increasing the height leads to minimal change in the characteristic curve for oxygen saturation. The oxygen saturation curve first moves upwards, then moves slightly downwards as the height is increased. This observation aligns with the expectations.

Oxygen taken up by the red blood cells has to diffuse through the gas permeable membrane as well as the blood film. As the channel height is increased, the thickness of the blood film increases causing a longer diffusional distance for the oxygen. This effect causes a slower overall uptake of oxygen. In addition, the channel height is also affected due to the flexible nature of the PDMS membrane, which expands under pressure, increasing the effective channel height. The magnitude of expansion depends on the applied pressure. Devices with smaller channel height require higher applied pressure in order to generate the same flow rate and therefore undergo larger membrane expansion than devices with larger heights. The effect of membrane expansion is more pronounced at smaller height and offsets some of the gains due to reduction in the blood film thickness at smaller channel heights. Therefore the oxygen uptake curves shift slightly upwards, then downwards on decreasing the designed height of the channel.

The pressure characteristic curve is affected by the change in height and moves downwards as the channel height is increased. This behaviour also agrees with the expectations as the pressure drop is inversely proportional to the channel height. So increase in channel height will cause reduction in pressure.

The combined effect of oxygen saturation and pressure drop characteristic curve downwards moving causes the optimal point to move in the bottom right direction as the height is increased. The movement towards the right is desirable as it increases the optimal flow rate and reaches the maximum allowed oxygen saturation of 35% and pressure of 30 mmHg at a channel height of 20 µm. However, the flow rate is 0.1 ml/min at that point, which is insufficient for an oxygenating unit of an artificial placenta.

7.2.2 Membrane Thickness

Next, the effect of the variation of the membrane thickness on the performance of the oxygenator was analysed. Membrane thickness was varied from 25 µm to 100 µm in steps of 25 µm while all the other geometrical parameters were kept constant and the pressure drop and the increase in oxygen saturation of blood at various flow rates was plotted as shown in Figure 7.3. The range was chosen based on the range of membrane thickness that can be manufactured at our fabrication facility. Membrane thickness for each characteristic curve was normalized with respect to 25 µm, which can be considered as a characteristic dimension for thickness. So that the normalized membrane thickness varies from 1 to 4.

It can be seen from Figure 7.3 that as the membrane thickness is increased, the characteristic curve for the change in oxygen saturation remains unchanged. This effect is seen as a result of negligible change in the overall diffusional resistance to the oxygen due to changes in membrane thickness. As described previously, the oxygen diffuses through the membrane and the blood channels. Also, the membrane is flexible in nature and it deforms under operation causing the channels to be larger than they are at rest. As the membrane thickness is increased, it becomes less flexible and undergoes smaller deformation under same pressure. So, the increase of the effective channel height is smaller. Hence, the blood layer in devices with thicker membrane exhibit lower diffusional resistance to oxygen as compared to devices with thin membrane. But, the diffusional resistance to the oxygen from the membrane is higher for thicker membrane. The combined effect of increased resistance from membrane and decreased resistance from blood film compensates each other and causes negligible variation in diffusional resistance.

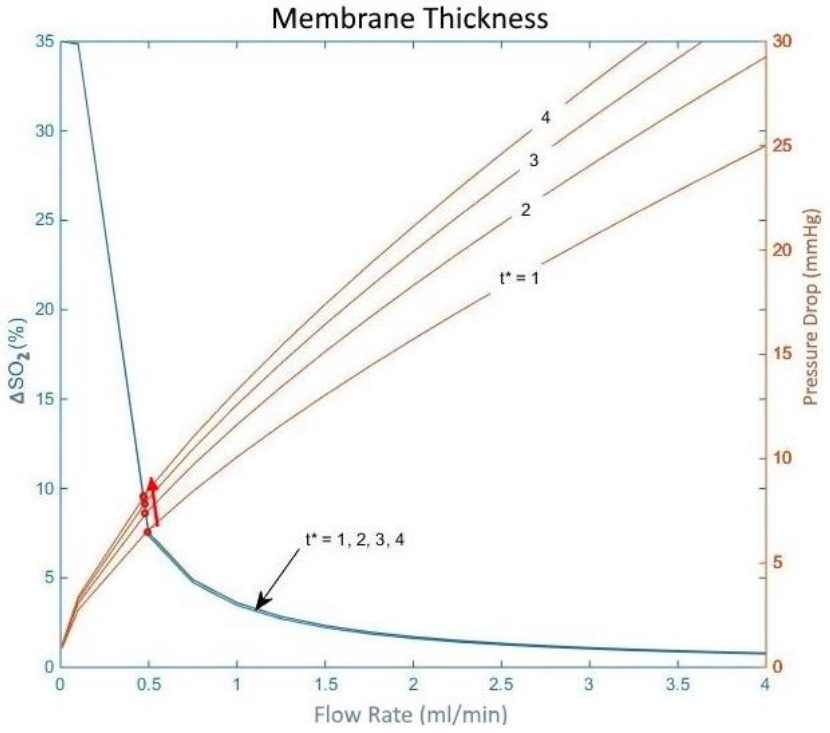

Figure 7.3 Variation of characteristic curves with increasing membrane thickness for flat device with PDMS membrane. Pressure curve moves upwards, while oxygen saturation change curve remains stationary. As a result, the optimal point, marked by red dot, moves towards the top left corner as the thickness is increased

As it can be seen in figure 7.3, pressure characteristic curve moves upwards as the membrane thickness is increased. This effect is seen as a result of the flexible nature of membrane. As discussed previously, thicker membrane undergo smaller deflection for same applied pressure. Hence smaller expansion in channel height is observed. As previously mentioned, pressure drop is inversely correlated with the height. So, the pressure drop increases as the channel height increases.

The combined effect of pressure characteristic curve moving upwards and oxygen saturation curve remaining stationary causes the optimal point to move in the top-left direction. Increasing thickness moves the optimal point upwards which is desirable, but the

optimal point is still in the bottom left corner of the graph. Hence, the configuration is still needs to be improved in order to be suitable as an oxygenating unit of an artificial placenta.

7.2.3 Device Width

Finally, the effect of the variation of the device width on the performance of the oxygenator was analysed. Device width was varied from 10.7 mm to 107.8 mm (device width that fits in a 6 inch wafer) in steps of 10.7 mm ($0.1\sqrt{2}$ inches). The range was chosen to account for the device width that can be manufactured. Currently, devices with width smaller than 43 mm are deemed possible to manufacture based on the equipment available at our research facility. Recent endeavor has been focused on being able to manufacture devices with width 107.8 mm or smaller. For this purpose, the upper cap to the range is chosen at 107.8 mm inches. Also, the width is normalized with respect 53.5 mm ($1/\sqrt{2}$ inches), which is the current maximum device width. So, the normalized width varies from 0.2 to 2.

Figure 7.4 shows the variation of characteristic curves for both pressure drop and oxygen saturation for varying device width. The effect of increasing device width is the upward movement oxygen saturation curve. This effect is observed as a result of increase in gas exchange area and the residence time of blood. Gas exchange area and volume of the device are directly proportional to the device width and the residence time of the blood in the device is directly proportional to the volume of the device. Higher gas exchange area and residence time of the blood implies higher oxygen uptake. Hence, increase in width improves oxygen uptake, driving the oxygen saturation characteristic curve to move upwards.

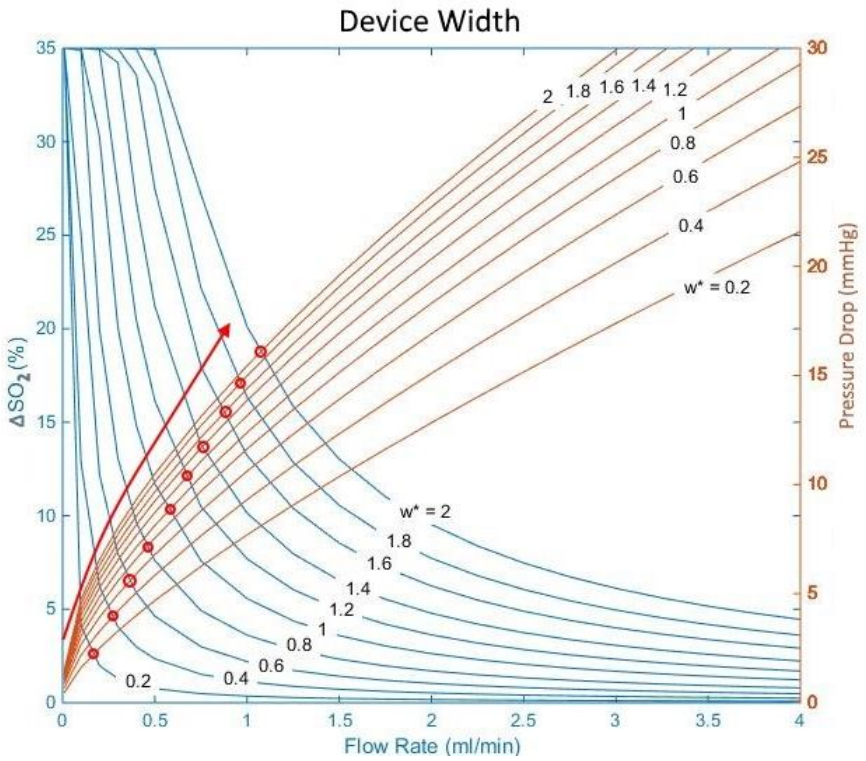

Figure 7.4 Variation of characteristic curves with varying device width for flat device with PDMS membrane. Both curves move upwards as the device width is increased. As a result, the optimal point, marked by red dot, moves towards the top right corner as the width is increased.

Pressure characteristic curve move upwards with increasing width. This effect is seen as a result of increased hydraulic resistance. Since the device is a square shaped, increasing width increases the distance between the inlet and the outlet. Also, increasing distance between the inlet and the outlet increases pressure drop. As a result, increase in device width increases pressure drop.

The combined effect of pressure and oxygen saturation characteristic curves moving upwards with increasing width, causes the optimal point to move in the right and upward direction, which contrasts from the movement of the optimal point in the right and bottom direction on increasing channel height, and decreasing membrane thickness. The movement in the upward-right direction is the desired locus for the optimal point. Hence,

increasing width produces the desired effect. The change in oxygen saturation at the optimal point increases to 18% at 1 ml/min of flow rate. That is a significant improvement from the base configuration, however further development is needed to improve the performance such that the change in oxygen saturation is ~ 35% from the inlet to the outlet.

7.3 Oxygenator with Flat Profile and Composite Membrane

The design configuration consisting of flat channel profile along with a composite membrane was conceived so that membrane expansion at higher operating pressures can be minimized and higher oxygenation can be achieved. In this section, effect of geometrical parameters of a flat device with composite membrane on its performance has been discussed. In particular, the geometrical parameters chosen for analysis are channel height, device width, and membrane thickness. Also, pillar size, pillar spacing, channel height, device width, and membrane thickness of the standard geometry are at 1 mm, 1mm, 100 µm, 43 mm, and 50 µm respectively.

7.3.1 Channel Height

Similar to flat device with PDMS membrane, the channel height was varied from 20 µm to 120 µm in steps of 20 µm and normalized against 100 µm. Hence, normalized channel height was varied from 0.2 to 1.2. The range was chosen to cover the whole spectrum of channel heights that can be manufactured in the current facility.

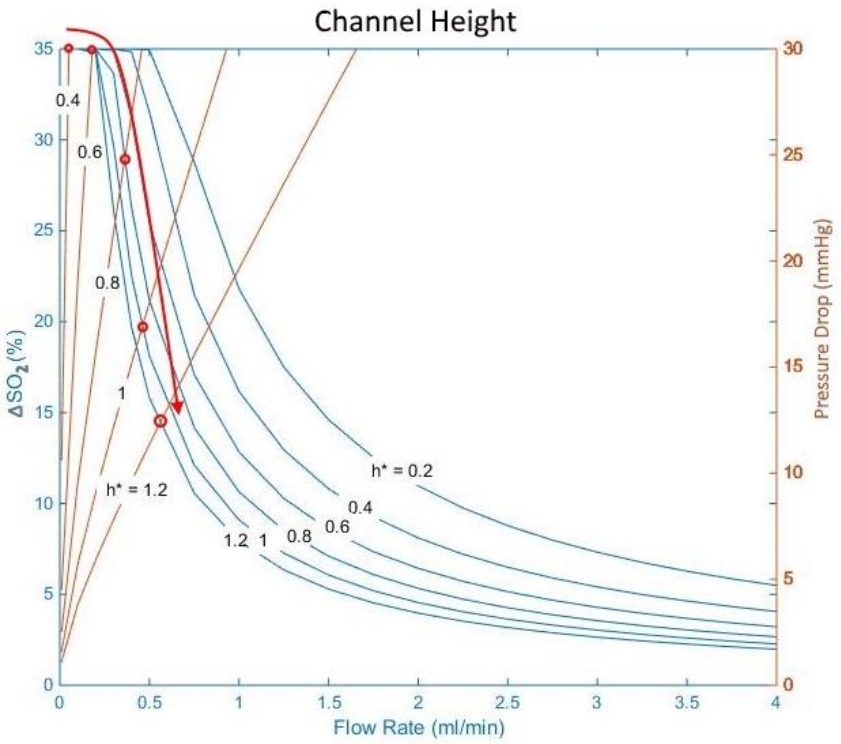

Figure 7.5 Variation of characteristic curve for flat device with composite membrane with varying channel height. Both curves move downwards as the height is increased. Notice as the height is increased, the optimal point moves towards to bottom-right corner.

Figure 7.5 shows the variation of characteristic curves for both pressure drop and oxygen saturation for varying channel height. Increasing the channel height shifts the oxygen saturation characteristic curve downwards. This aligns with expectations. As previously explained, the total amount of oxygen diffusing through the membrane and the blood film is inversely proportional to its thickness. As the thickness of the blood film is increased, the diffusing oxygen faces higher resistance. The thickness of the blood film is equal to the height of the channel. Hence, smaller increase in oxygen saturation is taken up at the same blood flow rate as the channel height is increased.

Pressure characteristic curve also shifts downwards as the channel height is increased. This effect is observed because pressure drop across a device at any given flow rate is inversely

proportional to the channel height. Hence, increase in channel height, decreases pressure drop.

Also, the shift in characteristic curves is larger for devices with composite membrane as compared to PDMS membrane. This effect is a result of inflexible nature of composite membrane. PDMS membrane expands under operation. Increasing channel height will have smaller effect on diffusional and hydraulic resistance as the channels are going to expand under operation regardless. As a result, small shift in characteristic curves is observed. Composite membrane does not expand under operation. Increasing channel height has a large effect on diffusional and hydraulic resistance. As a result, shift in characteristic curves is large.

The combined effect of pressure and oxygen characteristic curves moving downward with increasing channel height causes the optimal point to move in the bottom right direction. Also, because of the introduction of the composite membrane the device exhibits better oxygenation characteristics as it inhibits membrane expansion and maintains channel height under operation. However, the device exhibits lower flow rates as the composite membrane maintains the channel height and as a result, the flow resistance is increased. The change in oxygen saturation is 35% at the flow rate of 0.1 ml/min. However, this flow rate is insufficient for an artificial placenta where design constraints dictate a minimum required flow rate of at least 1 ml/min.

7.3.2 Membrane Thickness

Similar to flat device with PDMS membrane, the thickness of the PDMS only part of the membrane was varied from 0 to 100 µm. Membrane thickness was varied from 40 µm to

140 µm in steps of 25 µm and normalized by 25 µm. The normalized membrane thickness varies from 1.6 to 5.6.

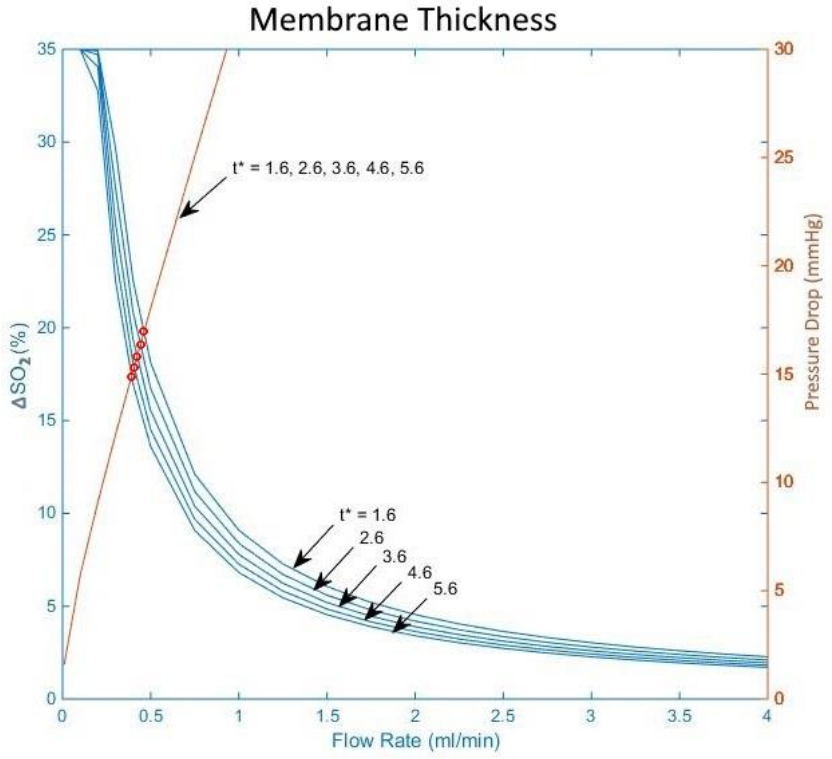

Figure 7.6 Variation of characteristic curves for flat device with composite membrane with varying membrane thickness. The pressure curve remains unchanged, while oxygen saturation curve moves downwards as the membrane thickness is increased.

Figure 7.6 shows the variation of characteristic curves for both pressure drop and oxygen saturation for varying membrane thickness. As the membrane thickness is increased the pressure characteristic curve remain stationary. This effect is observed as a result of the inflexible nature of the membrane. Since the membrane does not expand when device is under operation, the channel height remains unaffected. The channel height remains unaffected even when the membrane thickness is increased. Pressure drop depends on the anatomy of the blood channel network. Since the network is unaffected, the pressure drop will be unaffected as well.

Also, the pressure drop rise is steeper than in a flat design with PDMS membrane in subsection 7.2.2. This effect is also seen as a result of inflexible nature of the membrane. In case of a PDMS membrane, the membrane expands under pressure because of which channels expands and some pressure is release as a result. Composite membrane is reinforced with steel because of which it does not expand under pressure. As a result higher pressure rise is observed.

Increasing membrane thickness moves the oxygen saturation curve downwards slightly. This happens as the contribution of the membrane to the resistance to oxygen flow increases, which slows down the oxygen uptake. Hence the curve moves downwards as the membrane thickness is increased. It can be seen that none of the configurations simulated here using the composite membrane are suitable for an artificial placenta, as the flow rates and the change in oxygen saturation are less than 1 ml/min and 35% respectively.

The optimal point moves towards the left bottom corner of the graph as membrane thickness is increased. In contrast, the optimal point moves towards the bottom-right corner for the flat device with PDMS membrane. This contrasting effect is a result of difference in flexibility of PDMS and composite membrane. PDMS membrane expands under operation and increasing its thickness largely effect pressure characteristic curve, while oxygen saturation curve remains stationary. Composite membrane does not expand under operation and increasing its thickness only effect oxygen saturation curve, while the pressure curve remains stationary.

7.3.3 Device Width

Similar to flat device with PDMS membrane, device width for flat device with composite membrane was varied from 10.78 mm to 86 mm with steps of 10.78 mm and normalized with 53.5 mm. The normalized device width varies from 0.2 to 1.6. The device width was not increased beyond 86 mm because the pressure increases beyond the allowed range.

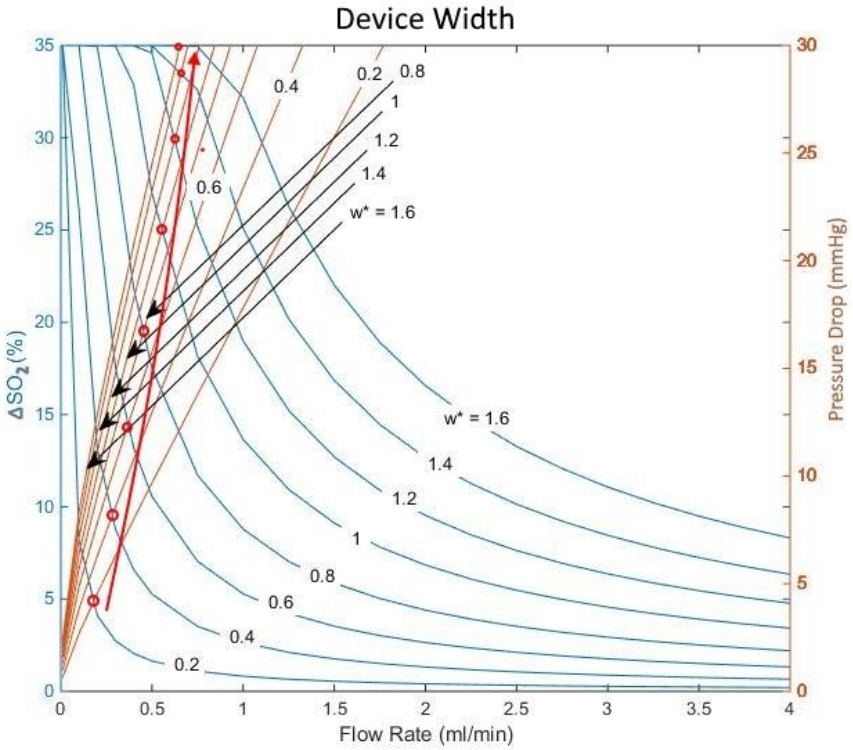

Figure 7.7 Variation of characteristic curves for flat device with composite membrane with varying device width. Both curves move upwards as the device width is increased. This causes the optimal point to move towards the top-right corner.

Figure 7.7 shows the variation of characteristic curves for both pressure drop and oxygen saturation for varying device width. Increasing width moves oxygen saturation characteristic curve upwards. This effect is observed as a result of increase in gas exchange area with increasing width. Amount of oxygen taken up by the blood is proportional to the

area available for gas exchange. Gas exchange area is proportional to the square of the device width. Hence, increase in device width drives oxygen saturation curve upwards.

Pressure characteristic curve also shifts upwards as the device width is increased. This effect is seen as pressure drop is proportional to the length of the device. The length of the device is proportional to the width of the device. Hence, the pressure drop increases as the width of the device is increased.

Flat design with PDMS membrane show similar characteristic curve shifts as composite membrane, but composite membrane exhibit larger shift in characteristic curve. This effect is a result of inflexible nature of composite membrane. PDMS membrane expands under operation. As previously mentioned, this effect relieves the hydraulic pressure and adversely affect the oxygen uptake. Composite membrane does not expand under operation. As a result, hydraulic and diffusional resistance are unaffected. As a result, shift in oxygen saturation curve is smaller as compared to composite membrane.

The combined effect of characteristic curves moving upward with increasing width causes optimal point to move in the top-right direction. This makes increasing device width an attractive option to improve device performance. Also, the device configuration with a normalized width of 1.6, the device exhibits 35% change in oxygen saturation, but the device flow rate is only 0.5 ml/min. Although, the introduction of the composite membrane did improve the capability of the device to effectively increase oxygen saturation, it did so, by introducing a high pressure drop. Therefore, a modified device geometry is needed where the pressure drop is not as high as the flat profile device to get the optimal device performance.

7.4 Oxygenator with Sloping Profile and PDMS Membrane

In this section, effect of geometrical parameters of a sloping profile device on its performance is discussed. In particular, the geometrical parameters chosen for analysis are the maximum channel height, minimum channel height, device width, and membrane thickness. Also, pillar size, pillar spacing, maximum channel height, minimum channel height device width, and membrane thickness of the standard geometry are kept at 1 mm, 1mm, 100 µm, 25 µm, 43 mm, and 50 µm respectively. Increasing maximum channel height and minimum channel height causes the optimal point to move in the bottom right direction. Similar effect is seen for decreasing membrane thickness. For increase in device width, the point moves towards the top-right corner.

7.4.1 Maximum and Minimum Height

Maximum channel height was varied from 60 µm to 180 µm, while minimum height varies from 20 µm to 150 µm and normalized against 100 µm. Hence, the normalized maximum and minimum channel height varies from 0.6 to 1.8 and 0.2 to 150 respectively. The range is chosen to include the set of heights used for parametric analysis of a flat device.

Figure 7.8 and Figure 7.9 shows the variation of characteristic curves for both pressure drop and oxygen saturation for varying maximum channel height and minimum channel height respectively. Increasing the maximum channel height or the minimum channel height moves oxygen saturation curve downwards. This effect is observed as a result of increasing overall diffusional resistance to oxygen with increasing channel height. As the maximum channel height or the minimum channel height increases, the average channel height increases. As the average channel height increases, the oxygen diffusing in the

device will face higher diffusional resistance from the blood film. Hence, lesser amount of oxygen will be taken up.

Pressure characteristic curve moves downwards as the maximum or the minimum channel height is increased. This effect is observed as a result of decreasing hydraulic resistance. As previously mentioned, pressure drop is inversely correlated with the channel height. If any of the maximum or the minimum channel height is increased, the average channel height increases. Hence, the pressure drop decreases.

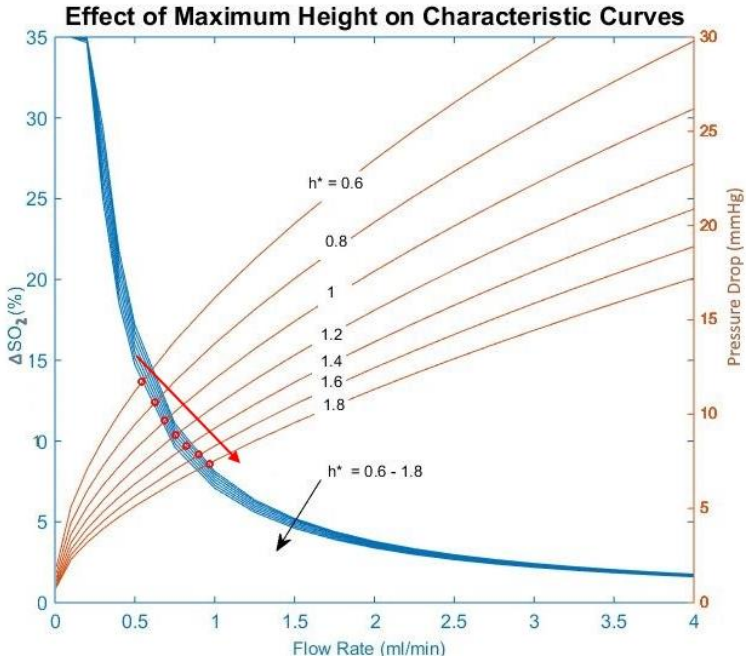

Figure 7.8 Variation of characteristic curve for sloping profile device with PDMS membrane for varying maximum channel height. Both curves move downwards as the height is increased, causing the optimal point to move towards the bottom-right corner.

Also, shifts in pressure drop characteristic curve is smaller and the change in oxygen saturation is larger in case of sloping profile as compared to flat profile. The pressure drop characteristic depends on the height profile and changing height changes the height at all points in the device by the same amount in case of a flat device, while changing either

maximum height or minimum height changes the height by proportional amount at different points in sloping device. As a result, effect of changing height in case of flat profile is larger as compared to the sloping profile. Also, the shifts in oxygenation characteristics is large in case of changing minimum height for sloping profile, as the region in which the height is minimum has a large gas exchange area. As a result, the oxygenation characteristic gets significantly affected by the minimum height.

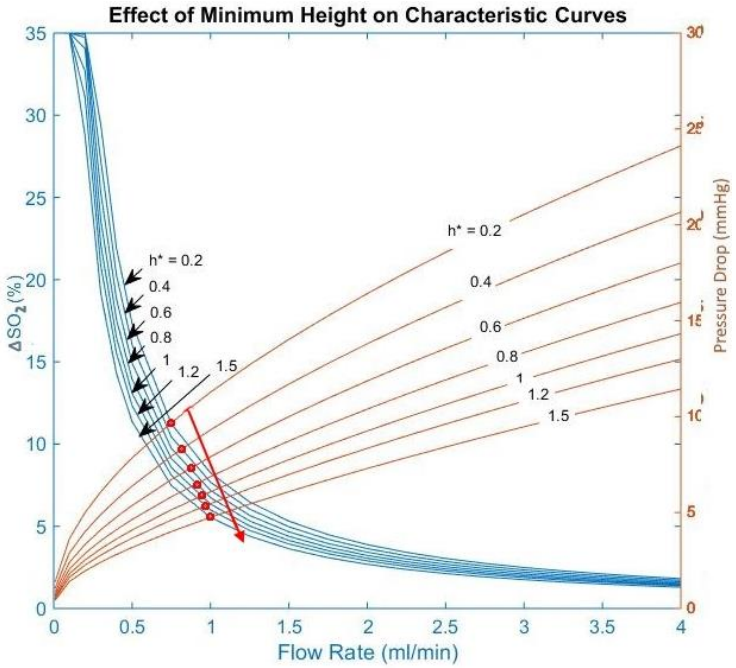

Figure 7.9 Variation of characteristic curve for sloping profile with PDMS membrane for minimum channel height. Both curves move downwards as the height increased, causing the optimal point to move towards the bottom-right corner.

The combined effect of the characteristic curves moving downwards is that the optimal point moves in the bottom-right direction. Adjusting maximum or minimum channel height places a trade-off between the oxygen saturation and the operating flow rate. Also, the sloping profile has lower pressure drop as compared to the flat profile, but it also exhibits lower oxygenation characteristics. Also, none of the configurations are suitable to be used

for an artificial placenta as the change in oxygen saturation and the flow rate are less than 35% and 1 ml/min.

7.4.2 Membrane Thickness

Similar to the flat device with PDMS membrane, membrane thickness was varied from 25 µm to 100 µm with steps of 25 µm and normalized with 25 µm. The normalized membrane thickness varies from 1 to 4. As previously mentioned, the range is chosen based on their manufacturability and commercial availability.

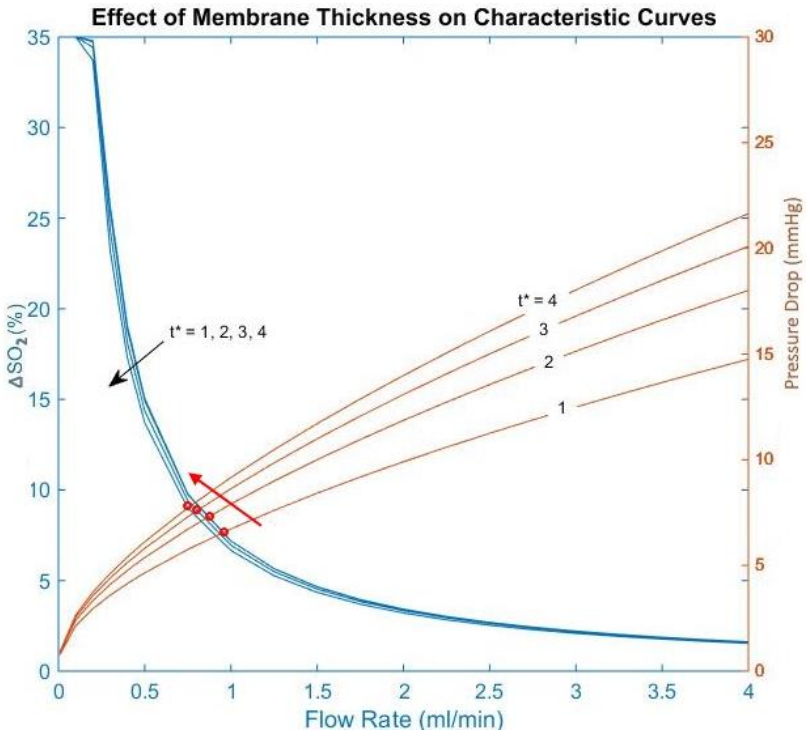

Figure 7.104 Variation of characteristic curves for sloping profile device with PDMS membrane for varying membrane thickness. Both curves move downwards as the thickness is increased. This causes the optimal point to traverse towards the top-left corner.

Figure 7.10 shows the variation of characteristic curves for both pressure drop and oxygen saturation for varying membrane thickness. Increasing membrane thickness causes the characteristic curves to behave in the similar as they do for the flat device. Small decrease in the overall diffusional resistance to the oxygen causes the oxygen saturation curve to move slightly downwards. While increase in hydraulic resistance for thicker membrane generates a higher pressure drop Also, the effect of changing membrane thickness on the performance of the flat profile device is similar to its effect on the performance of the sloping profile device. This is expected as the membrane deflection is independent of the device geometry and is unlikely to show any difference in performance based on the difference in geometry Also, it can be seen that none of the configuration simulated for the sloping profile with PDMS membrane are suitable for an artificial placenta as they do not exhibit required amount of change in oxygen saturation (35%).

Similar to flat device with PDMS membrane, the device width was varied from 10.78 mm to 107.8 mm and normalized against 53.5 mm. The normalized device width varies from 0.2 to 2. The range was chosen based on current and potential future manufacturing abilities. Increasing width produces similar effect with characteristic curves as it does with the other devices. Increasing width causes the characteristic curves to move upwards.

7.4.3 Device Width

Figure 7.11 shows the variation of characteristic curves for both pressure drop and oxygen saturation for varying device width. Increasing device width shifts the characteristic curves upwards, which is a result of increase in gas exchange area and hydraulic resistance for oxygenation and pressure characteristic respectively. The effect of increasing the device width on its performance in case of sloping device is similar to the effect on the

performance in case of the flat device, but the sloping device exhibit lower pressure drop. As a result, the maximum oxygen saturation that can be obtained was 18% at a flow rate of 2 ml/min as compared to 18% at 1 ml/min. This is a significant improvement over flat device, but further development is needed to improve the oxygenation characteristics. Therefore, the sloping profile design is combined with the composite membrane that demonstrated promising characteristics and analysed in the net section.

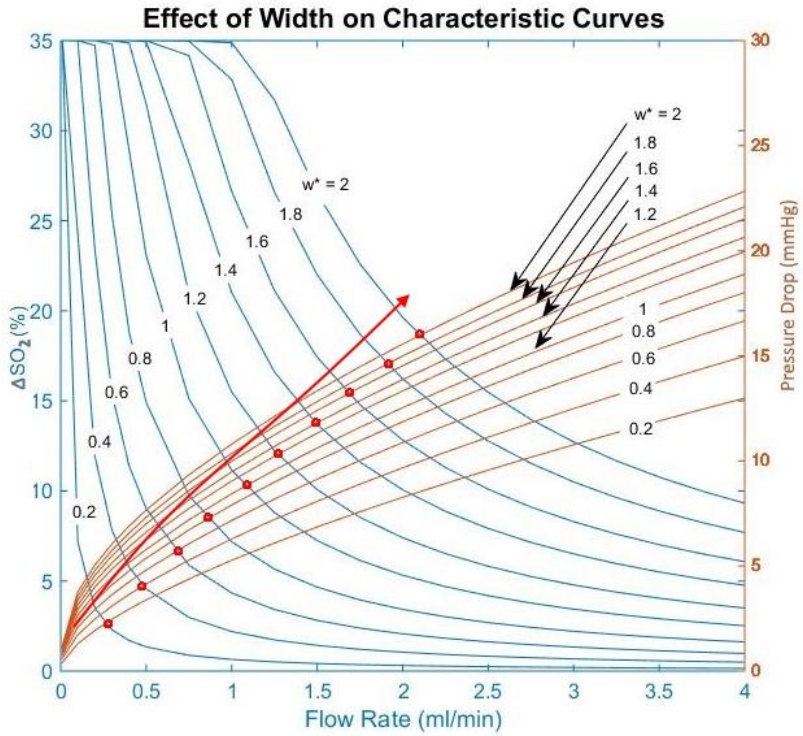

Figure 7.11 Variation of characteristic curves for sloping profile with PDMS membrane for varying device width. Both curves move upwards as the width is increased. This causes the optimal point to traverse towards the top-right corner.

7.5 Oxygenator with Sloping Profile and Composite Membrane

This section discusses the effect of geometrical parameters of a sloping profile device with composite membrane on its performance. In particular, maximum channel height, minimum channel height, membrane thickness, and device width are chosen for the

analysis. Also, pillar size, pillar spacing, maximum channel height, minimum channel height device width, and membrane thickness of the standard geometry are kept at 1 mm, 1mm, 170 µm, 60 µm, 43 mm, and 50 µm respectively.

7.5.1 Maximum and Minimum Channel Height

Similar to sloping device with PDMS membrane, maximum channel height was varied from 60 µm to 180 µm and minimum height was varied from 40 µm to 120 µm with steps of 20 µm and normalized against 100 µm. The normalized maximum channel height and minimum channel height varies from 0.6 to 1.8 and 0.4 to 1.2 respectively. The range was chosen to include the set of heights used for parametric analysis of a flat device, while eliminating the values for which the pressure drop falls out of range.

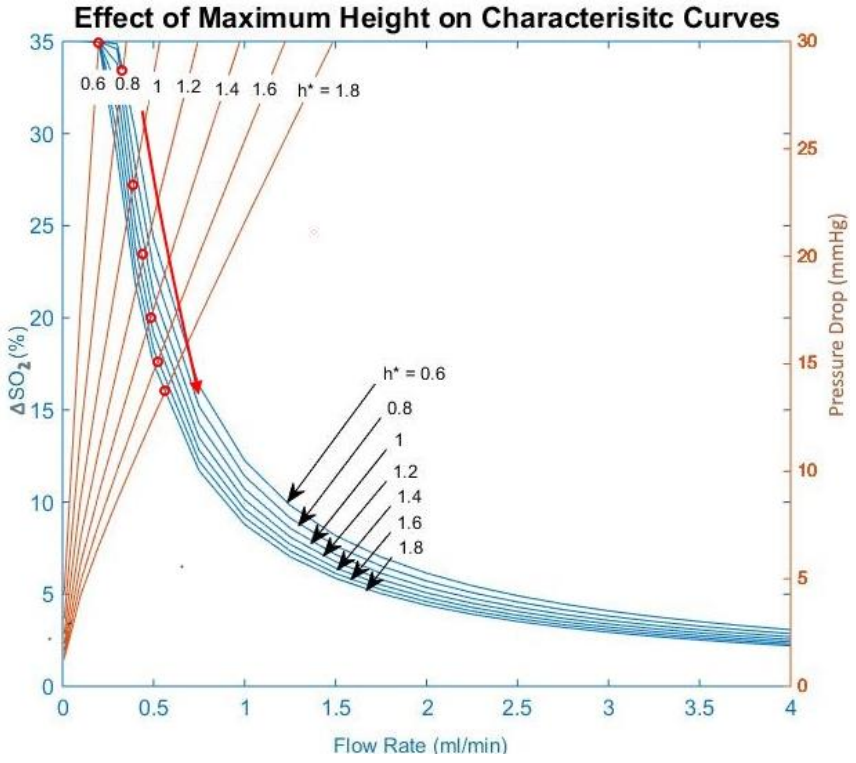

Figure 7.12 Variation of characteristic curves for varying maximum channel height for sloping device with composite membrane. Both curves move downwards as the height is increased. Notice the optimal point traverses a horizontal path before moving downwards

Figure 7.12 and figure 7.13 show the variation of characteristic curves for both pressure drop and oxygen saturation for varying maximum channel height and minimum channel height respectively. Increasing maximum height produces similar effect with characteristic curves as it does with the sloping device with PDMS membrane. Oxygen saturation curve moves downwards as the diffusional resistance increases as a result of increase in average channel height.

Similarly, pressure curve moves downwards as the hydraulic resistance decreases. As a result, the optimal point moves towards the bottom-right direction. Also, the effect of changing the height is stronger in case of a flat device as compared to a sloping device. This is because the channel height increases by the same amount at all points in the device in case of flat device as the height is increased while the channel height increases by proportional amount at all points in the device in case of sloping device as the maximum height or the channel height. For example, increasing maximum height in case of sloping device will increase the height at the inlet and the outlet by the same amount the maximum height is increased, while the height at the center of the device remains unaffected as the minimum height is not changed. Also, for all the points in between the center and the inlet, the height will increase proportional to the distance of the point from the inlet. As a result, the effect of channel height on the performance is stronger in case of flat device as compared to sloping device.

Similar effects are observed for minimum channel height. The characteristic curves move downwards as the hydraulic resistance decreases and diffusional resistance increases with increasing minimum channel height. High pressure drops at low minimum channel height

causes the optimal point to occur at the top edge of the graph and it moves downwards the height is increased.

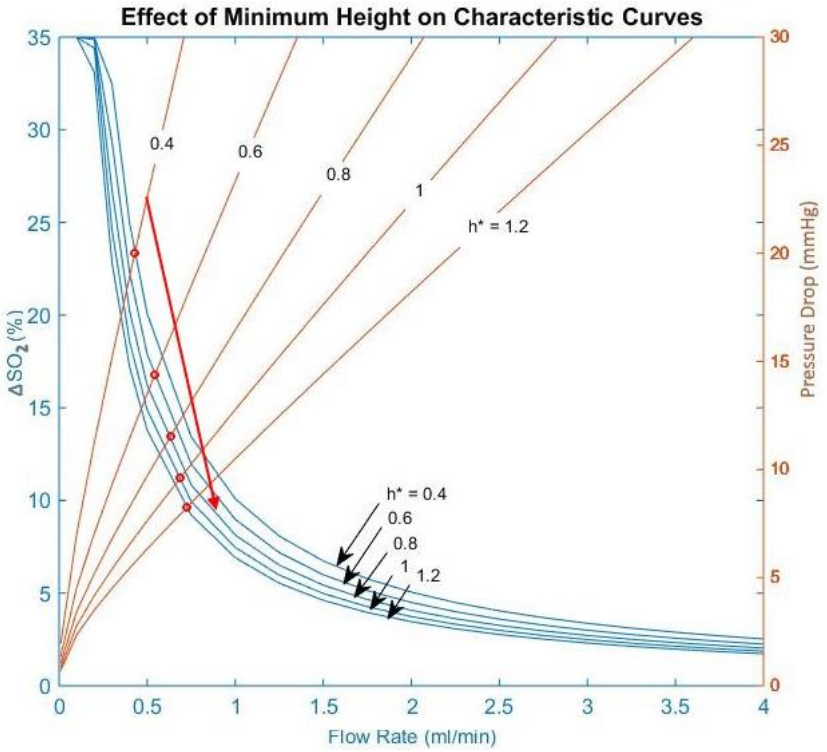

Figure 7.13 Variation of characteristic curves for varying minimum channel height for sloping device with composite membrane. Both curves move downwards as the height is increased. Notice the optimal point traverses a horizontal path before moving downwards

The shift in characteristic curve is small for sloping device with PDMS membrane as compared to sloping device with composite membrane. The reasoning behind this effect is the same as for flat device and is explained in section 7.3. As a result, the oxygenation characteristic has significantly improved. Nevertheless, none of the configurations that have been simulated in this section and completely suitable as they exhibit flow rate lower than 1 ml/min.

Also, the sloping profile with composite membrane exhibits better oxygenation characteristics and higher flow rates. This is in accordance with the expectations as the sloping profile has varying height, which improves oxygenation and reduces pressure drop.

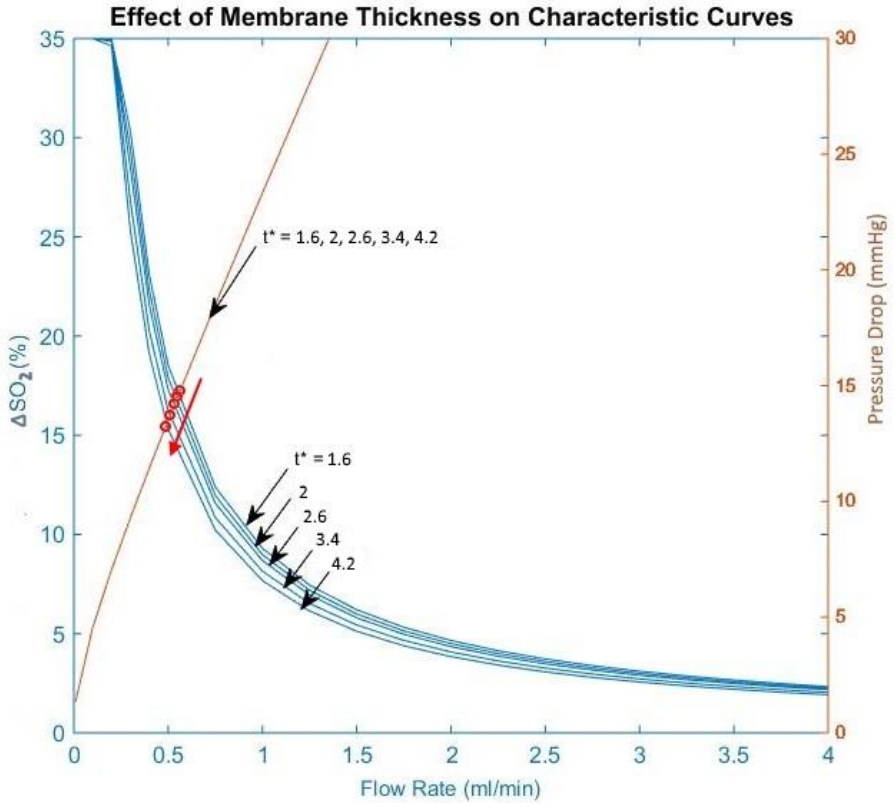

Figure 7.14 Variation of characteristic curves for varying membrane thickness for sloping device with composite membrane. Pressure curve remains unchanged, while oxygen saturation curve moves downwards as the membrane thickness is increased. Notice the optimal point does not move at all.

7.5.2 Membrane Thickness

Similar to flat device with composite membrane, the membrane thickness was varied from 40 µm to 140 µm with steps of 25 µm. The membrane thickness was normalized with 25 µm and normalized membrane thickness varied from 1.6 to 5.6.

Figure 7.14 shows the variation of characteristic curves for both pressure drop and oxygen saturation. As the membrane thickness increases, the resistance to oxygen diffusion also

increases which results in the downward shift of the oxygen saturation curve. In contrast, the hydraulic resistance is unaffected by the changes in membrane thickness, in case of the composite membrane, resulting in no change to the pressure curve.

The combined effect causes the optimal point to move in the bottom left direction as the membrane thickness is increased, while the optimal point for sloping device with PDMS membrane moves in the bottom-right direction of the graph. The reasoning is the same as for flat design. The reasoning is based on the difference between the material properties of PDMS membrane and composite membrane, and is explained in section 7.3.Also, the movement of the optimal point is slight because of which none of the configuration reach the required operating point for an artificial placenta.

7.5.3 Device Width

Similar to flat device with composite membrane, the device width was varied from 10.78 mm to 97 mm with steps of 10.78 mm. The device width was normalized with 53.5 and the normalized device width varies from 0.2 to 1.8.

Figure 7.15 shows the variation of characteristic curves for both pressure drop and oxygen saturation for varying. Increasing device width causes both characteristic curves to move upwards. This effect is seen as a result of increase in gas exchange area and hydraulic resistance. Increase in device width causes increase in gas exchange area, which in turn increases the amount of oxygen taken up. Hence the oxygen saturation curve moves upwards. Also, increase in device width causes increases in hydraulic resistance, which in turn increases the pressure drop. Hence, the pressure curve moves upwards.

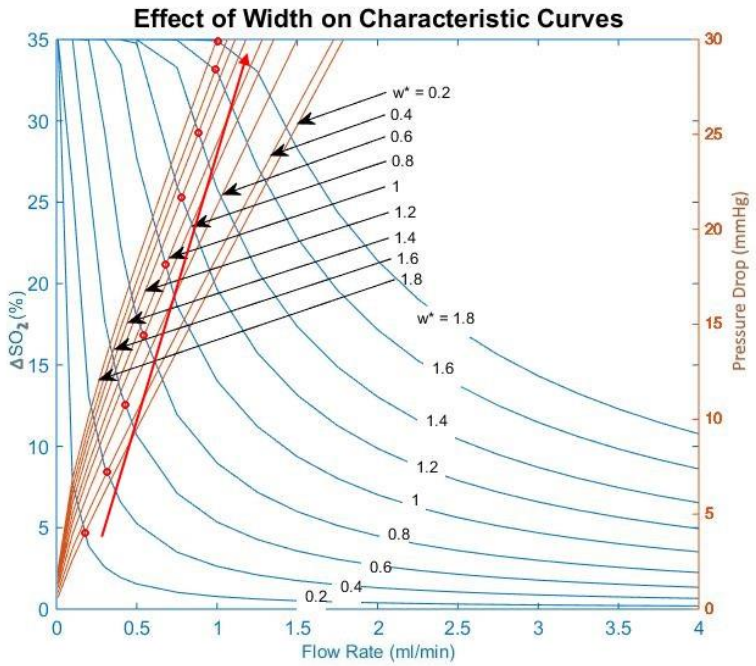

Figure 7.15 Variation of characteristic curves for sloping profile with composite membrane for varying device width for sloping device with composite membrane. Both curves move upwards as the width is increased. This causes the optimal point to traverse towards the top edge before it moves towards the top-left corner.

The optimal point moves towards the upper-left corner of the graph as the device width is increased. The slope of the line along which point moves is steeper than for the sloping device with PDMS membrane. This difference in behavior is also seen between flat device with PDMS membrane and composite membrane. The cause of this behavior is the difference between the material properties of PDMS membrane and composite membrane. This effect is a result of inflexible nature of composite membrane. PDMS membrane expands under operation. As previously mentioned, this effect relieves the hydraulic pressure and adversely affect the oxygen uptake. Composite membrane does not expand under operation. As a result, hydraulic and diffusional resistance are unaffected. As a result, shift in oxygen saturation curve is smaller as compared to composite membrane.

Also, the sloping device with composite membrane exhibit 35% change in oxygen saturation at a flow rate of 1 ml/min for a non-dimensionalized width of 1.8. Such a device can be used as an oxygenating unit for an artificial placenta, as it fully oxygenates the blood at a reasonable flow rate under operating pressure.

7.6 Discussion

In this section, parametric analysis is further discussed to identify the parameters with significant effect on the optimal point. The extent by which the optimal point moves for unit change in the parameter is of interest as it is an indicator of the dependence of the performance depends on the parameter. Also, the direction in which the optimal point moves is also of interest as it informs about the relationship between the change in oxygen saturation and the blood flow rate at the optimal points for different values of a parameter.

The length of the vector joining the position of the optimal point for the minimum value and the maximum value of the parameter, is used to represent the extent by which the optimal point moves. Similarly, the angle the vector makes with the horizontal axis, is used to represent the direction of the movement of the optimal point. Figure 7.16 illustrates the vector on a graph, by joining the optimal point for the maximum value and the minimum value of the parameter, by a straight line. The parameter varies from 'h' to 'l' for which the change in oxygen saturation are $\Delta sO_{2,h}$ and $\Delta sO_{2,l}$ respectively and the blood flow rates are $Q_{b,h}$ and $Q_{b,l}$ respectively. The normalized length of the vector is L* and the angle it makes with the horizontal axis is φ. The normalized length is the length of the vector, obtained by dividing the horizontal component and the vertical component of the vector joining the optimal points at the maximum and the minimum value of the parameter, by

the length of the horizontal axis and the vertical axis respectively, and the difference in the maximum and the minimum value of the parameter. The equation to calculate the normalized length is given by the following:

$$L^* = \frac{\sqrt{\left(\frac{\Delta sO_{2,h} - \Delta sO_{2,l}}{35}\right)^2 + \left(\frac{Q_{b,h} - Q_{b,l}}{4}\right)^2}}{h - l}$$

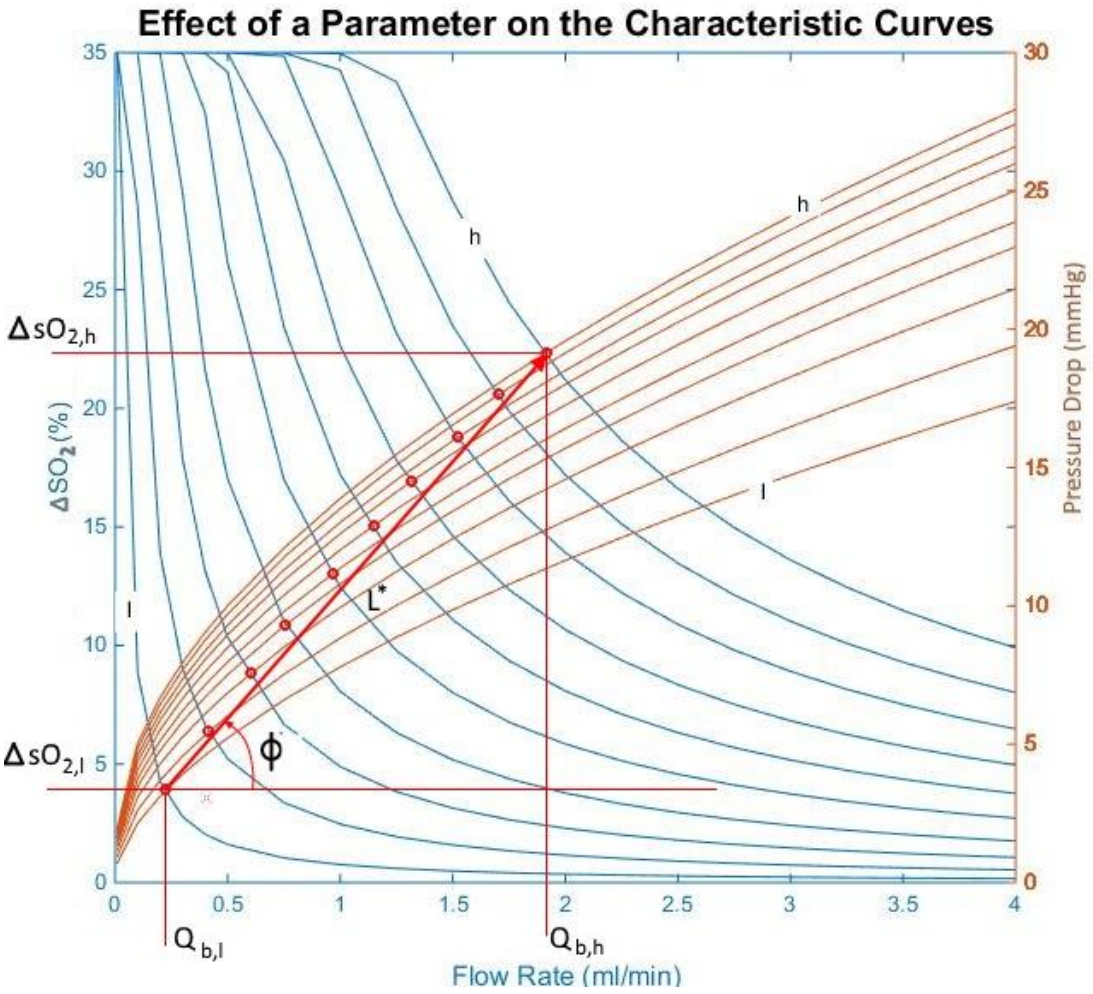

Figure 7.16 Illustration of the vector joining the optimal points at the maximum value and the minimum value of the parameter by a straight line.

Here, 35 and 4 are the maximum change in the oxygen saturation and the maximum blood flow rate marked on the graph. The following equation is used to calculate the angle:

$$\emptyset = \tan^{-1}\left(\frac{\Delta sO_{2,h} - \Delta sO_{2,l}}{Q_{b,h} - Q_{b,l}} * \frac{4}{35}\right)$$

Here $\emptyset$ is the angle the vector makes with the horizontal axis.

Table 7.1 lists the normalized length and the angle of the vector representing the optimal point movement for the analysis of various parameters. It can be seen that the width and the height have the most significant effect on the performance, with width producing desirable effect while height producing neutral effect. Increasing width increases the change in oxygen saturation and the blood flow rate at the optimal point, while increasing height decreases the oxygen saturation and increases the blood flow rate at the optimal point.

Device	Membrane	Max Height (µm)	Min Height (µm)	Width (mm)	Membrane Thickness (µm)	Normalized Length (L^*)	Angle 'φ' (Degree)
Flat	PDMS	20-100	-	43	50	0.82	-81
		100	-	43	25-100	0.02	102
		100	-	10.7-107	50	0.29	61
	Composite	20-100	-	43	50	0.6	-76
		100	-	43	40-140	0.02	-103
		100	-	10.7-64.6	50	0.46	80
Sloping	PDMS	60-180	60	43	50	0.15	-49
		170	20-160	43	50	0.13	-66
		170	60	43	25-100	0.02	141
		170	60	10.7-107	50	0.36	47
		60-180	60	43	50	0.46	-79

	Composite	170	40-160	43	50	0.5	-79
		170	60	43	40-100	0.02	-113
		170	60	10.7-97	50	0.55	79

Table 7.1 Table listing effect of various geometric parameters on the movement of optimal point.

Currently, the only configuration that fulfils the requirement of an artificial placenta is for the sloping device with composite membrane with device width of 97 mm, maximum and minimum channel height of 170 µm and 60 µm respectively, and membrane thickness of 50 µm. At this configuration the device is expected to have a 35% change in oxygen saturation, 30 mmHg pressure drop, and 1 ml/min flow rate. The performance can be optimized by increasing the maximum height and increasing device width. As increasing the maximum height reduces the pressure drop significantly and reduces the oxygen uptake slightly and increasing device width increases pressure drop slightly and increases the oxygen uptake significantly. First, the normalized device width is increased to 2. The results are plotted in figure 7.17. The operating point now exhibits 35% oxygenation at 0.9 ml/min flow rate. This is slightly below the requirement as the operating flow rate is required to be above 1 ml/min. Now, the maximum height is increased to its maximum limit (200 µm) to reduce the pressure drop. The device now exhibits slightly over 34% oxygenation at 1.25 ml/min.

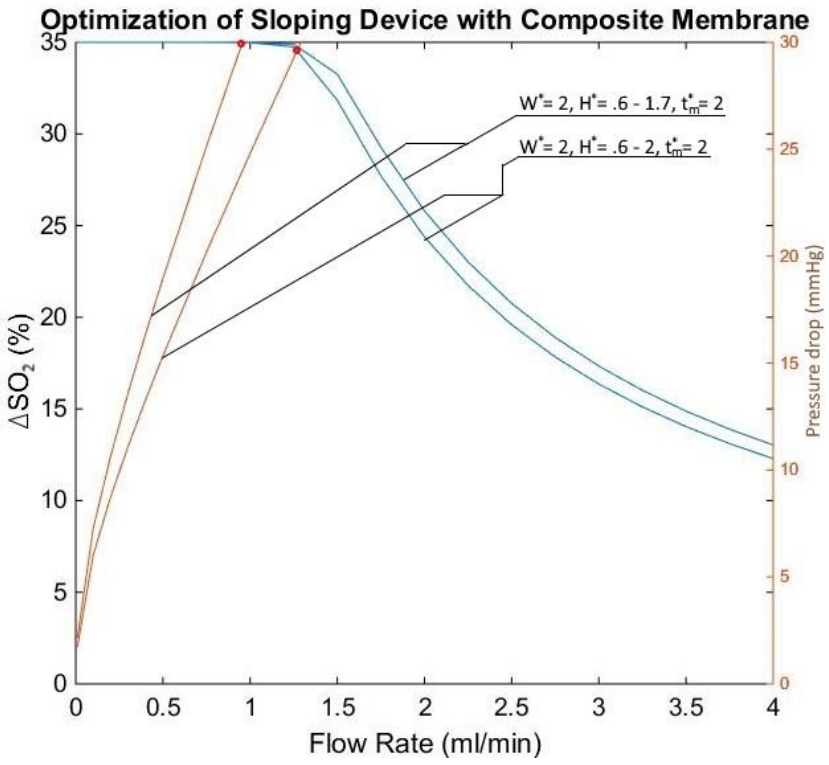

Figure 7.17 Characteristic curves for the optimized configuration of sloping device with composite membrane.

Any further changes in geometric parameters will adversely affect the performance. Increasing height will reduce the pressure drop as well as the oxygenation characteristics. As a result, the device will have a reduced oxygenation capability. Similarly, decreasing height will increase the pressure drop as well as the oxygenation characteristics. The oxygenation characteristic will remain unchanged as it is already at its maximum capacity, but the operating flow rate will reduce. Also, reducing membrane thickness cannot improve the performance either, as the membrane thickness only affects the oxygenation characteristic and the oxygen uptake is already at its maximum capacity.

So the optimized configuration for sloping device within the current manufacturing abilities has device width of 107 mm, maximum height of 200 µm, minimum height of 60 µm, and membrane thickness of 50 µm. At this configuration the device operates at 1.25

ml/min flow rate, 30 mmHg pressure drop and exhibits change in oxygen saturation of 35%.

In this chapter, parametric analysis of various designs have been done. In particular, flat profile with PDMS membrane, flat profile with composite membrane, sloping profile with PDMS membrane, and sloping profile with composite membrane have been analyzed. Each parameter is studied in isolation by varying it within a set range, while keeping the other parameters constant. Final analysis shows the width and the height of the device has significant effect on the performance with width producing the desirable effect by increasing the change in oxygen saturation and the blood flow rate at the optimal point.

Chapter 8 – Conclusion

The chapter summarizes the key contributions to the project and suggests new designs for future work that can improve the performance of an oxygenator. The fabrication process of the design is conceptualized and the performance of the designs is predicted using the model developed in chapter 5. In particular, the designs attempt to increase the gas exchange area or/and reduce the diffusion length for oxygen by various means.

8.1 Key Contributions

Key contribution of this thesis are as follows:

8.1.1 Experimental Setup Redesign to Reduce the Experimental Error

An active control mechanism was developed to maintain the oxygen saturation property of the blood in a reservoir so that its variation over 1 hour is reduced to ±3% from >+/- 9%.

As mentioned in chapter 4, average time to test one device with blood is 30-45 minutes. It is essential that the oxygen saturation of the input blood remains within ±5% of the set oxygen saturation during that time.

In the previous experimental setup, blood was deoxygenated to the desired point and stored in a reservoir. In such a case, the blood would exchange gases with the ambient air in the container and its oxygen saturation would change by at least 9% in an hour. As a result, a new experimental setup was built.

In the new experimental setup, two hollow fiber oxygenators – one oxygenates the blood while other deoxygenates the blood- were present that actively balance the oxygen taken

up from the ambient air and the oxygenator with the oxygen released by the deoxygenator. As a result, the oxygen saturation of the input blood deviated by ±3% from the set point within an hour.

8.1.2 Introduction of a Reinforced Thin Membrane to Improve Oxygenation

Previously, PDMS membrane was used, which is flexible in nature and would expand under pressure adversely affecting the performance of the device. Hence, a new composite membrane was developed that maintains the height profile of the device when it is under operation.

The membrane of the device was reinforced with steel mesh for added mechanical strength and the height profile was changed from a flat profile to a sloping profile to reduce pressure drop. Such changes improved the oxygen uptake from 18 µL/min to 26 µL/min at an operating pressure of 30 mmHg for shifting from PDMS membrane to composite membrane, and improved device throughput from 1.25 ml/min to 1.5 ml/min for shifting from flat profile to sloping profile.

It was seen the PDMS membrane expanded under operation. As a result, the channel height increased adversely affecting the oxygen uptake. A new composite membrane made out of PDMS, reinforced with steel mesh was fabricated. The presence of steel mesh maintained the channel height, which improved the oxygenation characteristic.

Later, it was realized that the area near the inlet and the outlet contributed significantly to the pressure drop, while the area near the center contributed significantly oxygen uptake. As a result, a sloping height profile was introduced to increase the height at the inlet and the outlet to reduce the pressure drop, and to decrease the height near the center to

increase the oxygen uptake. These changes lead to no changes in the oxygen uptake, but the operating flow rate increased from 1.25 ml/min to 1.5 ml/min.

8.1.3 Mathematical Model

A mathematical model was developed that could simulate oxygen uptake, membrane deflection and pressure drop in a device. The model was developed to improve the understanding of the oxygen uptake and its dependence of various geometric parameters. The sloping profile device with composite membrane was later used to optimize its performance to the operating flow rate of 1.2 ml/min, change in oxygen saturation of 34%, and the operating pressure drop of 30 mmHg. The configuration of the device is as follows: 107 mm width, 200 µm maximum channel height, 60 µm minimum channel height, and 50 µm membrane thickness.

8.2 Recommendation for Future Work: Large Sloping Device with Composite Membrane

The first improvement that could improve the performance of a device would be to reconfigure the sloping profile with composite membrane to its optimum geometry as explained in chapter 7. The performance of the device will be 34% of change in oxygen saturation of the blood and 1.2 ml/min of blood flow rate at the operating pressure of 30 mmHg. The configuration of such a device will be as follows: 107 mm width, 200 µm maximum channel height, 60 µm minimum channel height, and 50 µm membrane thickness. The mold for such a device can be fabricated using micro-milling operation. Rest of the fabrication process will be the same as explained in chapter 4.

8.3 Recommendation for Future Work: Double Sided Gas Diffusion

As it has been established in the previous few chapters, increasing gas exchange area and shortening diffusion length improve the oxygenation characteristic, but such changes increase the pressure drop at the same time. A new design has been proposed in this section that improves oxygenation capacity and does not affect the pressure drop characteristic. Such device is called double-sided diffusion.

8.3.1 Design

The double-sided diffusion device allows oxygen to diffuse in the blood from the top and the bottom of the device contrasting from the device so far studied in the thesis which only allows diffusion from the bottom. As a result, the double-sided diffusion device has twice the area for gas exchange and half the diffusion length for oxygen as compared to the devices studied so far.

The design of such a device is shown in figure 8.2. The blood enters the device through tubing as inlet, into a microvascular network that hosts an array of uniformly spaced square pillars to uniformly distribute the blood stream; the top and the bottom of the pillars hold composite membranes. The blood flowing inside the device has lower partial pressure of oxygen as compared to the partial pressure. As a result, a gradient of partial pressure is developed that allows the oxygen in the atmosphere to diffuse through from the top and the bottom of the device.

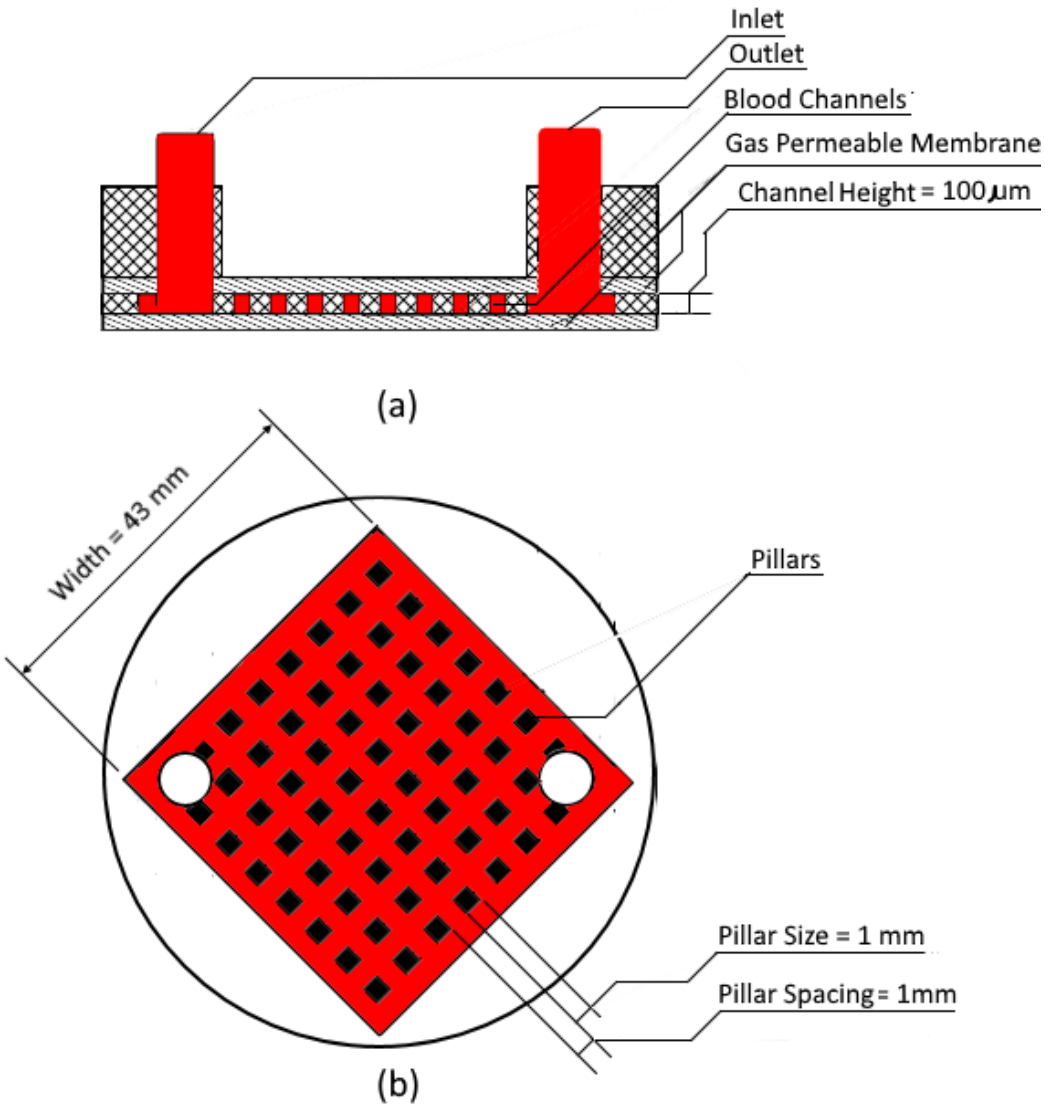

Figure 8.1 Illustration of a device with double sided diffusion.

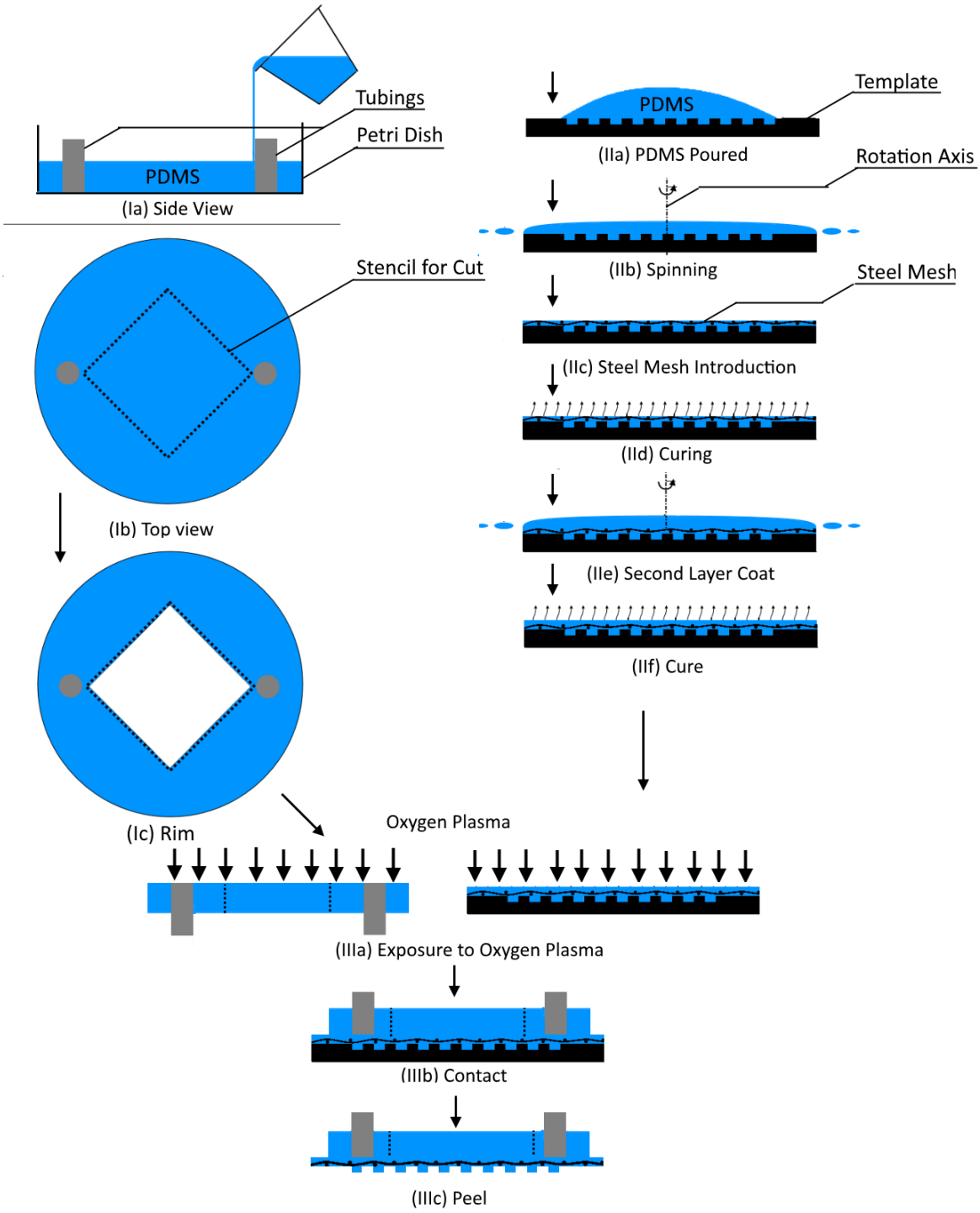

Figure 8.2 Process of preparing the vascular network and the rim and bonding them together using oxygen plasma.

8.3.2 Fabrication Process

The device with double-sided diffusion consists of three parts: composite membrane, vascular network, and a rim to hold the vascular network. The composite membrane is fabricated by the same process laid out in section 4.3 of chapter 4. But for a device with double-sided diffusion, the process of fabricating the vascular network is done by spinning PDMS on a substrate. And the rim is fabricated by casting PDMS in a petri dish. The process is laid out in figure 8.2.

Rim is fabricated by placing tubing with 3 mm inner diameter and 4 mm length in a petri dish and 10 ml of PDMS is measured and poured into the petri dish (fig 8.2 Ia) and is cured in an oven at 60^{o} C for 5 hours. Then, a large square hole is made by using a stencil placed on top of the resulting product (fig 8.2 Ib and Ic).

The vascular network is prepared by spin coating a thin layer of PDMS over the mold at 2000 RPM for 30 seconds (fig 8.2 IIa and IIb). A piece of 39 ± 2 μm thick steel mesh cut into 50 cm X 50 cm dimension is gently laid on the uncured PDMS layer(fig 8.2 IIc) and the product is cured in an oven at 60^{o} C for 5 hours(fig 8.2 IId). Later another layer of PDMS is spun on top of the product at 4000 RPM for 30 seconds (fig 8.2 IIe) and the resulting product is cured in an oven at 60^{o} C for 5 hours (fig 8.2 IIf).

Finally, the rim is bonded to the vascular network by exposing their surfaces to oxygen plasma and bringing them in contact to form a bond.

The rest of the process including membrane fabrication and its bonding to the vascular network is done by spin coating and oxygen plasma respectively; the process is laid out in section 4.3 of chapter 4.

8.3.3 Expected Performance

The expected performance was calculated using the model explained in chapter 5 to check if the proposed design could improve the performance. The analysis was done by assuming that the blood was at standard physiological conditions: pH = 7.4, pCO_2 = 27 mmHg, T = 37 degree Celsius. The oxygen saturation of the input blood was taken as 65%. The geometric parameters of the device were 43 mm device width, 50 µm membrane thickness (of both membranes) and 100 µm channel height. Also, the performance of the device with double-sided diffusion was compared with the performance of a device with one-sided diffusion with same dimensions.

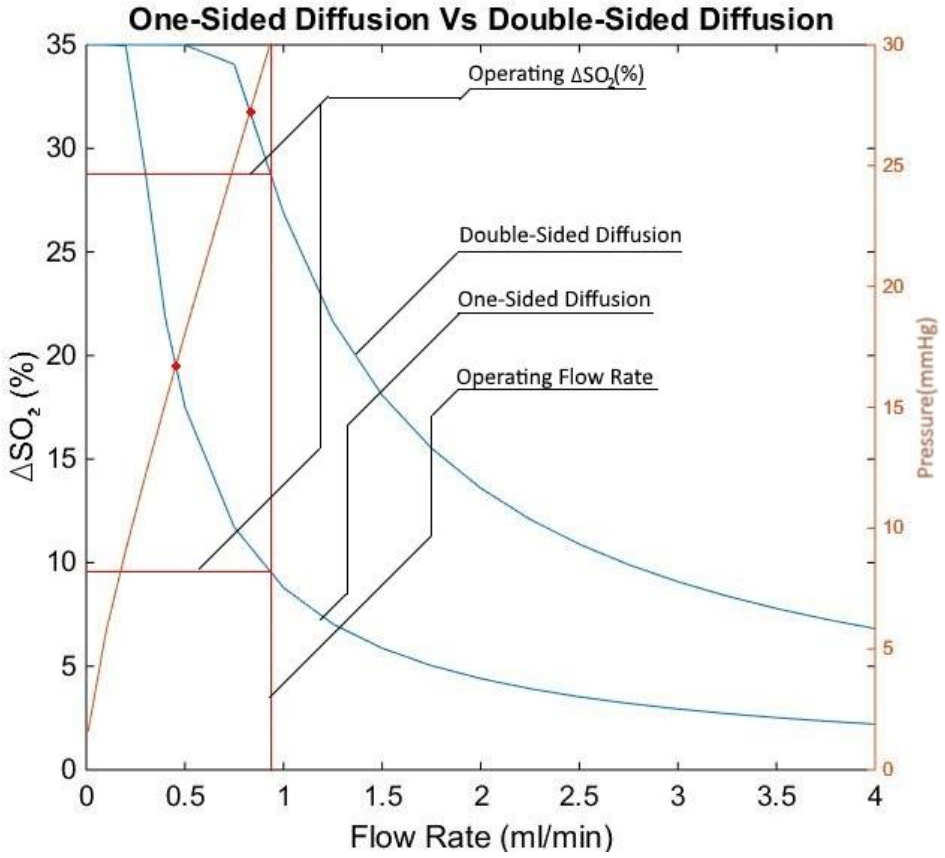

Figure 8.3 Expected performance of the double-sided diffusion device compared with the performance of a device with one-sided diffusion with same configuration.

Figure 8.3 shows the comparison of the performance of a device with double-sided diffusion and with one-sided diffusion. Pressure drop and the change in the oxygen saturation of the device is plotted on the same graph. The devices exhibit similar pressure drop characteristic, but the device with double sided diffusion exhibits significantly better oxygenating characteristics. At the operating pressure of 30 mmHg, the devices exhibit a flow rate of 0.9 ml/min, but the one sided diffusion device exhibits 9% change in oxygen saturation and the device with double sided diffusion exhibits 28% change in oxygen saturation.

This improvement in oxygenation characteristics is a result of increased gas exchange area and shortened diffusion length for oxygen. Since, the oxygen diffuses from the top as well as the bottom of the channels, the gas exchange area becomes twice its original size and the diffusion length becomes half its original value.

8.4 Recommendation for Future Work: All Sided Gas Diffusion

Similar to the device with double-sided diffusion, another design is conceived that further increases oxygenation capacity and does not affect the pressure drop characteristic. Such a device is called all-sided diffusion.

8.4.1 Design

The all-sided gas diffusion device allows oxygen transfer from all the walls that blood gets in contact with in the device, contrasting from the device studied so far which only allows diffusion bottom or/and top of the device. As a result, all-sided gas diffusion device will have a higher gas exchange area and shorter oxygen diffusion length than the devices discussed so far.

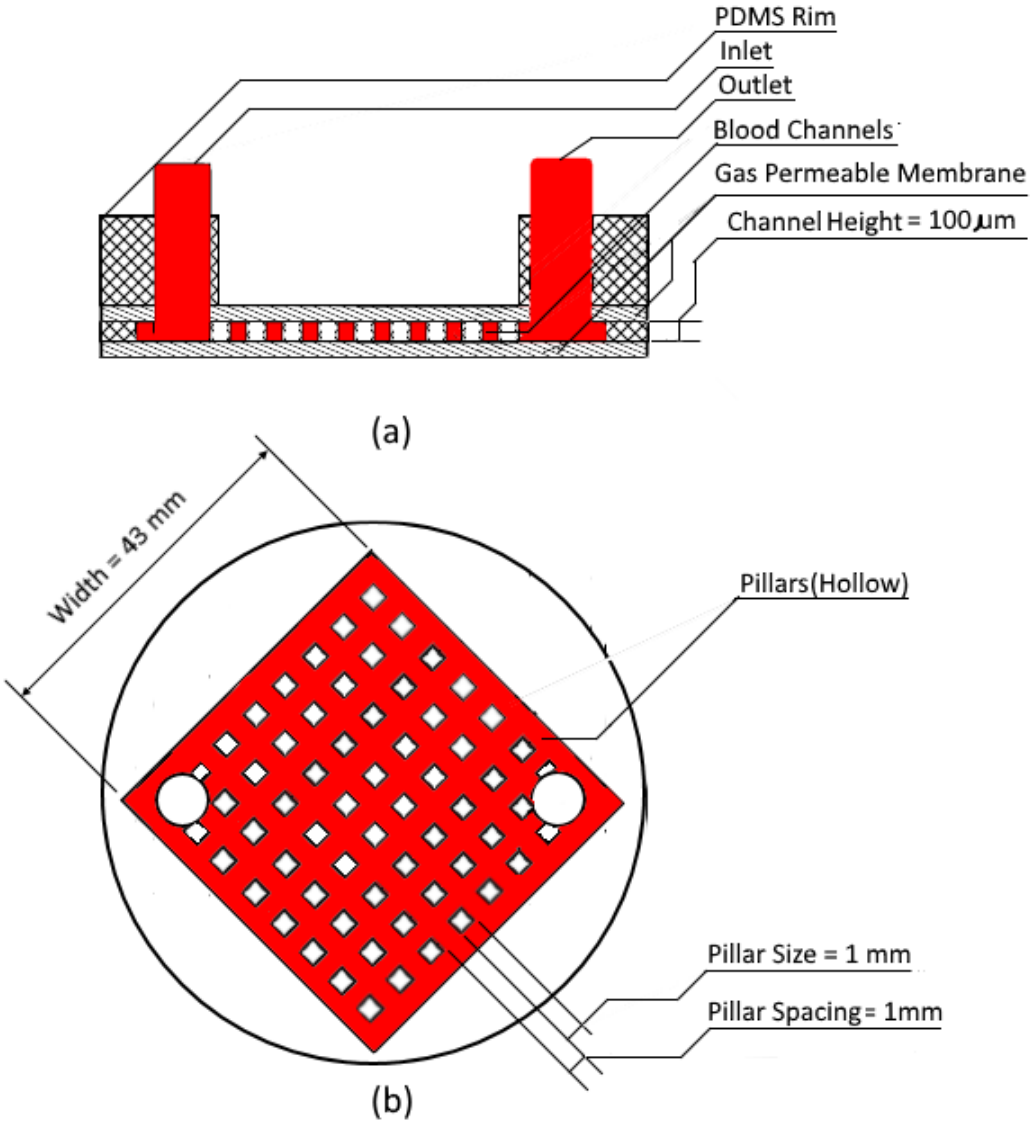

Figure 8.4 Illustration of a device with all-sided diffusion.

Such a device is shown in figure 8.4. The basic anatomy of the device is similar to a double-sided diffusion device except, the square pillars are hollow. The air present in the hollow volume of the square pillars and outside of the device has higher partial pressure of oxygen as compare to the blood flowing the device. As a result, a gradient of partial pressure is developed that allows the oxygen in the atmosphere to diffuse through from the top and the bottom of the device, and the sides of the pillars.

8.4.2 Fabrication Process

The fabrication process of a device with all-sided diffusion is the same as the process for the device with double-sided diffusion, except for the device with all-sided diffusion the template is such that it produces hollow pillars. The process follows fabricating vascular network by the process of spin-coating and bonding it to a PDMS rim by oxygen plasma. The PDMS rim is made by casting PDMS in a petri-dish and cutting a hole in it. Once the vascular network is prepared, it is bonded to a composite membrane by means of oxygen plasma.

8.4.3 Expected Performance

The expected performance was calculated using the model explained in chapter 5 to check if the proposed design could improve the performance. The analysis was done by assuming that the blood was at standard physiological conditions: pH = 7.4, pCO_2 = 27 mmHg, T = 37 degree Celsius. The oxygen saturation of the input blood was taken as 65%. The geometric parameters of the device were 43 mm device width, 50 µm membrane thickness (of both membranes) and 100 µm channel height. The thickness of the wall of the hollow pillars was taken as 50 µm. Also, the performance of the device with all-sided diffusion was compared with the performance of a devices with double-sided diffusion and one-sided diffusion with same dimensions.

Figure 8.5 shows the comparison of the performance of a device with all-sided diffusion with the performance of devices with double-sided and one-sided diffusion. All devices exhibit similar pressure drop characteristic, but different oxygenation characteristic. Device with all-sided diffusion exhibit highest oxygenation as compared to double-sided

and one-sided. At an operating pressure of 30 mmHg, all-sided diffusion exhibit change in oxygenation of 30%, double-sided 28%, and one-sided 9%.

The improvement in oxygenation characteristic can be attributed to increase in gas exchange area and shorter diffusion length for oxygen. But since the increase in gas exchange area from double-sided diffusion is not as significant, a smaller improvement in performance is seen.

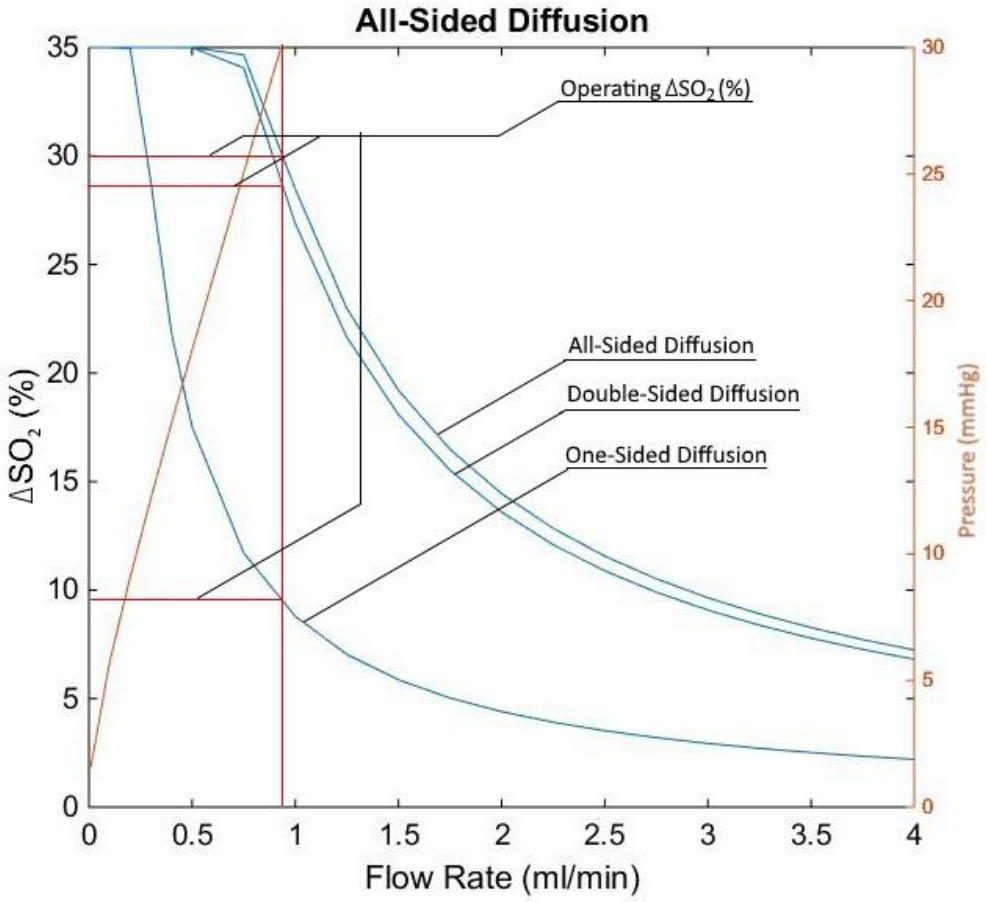

Figure 8.5 Performance comparison of a device with all-sided diffusion with the performance of devices with one-sided and two-sided diffusion.

The increased gas exchange area in case of all-sided diffusion depends on the size and the number of the pillars. In the current case, the added gas exchange area is 1.76 cm^2 for 1

mm pillar size and 441 number of pillars. But if the pillar size is reduced to 100 µm and the number of pillars increased to 44100, the added gas exchange area will be 17.6 cm^2, which will lead to dramatic increase in performance. However, such a device might be too fragile and may fail under operation.

In summary, the chapter presents the key contribution made to the project. In particular the contributions are redesigning of the experimental setup to measure the performance, redesigning of the oxygenator device, and development of a mathematical model. Later, a number of designs were proposed for future work to further improve the performance of the device. In particular, such designs are large sloping profile with composite membrane, device with double-sided diffusion, and device with all-sided diffusion. The process to fabricate such devices and their expected performance were also briefly discussed.

References

[1] J. Lee, M. Kung, H. Kung and L. Mockros, "Microchannel Technologies for Artificial Lungs: (3) Open Rectangular Channels," *American Society for Artificial Internal Organs,* vol. 54, no. 4, pp. 390-595, 2008.

[2] K. Lee, B. Khoshnood, S. N. Wall, Y. Chang, H. L. Hsieh and J. K. Singh, "Trend in mortality from respiratory distress syndrome in the United States," *Journal of Pediatrics,* vol. 134, no. 4, pp. 434-440, 1999.

[3] A. Kumar and B. V. Bhat, "Epidemiology of respiratory distress of newborns," *Indian Journal of Pediatrics,* vol. 63, no. 1, pp. 93-98, 1996.

[4] A. K. Malhotra, R. Nagpal, R. K. Gupta, D. S. Chhajta and R. K. Arora, "Respiratory distress in newborn: treated with ventilation in a level II nursery," *Indian Journal of Pediatrics,* vol. 32, no. 2, pp. 207-211, 1995.

[5] B. D. Kamath, E. R. MacGuire, E. M. McClure, R. L. Goldenberg and A. H. Jobe, "Neonatal Mortality From Respiratory Distress: Lessons from Low-Resource Countries," *Pediatrics,* vol. 127, no. 6, pp. 1139-1146, 2011.

[6] T. Fujiwara, S. Chida, Y. Watabe, H. Maeta, T. Morita and T. Abe, "Artificial Surfactant Therapy in Hyaline Membrane Disease," *The Lancet,* vol. 315, no. 8159, pp. 55-59, 1980.

[7] R. J. Rodriguez, "Management of Respiratory Distress Syndrome: An Update," *Respiratory Care,* vol. 48, no. 3, pp. 279-287, 2003.

[8] M. Mugford, D. Elbourne and D. Field, "Extracorporeal membrane oxygenation for severe respiratory failure in newborn infants(review)," *Evidence-Based Child Health: A Cochrane Review Journal,* vol. 5, pp. 241-298, 2010.

[9] A. Polito, C. S. Barrett, D. Wypij, P. T. Rycus, R. Netto, P. E. Cogo and R. R. Thiagarjan, "Neurologic complications in neonates supported with extracorporeal membraen oxygenation. An analysis of ELSO registry data," *Intensive Care Medicine,* vol. 39, pp. 1594-1601, 2013.

[10] W. Zapol, T. Kolobow, J. Pierce, G. Vurek and R. Bowman, "Artificial placenta: two days of total extrauterine support of the isolated premature lamb fetus," *Science,* vol. 166, no. 3905, pp. 617-618, 1969.

[11] A. S. Manan, "Characterizing Gas Exchange and Assessing Feasibility of a New Lung Assist Device," Department of Biomedical Engineering, McMaster University, Hamilton, 2013.

[12] V. K. Bhutani, "Development of the Respiratory System," in *Manual of Neonatal Respiratory Care*, Springer Science, 2012, pp. 3-4.

[13] M. E. Avery and J. Mead, "Surface Properties in Relation to Atelectasis and Hyaline Membrane Disease," *AMA Journal of Diseases of Children,* vol. 97, pp. 517-523, 1959.

[14] J. U. Raj and J. R. Wright, "Respiratory Distress Syndrome," in *Breathing in America: Diseases, Progress, and Hope*, American Thoracic Society, 2010, pp. 197-206.

[15] J. P. Goldsmith and E. H. Karotkin, "Introduction to Assisted Ventilation," in *Assisted Ventilation of the Neonates*, Saunders, 2011, pp. 1-18.

[16] S. M. Donn and S. K. Sinha, "Newer techniques of mechanical ventilation: an overview," *Seminars in Neonatalogy*, vol. 7, pp. 401-407, 2002.

[17] T. E. Wiswell and S. E. Courtney, "Noninvasive Respiratory Support," in *Assisted Ventilation for the Neonates*, Saunders, 2011, pp. 140-162.

[18] R. Ramanathan, K. C. Sekar, M. Rasmussen, B. J and R. F. Soll, "Nasal intermittent positive pressure ventilation after surfactant treatment for respiratory distress syndrome in preterm infants <30 weeks' gestation: a randomized, controlled trial," *Journal of Perinatology*, vol. 32, pp. 336-343, 2012.

[19] R. M. Arensman and B. L. Short, "Extracorporeal Membrane Oxygenation," in *Assisted Ventilation of the Neonates*, Saunders, 2011, pp. 277-291.

[20] P. K. Riyas, K. M. Vijayakumar and M. L. Kulkarni, "Neonatal Mechanical Ventilation," *Indian Journal of Pediatrics*, vol. 70, pp. 537-540, 2003.

[21] S. K. Gautham and R. F. Soll, "Overview of Surfactant Replacement Trials," *Journal of Perinatology*, pp. S40-S44, 2005.

[22] R. Soll, "Synthetic surfactant for respiratory distress syndrome in preterm infants," *The Cochrane Collaboration,* no. 3, 1998.

[23] A. G. S. Philip, "Neonatal Mortality rate: Is further improvement possible," *The Journal of Pediatrics,* vol. 126, no. 3, pp. 427-433, 1995.

[24] R. H. Barlett, A. B. Gazzaniga, M. R. Jefferies, R. F. Huxtable, N. J. Haiduc and S. W. Fong, "Extracorporeal membrane oxygenation cardiopulmonary support in infancy," *Transactions - American Society of Artificial Internal Organs,* vol. XXII, pp. 80-92, 1976.

[25] P. P. O'Rourke, R. K. Crone, J. P. Vacanti, J. H. Ware, C. W. Lillehei, R. B. Parad and M. F. Epstein, "Extracorporeal membraen oxygenation oand conventional medical therapy in neonates with persistent pulmonary hypertension of the newborn: a prospective randomized study," *The Journal of Pediatrics,* vol. 84, no. 6, pp. 957-963, 1989.

[26] W. P. Kanto, "A decade of experience with neonatal extracorporeal membrane oxygenation," *The Journal of Pediatrics,* vol. 124, no. 3, pp. 335-347, 1994.

[27] C. D. Downard, P. Betit, R. W. Chang, J. J. Garza, J. H. Arnold and J. M. Wilson, "Impact of AMICAR on hemorrhagic complication of ECMO: A Ten-Year Review".

[28] J. Awad, R. Cloutier, L. Fournier, D. Major, L. Martin, M. Masson and R. Guidoin, "Pumpless respiratory assistance using a membrane oxygenator as an artificial

placenta: a preliminary study in newborn and preterm lambs," *Investigative Surgery,* vol. 8, no. 1, pp. 21-30, 1995.

[29] J. Reoma, A. Rojas, A. Kim, J. Khouri, E. Boothman, K. Brown, J. Grotberg, K. Cook, R. Bartlett, R. Hirschl and G. Mychaliska, "Development of an artificial placenta I: pumpless arterio-venous extracorporeal life support in a neonatal sheep model," *Journal of Pediatric Surgery,* vol. 44, no. 1, pp. 53-59, 2009.

[30] B. Gray, A. El-Sabagh, A. Rojas-Pena, A. Kim, S. Gadepali, K. Koch, T. Capizzani, R. Bartlet and G. Mychaliska, "Development of an artificial placenta IV: 24-hour venovenous extracorporeal life support in premature lambs," *ASAIO Journal,* vol. 58, no. 2, pp. 148-154, 2012.

[31] Y. Miura, T. Matsuda, A. Funakubo, S. Watanabe, R. Kitanishi, M. Saito and T. Hanita, "Novel modification of an artificial placenta: pumpless arteriovenous extracorporeal life support in a premature lamb model," *Pediatric RESEARCH,* vol. 72, no. 5, pp. 490 - 494, 2012.

[32] B. Bryner, B. Gray, E. Perkins, R. Davis, H. Hoffman, J. Barks, G. Owens, M. Bocks, A. Rojas-Pena, R. Hirschl, R. Barlett and G. Mychalisk, "An extracorporeal artificial placenta supports extremely premature lambs for one week," *Journal of Pediatric Surgery,* vol. 1, no. 50, pp. 44-49, 2015.

[33] M. Schroberer, J. Arens, A. Erben, D. Ophelders, R. K. Jellema, B. W. Kramer, J. L. Bruse, P. d. Brouwer, T. Schmitz-Rode, U. Steinseifer and T. Orlikowsky,

"Miniaturization: The Clue to Clinical Application of the Artificial Placenta," *Journal of Artificial Organs,* vol. 38, no. 3, pp. 208-214, 2013.

[34] R. A. DeWall, H. E. Warden, R. C. Read, V. L. Gott, N. R. Ziegler, R. L. Varco and C. W. Lillehei, "A simple, expendable, artificial oxygenator for open heart surgery," *The Surgical Clinics of North America,* pp. 1025-1034, 1956.

[35] J. A. Wegner, "Oxygenator Anatomy and Function," *Journal of Cardiothoracic and Vascular Anesthesia,* vol. 11, no. 3, pp. 275-281, 1997.

[36] H. Iwahashi, K. Yuri and Y. Nose, "Development of the oxygenator: past, present, and future," *Journal of Artificial Organs,* vol. 7, no. 3, pp. 111-120, 2004.

[37] T. Kolobow and R. L. Bowman, "Construction and evaluation of an alveolar membrane artificial heart-lung," *ASAIO,* vol. IX, pp. 238-243, 1963.

[38] R. H. Barlett, A. F. Andrews, J. M. Toomasian, N. J. Haiduc and A. B. Gazzaniga, "Extracorporeal membrane oxygenation for newborn respiratory failure: forty-five cases," *Surgery,* vol. 92, no. 2, pp. 425-433, 1982.

[39] N. C. Saxena, P. Hillyer and L. H. Edmunds Jr., "Use of the spiral coil membrane oxygenator during open heart surgery in infants and children.," *The Journal of cardiovascular surgery,* vol. 18, no. 1, pp. 1-7, 1976.

[40] J. D. S. Gaylor, "Membrane oxygenators: current developments in design and application.," *Journal of biomedical engineering,* vol. 10, no. 6, pp. 541-547, 1988.

[41] J. D. S. Gaylor, S. Hickey, G. Bell and J. M. Pei, "Membrane oxygenators: influence of design on perfromance," *Perfusion,* vol. 9, pp. 173-180, 1994.

[42] M. E. Voorhees and B. F. Brian III, "Blood-gas Exchange Devices," *International anesthesiology clinics,* vol. 34, no. 2, pp. 29-46, 1996.

[43] L. Lequier, "Extracorporeal life support in pediatric and neonatal critical care: a review.," *Journal of Intensive Care Medicine,* vol. 19, no. 5, pp. 243-258, 2004.

[44] H. A. Stone and S. Kim, "Microfluidics: basic issues, applications, and challenges.," *AIChE Journal,* vol. 47, no. 6, pp. 1250-1254, 2001.

[45] R. H. Lam, M.-C. Kim and T. Thorsen, "Culturing aerobic and anaerobic bacteria and mammalian cells with a microfluidic differential oxygenator," *Analytical Chemistry,* vol. 81, no. 14, pp. 5918-5924, 2009.

[46] J. K. Lee, H. H. Kung and L. F. Mockros, "Microchannel technologies for artificial lungs:(1) theory.," *ASAIO Journal,* vol. 54, no. 4, pp. 372-382, 2008.

[47] M. C. Kung, J. K. Lee, H. H. Kung and L. F. Mockros, "Microchannel Technologies for Artificial Lungs: (2) Screen-filled Wide Rectangular Channels," *ASAIO,* vol. 54, no. 4, pp. 383-389, 2008.

[48] J. K. Lee, M. C. Kung, H. H. Kung and L. F. Mockros, "Microchannel Technologies for Artificial Lungs: (3) Open Rectangular Channels," *ASAIO,* vol. 54, no. 4, pp. 390-395, 2008.

[49] J. A. Potkay, "A high efficiency micromachined artificial lung.," *Solid-State Sensors, Actuators and Microsystems Conference, Transducers, IEEE,* pp. 2234-2237, 2009.

[50] D. M. Hoganson, H. I. Pryor II, E. K. Bassett, I. D. Spool and J. P. Vacanti, "Lung assist device technology with physiologic blood flow developed on a tissue engineered scaffold platform.," *Lab on a Chip,* vol. 11, no. 4, pp. 700-707, 2011.

[51] T. Kniazeva, J. C. Hsiao, J. L. Charest and J. T. Borenstein, "A microfluidic respiratory assist device with high gas permeance for artificial lung application," *Journal of Biomedical Microdevices,* vol. 13, pp. 315-323, 2011.

[52] J. A. Potkay, M. Magnetta, A. Vinson and B. Cmolik, "Bio-inspired, efficient, artificial lung employing air as the ventilating gas.," *Lab on a Chip,* vol. 11, no. 17, pp. 2901-2909, 2011.

[53] W.-I. Wu, N. Rochow, E. Chan, G. Fusch, A. Manan, D. Nagpal, P. R. Selvaganapathy and C. Fusch, "Lung assist device: development of microfluidic oxygenators for preterm infants with respiratory failure," *Lab on a chip,* vol. 13, pp. 2641-2650, 2013.

[54] K. M. Kovach, M. A. LaBarbera, M. C. Moyer, B. M. Cmolik, E. Van Lunteren, A. Sen Gupta, J. R. Capadona and J. A. Potkay, "In vitro evaluation and in vivo demonstration of a biomimetic, hemocompatible, microfluidic artificial lung," *Lab on a Chip,* vol. 15, pp. 1366-1375, 2015.

[55] M. H. Weissman and L. F. Mockros, "Oxygen and carbon dioxide transfer in membrane oxygenators," *Medical & Biological Engineering*, vol. 7, pp. 169-184, 1969.

[56] M. H. Weissman and T. K. Hung, "Numerical simulation of convective diffusion in blood flowing in a channel with a steady, three-dimensional velocity field," *AIChE*, vol. 17, no. 1, pp. 25-30, 1971.

[57] T.-K. Hung, "Transport and flow phenomena in a microchannel membrane oxygenator," *Annals of Biomedical Engineering*, vol. 5, pp. 343-371, 1977.

[58] T. J. Hewitt, B. G. Hattler and W. J. Federspiel, "A mathematical model of gas exchange in an intravenous membrane oxygenator".

[59] J. A. Potkay, "A simple, closed-form, mathematical model for gas exchange in microchannel artificial lungs," *Biomedical Microdevices*, vol. 15, no. 3, pp. 397-406, 2013.

[60] G. S. Matte and J. A. DiNardo, "Pediatric Cardiopulmonary Bypass," in *Cardiopulmonary Bypass and Mechanical Support: Principles & Practice*, Wolters Kluwer, 2015.

[61] T. Kiserud, C. Ebbing, J. Kessler and S. Rasmussen, "Fetal cardiac output, distribution to the placenta and impact of placental compromise," *Ultrasound in Obstetrics & Gynecology*, vol. 28, pp. 126-136, 2006.

[62] N. Rochow, A. Manan, W.-I. Wu, G. Fusch, S. Monkman, J. Leung, E. Chan, D. Nagpal, D. Predescu, J. Brash, P. R. Selvaganapathy and C. Fusch, "An integrated array of microfluidic oxygenators as a neonatal lung assist device: in vitro characterization and in vivo demonstration," *Journal of Artificial Organs,* vol. 38, no. 10, pp. 856-866, 2014.

[63] F. a. D. Administration, "Guidance for Cardiopulmonary Bypass Oxygenator 510(k) Submissions," Center for Devices and Radiological Health, 2000.

[64] C. O. F. Kamlin, C. P. F. O'Donnell, P. G. Davis and C. J. Morley, "Oxygen saturation in health infants immediately after birth," *The Journal of Pediatrics,* vol. 148, no. 5, pp. 585 - 589, 2006 .

[65] S. J. Clarson and J. F. Rabolt, "A study of the phase transitions in cyclic poly(dimethylsiloxane) by Raman spectroscopy and thermal analysis," *Macromolecules,* vol. 26, no. 10, pp. 2621-2623, 1993.

[66] H. D. Baehr and K. Stephan, "Fick's Law," in *Heat and Mass Transfer,* New York, Springer, 2011, p. 71.

[67] A. V. Hill, "The possible effects of the aggregation of the molecules of haemoglobin on its dissociation curve," *Journal of Physiology,* vol. 40, pp. 4-7, 1910.

[68] H. D. Baehr and K. Stephan, "Overall Mass Transfer," in *Heat and Mass Transfer,* New York, Springer, 2011, pp. 92-93.

[69] S. Kawahito, T. Maeda, T. Motomura, T. Takano, K. Nonaka, J. Linneweber, M. Mikami, S. Ichikawa, M. Kawamure, J. Glueck, K. Sato and Y. Nose, "Development of a new hollow fiber silicone membrane oxygenator: in vitro study," *Artificial Organs*, vol. 25, no. 6, pp. 494-498, 2001.

[70] K. W. Oh, K. Lee, B. Ahn and E. P. Furlani, "Design of pressure-driven microfluidic networks using electric circuit analogy," *Lab on a Chip*, vol. 12, no. 3, pp. 515-545, 2012.

[71] Y.-H. Hsu, M. L. Moya, P. Abiri, C. C. W. Hughes, S. C. George and A. Lee, "Full range physiological mass transport control in 3D tissue cultures(Supplementary Information)," *Lab on a Chip*, vol. 13, pp. 81-89, 2013.

[72] Y. I. Cho and K. R. Kensey, "Effects of the non-Newtonian viscosity of blood on flows in a diseased arterial vessl. Part 1: steady flows," *Biorheology*, vol. 28, pp. 241-262, 1991.

[73] W. K. Schomburg, "Membranes," in *Introduction to Microsystem Design*, Springer-Verlag Berlin Heidelberg, 2011, pp. 29-52.

[74] J. A. Potkay, "A simple, closed-form, mathematical model for gas exchange in microchannel artificial lungs," *Biomed Microdevices*, vol. 15, pp. 397-406, 2013.

[75] S. N. Vaslef, L. F. Mockros, R. W. Anderson and R. J. Leonard, "Use of Mathematical Model to Predict Oxygen Transfer Rates in Hollow Fiber Membrane Oxygenator," *American Society of Artificial Internal Organs*, pp. 990-996, 1994.

[76] T. J. Hewitt, B. G. Hattler and W. J. Federspiel, "A Mathematical Model of Gas Exchange in an Intravnous Membrane Oxygenator," *Annals of Biomedical Engineering,* vol. 26, pp. 166-178, 1998.

[77] R. K. Dash and J. B. Bassingthwaighte, "Erratum to: Blood HbO2 and HbCO2 Dissociation Curves at Varied O2, CO2, pH, 2,3-DPG and Temperature Levels," *Annals of Biomedical Engineering,* vol. 38, no. 4, pp. 1683-1701, 2010.

[78] J. A. Potkay, M. Magnetta, A. Vinson and B. Cmolik, "Bio-inspired, efficient, artificial lung employing air as the ventilating gas," *Lab on a Chip,* pp. 2901-2909, 2011.

[79] K. Khanafer, A. Duprey, M. Schlicht and R. Bergeur, "Effects of strain rate, mixing ratio, and stress-strain definition on the mechanical behavior of the polydimethylsiloxane (PDMS) material as related to its biological applications," *Biomedical Microdevices,* vol. 11, pp. 503-508, 2009.

[80] Z. Peng and S. Chen, "Effect of bending stiffness on the peeling behavior of an elastic thin film on a rigid substance," *Physical Review E,* vol. 91, no. 4, 2015.

[81] N. Pracha, W. Yang and H. S. Bada-Ellzey, "Blood pressure measurements in the newborn," *Clinics in perinatology,* vol. 4, pp. 981-96, 1999.

[82] J. West, "Shunt Equation," in *Respiratory Physiology: The Essentials*, 2005, p. 169.

[83] F. B. Plotz, R. A. van Lingen and A. P. Bos, "Venous oxygen measurements in the inferior vena cava in neonates with respiratoy failure," *Criticial Care,* vol. 2, no. 2, pp. 57-60, 1998.

[84] T. A. O'Connor and R. T. Hall, "Mixed venous oxygenation in crticially ill neonates," *Critical Care Medicine,* vol. 22, no. 2, pp. 343-346, 1994.

Appendices

Appendix A: Micro-Vascular Network Fabrication

1. The mold for the micro-vascular network was prepared using soft-lithography for flat profile device or micro-milling operation for sloping-profile design.
2. Preheat the oven to 60^{o} C
3. Mix PDMS base and curing agent in a 10:1 w/w ratio.
4. Stir mixture well with a stirrer.
5. Place the mixture under vacuum for 10 minutes.
6. Place the mold on a levelled surface.
7. Cut two 5 mm long silicone tubing with 3 mm ID
8. Place the tubings at the inlet and the outlet of the SOU.
9. Pour 12 ml of PDMS mixture on the mold.
10. Place the mold in the oven at 60^{o} C for 2 hours.
11. Remove the mold from the oven and cut the PDMS around the network.
12. Remove residual PDMS from the inlet and the outlet tubings.
13. Place the network in a clean petri dish.

Appendix B: PDMS Membrane Fabrication

1. Prepare the substrate by placing Teflon sheet on top of a silicon wafer.
2. Prepare PDMS base and curing agent mixture in 10:1 w/w ratio as described in appendix A.
3. Center the substrate onto spinner.
4. Set the spin rate at 500 RPM for 10 s and increase to 4000 RPM for 30 s.
5. Pour 1 ml of PDMS mixture on the substrate.
6. Run the spinner.
7. Place the resulting product in the oven at 60^{o}C for 5 hours.

Appendix C: Composite Membrane Fabrication

1. Prepare the substrate by placing Teflon sheet on top of a silicon wafer.
2. Prepare PDMS base and curing agent mixture in 10:1 w/w ratio as described in appendix A.
3. Center the substrate onto spinner.
4. Set the spin rate at 500 RPM for 10 s and increase to 4000 RPM for 30 s.
5. Pour 1 ml of PDMS mixture on the substrate.
6. Run the spinner.
7. Place a 50 cm X 50 cm cut piece of a steel-mesh on the thin layer of PDMS.
8. Place the resulting product in the oven at 60^{o}C for 5 hours.
9. Cut the steel mesh around the edge of the substrate
10. Place the product onto spinner.
11. Repeat steps 4 to 6 and 8 from appendix C.

Appendix D: Bonding Vascular Network with the Membrane

1. Place the membrane and the vascular network in the plasma chamber.
2. Tightly close the chamber.
3. Turn on the pump.
4. Wait till the pressure inside the chamber reaches between 200-250 mTorr, turn on the oxygen flow.
5. Wait till the pressure inside the chamber reaches between 500-550 mTorr, turn the plasma on and turn power knob to ‘High’.
6. Now the surfaces of the network and the membrane are being exposed to plasma. Wait for 2.5 minutes.
7. Turn the power knob to ‘Off’. Turn off the plasma. Turn off the pump in order.
8. Slowly vent the chamber.
9. Put vascular network in contact with the membrane.
10. Place the device in an oven at 60^{o} C for 4 – 6 hours.
11. Gently peel the device off the substrate.
12. For the device with composite membrane, the device is ready. For the device with PDMS membrane, repeat steps from 1 to 11 of appendix D with the resulting product and another membrane.